

修士論文

MEMS マイクロミラーの強度解析と信頼性評価に関する研究

PAGE 1 ~ PAGE 184

平成 16 年 2 月 13 日 提出

指導教官 酒井信介教授

26199 チャン ウェー ピン

1	Research background	5
1.1	Social aspect	5
1.2	Academic aspect	7
2	Aims of research	10
3	Theory	11
3.1	Weibull theory	11
3.1.1	Introduction	11
3.1.2	Problems of using the Weibull theory	12
3.1.3	Significance of the Weibull modulus m	13
3.1.4	Estimating the Weibull parameters using the Maximum Likelihood Estimator (MLE)	13
3.2	Load factor analysis	15
3.2.1	Definition	15
3.2.2	Interpretation	15
3.2.3	Load factor PDF (probability density function)	16
3.2.4	Load factor CDF (cumulative distribution function)	17
3.2.5	Other essential points	18
3.3	FEM analysis	20
3.3.1	Necessity of FEM analysis and accurate experimental displacement	20
3.3.2	Submodeling	20
3.3.3	Construction of a good initial FEM model based on pure bending experimental results	22
3.3.4	Problems of the different types of FEM elements	23
3.3.5	Relationship between the site of crack initiation and the maximum principal stress	29
3.3.6	Degree of fineness of mesh	30
3.3.7	Anisotropic material constant for silicon	31
3.3.8	Limitations of FEM analysis	35
3.4	Bayesian reliability analysis	36
3.4.1	Introduction	36
3.4.2	Non-informative prior	37
3.4.3	Effectiveness of the Bayesian method with respect to the MLM (maximum likelihood method)	39
3.5	St. Venant torsion theory	40
3.6	Saint-Venant's principle	41

3.7	Safety design in the context of reliability engineering	42
3.7.1	Introduction to Crystal Ball	42
3.7.2	Monte Carlo simulation and importance sampling simulations	43
3.7.3	Proof test of brittle material	44
3.7.4	Dynamic simulation	44
3.7.5	Probabilistic design	45
3.7.6	Traditional (deterministic) vs. probabilistic design analysis methods	46
3.7.7	Surface response method	47
4	Design of test specimen	50
4.1	Overview	50
4.2	Experimental considerations	50
4.3	Mechanical considerations	50
4.4	Stress ratio	51
4.5	Maximum shear stress calculation	52
4.6	Maximum normal tensile stress calculation	53
4.7	Torque calculation	54
4.8	Points to be noted in the design process	54
4.9	Excel sheet calculation	55
4.10	Final dimensions of beams	57
5	Experimental apparatus and procedures	58
5.1	Experiment setup	58
5.1.1	Introduction	58
5.1.2	Wafers containing the test samples	59
5.1.3	Silicon etching process	59
5.1.4	Apparatus	61
5.1.5	Alignment of the laser spot	62
5.1.6	Estimating the thickness of the wafer	63
5.1.7	Precautions in performing the test	64
5.2	Experimental procedures	65
5.2.1	Pure bending test	65
5.2.2	Combined bending test	65

6	Experimental test results and discussion	66
6.1	FEM model overview	66
6.2	Pure bending experimental and FEM results (batch 1; batch 2)	69
6.2.1	FEM fractured stresses	69
6.2.2	Experimental and FEM displacements	70
6.3	Combined loading experimental and FEM results (batch 1; batch 2)	71
6.3.1	FEM fractured stresses	71
6.3.2	Experimental and FEM displacements	74
6.4	Various types of fractured stress plots	78
6.4.1	Weibull plot for pure bending (240um and 300um) samples	78
6.4.2	Weibull plot for combined loading (240um and 300um) samples	79
6.4.3	Fractured stress histogram	79
6.4.4	Weibull plot with 95% confidence intervals	80
6.5	Statistical treatment of experimental results	81
6.5.1	Overview	81
6.5.2	Estimation of Weibull parameters	81
6.5.3	Possibility of 3-parameter Weibull model	82
6.5.4	Parametric tests	85
6.5.5	Anderson-darling test	87
6.5.6	Results of parametric tests	88
6.5.7	Non-parametric test	89
6.5.8	Results of non-parametric test	91
6.6	Explanations for differences in strength	92
6.6.1	Overview	92
6.6.2	Selection of a suitable path	92
6.6.3	Illustrations of path A and path B	95
6.6.4	Typical load factor values for path A and path B	96
6.6.5	Typical stress distribution plots	98
6.6.6	Difference between 240um and 300um pure bending	104
6.6.7	Difference between pure bending and combined loading	106
6.6.8	Difference between 240um and 300um combined bending	110
6.7	Fractography	114
6.7.1	Scaling issues in fractography	114
6.7.2	Typical size of flaw and estimation of nominal fracture stress	116
6.7.3	Pure bending fractured surface	118
6.7.4	Combined loading fractured surface	119
6.7.5	Flaws in the various regions of the beam	121

7	Extrapolation to pure torsion and proposed fracture criterion	131
7.1	Extrapolation to pure torsion	131
7.1.1	FEM model overview	131
7.1.2	Stress and load factor PDF for path A	133
7.1.3	Stress and load factor PDF for path B	134
7.1.4	Discussion and explanation	136
7.2	Proposed fracture criterion	137
7.2.1	No specific well-defined values	137
7.2.2	Need for a separate fracture criterion for each form of geometry and loading	138
8	Reliability analysis and safety design procedure	139
8.1	Overview	139
8.2	Safety design procedure	140
8.3	Results of reliability analysis based on actual experimental data	141
8.4	Case study (simulation) on effectiveness of Bayesian update	153
9	Conclusions	178
10	Future plans	179
11	References	180
12	General Readings	182
13	Acknowledgement	183

1 Research background

1.1 Social Aspect

MEMS micro-mirrors have been widely used in optical switches and scanning devices¹. For instance, “Eco-scan” from Nippon Signal Corporation is shown below in Fig 1.

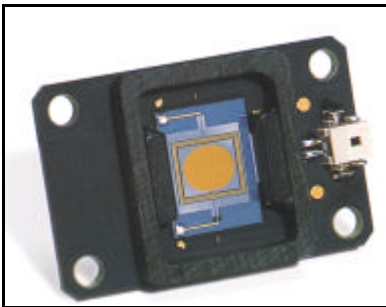


Fig1: Eco-scan from Nippon Signal Corporation

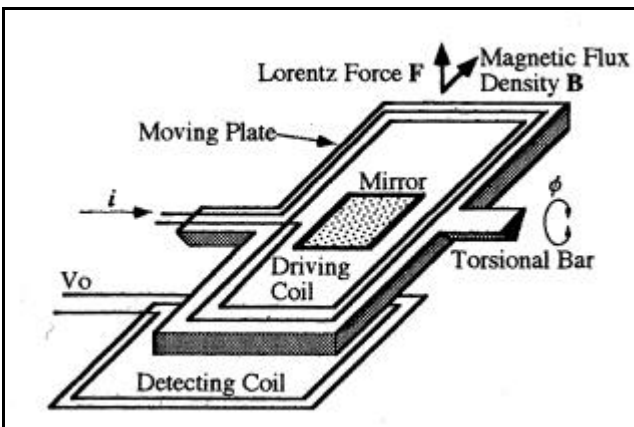


Fig 2: Working principle of the micro-mirror

Fig 2 shows the **principle of the micro-mirror**. The movement of the mirror is achieved by electromagnetic drive. Lorentz force is controlled easily by the direction and amplitude of the current flowing the driving coil fabricated on the driving plate. The driving coil is also used for detecting the rotational angle. Lorentz force vector F is given by:

$$\boxed{F = i \times B} \quad \text{-----(1)}$$

where i is the current density vector and B is the magnetic flux density vector produced by the permanent magnets. A torque T can be generated by the opposite directional Lorentz force on both sides of the torsion bar. The rotational angle ϕ is given by:

$$f = T/k \quad \text{-----(2)}$$

where k is the spring constant of torsion and can be expressed as:

$$k = GI_p/L \quad \text{-----(3)}$$

G is the shear modulus, I_p is the polar second moment of area and L is the length of the torsion bar.

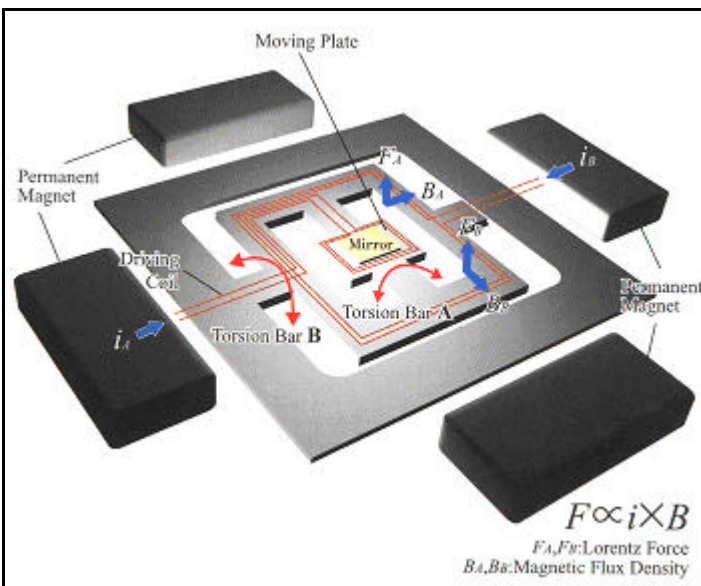


Fig 3: Structure of a two-dimensional Galvano optical scanner

Fig 3 shows the structure of the **two-dimensional Galvano optical scanner**. Two-dimensional operation can be achieved by a gimbal structure fabricated by silicon etching. (Note that there are two sets of permanent magnets). When currents i_A and i_B are applied to driving coils with magnetic fields of magnetic flux densities B_A and B_B applied in the directions perpendicular to torsion bars **A** and **B**, rotational torques are generated by Lorentz forces F_A and F_B respectively, thereby permitting the mirror to tilt to a position where the restoring forces of the torsion bars are balanced with the corresponding rotational torques. By changing the magnitudes of the currents i_A and i_B respectively, it is possible to change the tilt angles of the mirror, as desired, in the directions of the two axes.

The beams supporting the micro-mirrors are twisted and deformed largely and consequently these beams failed by brittle fracture catastrophically. **To ensure that these beams work safely and reliably, there is a need to clarify the mechanical characteristic of such beams.** For instance, the safety working

rotational angle and fracture stress of the beam. Furthermore, since the micro-mirrors are fabricated by ICP (inductively-coupled plasma) etching process, the strength characteristic of the micro-mirrors will be determined by the extent of the damage caused by etching on the surfaces of the beams. Thus, it is also possible to evaluate and estimate the strength of the beams associated with the etching process. Here, the etching process is kept as simple as possible, preferably a single mask process. (Refer to 5.1.2 for more details on the etching process)

1.2 Academic aspect

Until now, many researches have been performed to determine the mechanical characteristics of MEMS. Most of them are pure bending tests^{4,13,14,16,17,18,21} and direct tensile tests^{2,3,4,15,20,24,25}.

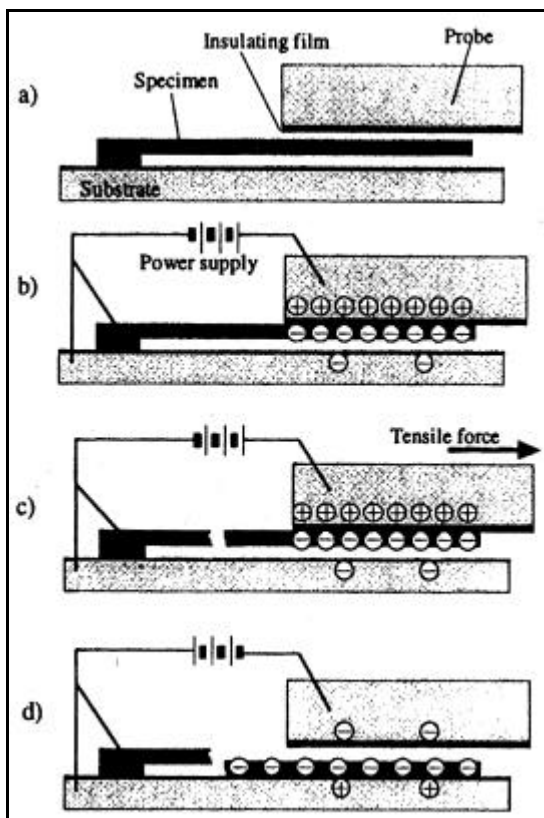


Fig 4: A schematic drawing of the tensile-testing procedure: (a) sample-to-probe alignment, (b) fixing the sample on the probe using electrostatic force, (c) applying tensile force by moving the probe and (d) releasing the fractured sample by changing the polarity applied to the probe and substrate.

A good example of direct tension testing is that performed by Tsuchiya². He found that electrostatic attraction force could be used to hold the sample during tension loading, as explain in Fig 4. Although the direct tension test is an effective method when it is properly performed and the data can be easily interpreted, the requirements for sample alignment and deflection of measurement are stringent.

For a microscale test, the task of meeting these requirements is rather challenging. Fracture testing inside a SEM chamber has the distinctive advantages of preserving the fracture surface from contamination and oxidation until observation. However, the whole measurement set-up should be compact enough to fit inside the SEM chamber.

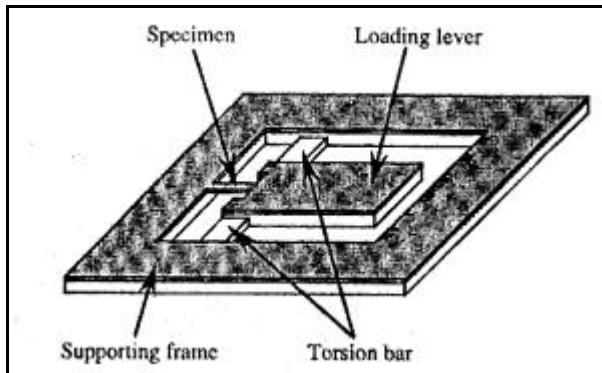


Fig 5: A schematic view of the tensile-testing chip with an integrated aid structure that direct loading

Another example of tensile test (integration of specimen and testing setup) is that performed by Sato³. He introduced an aid structure consisting of a loading lever and two torsion bars, which converted the external loading of the lever into uniaxial tension force on the tensile specimen. When a needle tip pushed down the free end of the loading lever perpendicular to the chip surface, the other end of the lever rotated about the axis of the torsion bars. This caused movement of the connecting point, where the tensile specimen was connected to the loading lever. Since the motion was small, he assumed that the point moved horizontally following a straight path and applied a pure tension to the specimen. Since the specimen and the aid structure were fabricated together lithographically, the misalignment between them could be minimal. However, the measured data includes the contribution of the aid structure as well. The effect of the torsion bars and the loading lever should be quantified and subtracted for accurate measurement and correct interpretation of data.

Most of the problems of testing microsamples with a separate measurement system can be avoided if the entire system, including the loading actuator, is made on chip⁴. However, the task of integrating the entire system is not simple. Firstly, the popular electrostatically driven comb actuators do not readily provide enough force to test mechanical properties such as fracture strength. Secondly, other microactuators require fabrication processes that are rather complicated or different from that which the specimen does. Thirdly, the microactuator need to be calibrated so that the force it delivers to the specimen can be known accurately.

Testing by bending has the advantage of being simple compared with the direct tension test. Bending test needs a smaller force than tension test but yields a lateral deformation, which is large enough to be measured using an optical microscopy. Moreover, bending method is free of the problems of sample gripping

and the method is not affected by slight misalignment in the loading direction. As such, the loading mechanism becomes relatively simple and easy to use. The bending samples can also be made smaller than a tensile-testing specimen and can be tested more easily. However, the analysis of data obtained by bending test is not straightforward due to the large deformation of the beam and the stress concentration at the boundary. Thus, both analytical and numerical approaches need to be used to help interpret the data.

A common problem with most of the present testing methods is that the etching process is quite complicated. Consequently, the damaging effects that the etching process exerts on the specimens cannot be effectively evaluated. As such, there is a need to keep the etching process simple to effectively estimate the effects etching process. Here, experiments and statistical analysis can be used in combination to correlate the damage caused by the etching process and the fracture strength of the specimens.

From an industrial and practical point of view, it is necessary to extract as many samples as possible from a single piece of wafer. As such, the interactions between the samples on the wafer have to be considered with the aid of FEM analysis. Moreover, if the specimen is of the same size as the real product, the actual working stress environment is produced and thus, more reliable and useful data can be obtained and used for actual performance. From a reliability engineering point of view, the design stress and the number of specimens needed to achieve the required level of reliability can be determined by means of probabilistic design. From a fractographic point of view, there is a need to locate the crack initiation site and identify the flaw population (flaw size and orientation). Moreover, the fracture mode (Mode I, Mode II, Mode III) should also be determined as far as possible. It is experimentally difficult to perform a pure torsion experiment. As such, combined loading (combination of pure bending and pure torsion) is performed and the effects of pure torsion can be estimated by means of the load factor analysis (refer to 3.2 for discussion on “load factor analysis”)

In conclusion, torsional loading tests^{22,23} and fractures due to torsional loading are relatively not well documented. As such, there is still much room for research relating to torsional loading tests and fractures due to torsional loading.

2 Aims of research

The first aim of the research is to design a specimen suitable for micro testing. Next, an experimental procedure for micro testing will be proposed. Then pure bending and combined loading (combination of bending and torsion) tests will be performed and a failure criterion based on the experimental data will be proposed. Finally, a general safety design procedure for microstructure under torsional loading will be proposed.

3 Theory

3.1 Weibull theory

3.1.1 Introduction

The Weibull theory has been widely used to describe the strength of brittle materials. The underlying assumptions are

- A) The defects are independent from each other i.e. they are not interacting.
- B) The material obeys the “weakest-link hypothesis”; i.e. the weakest defect causes the failure of the whole structure.
- C) A critical defect density can be defined, and the size of a critical defect is uniquely related to the strength (usually by Griffith’s law)

The Weibull theory was developed by Weibull, using the idea when one link in a chain fails, the whole chain fails. Weibull also considered multi-axial stress problems and assumed that normal tensile stress acting on a crack causes the failure of a component.

As such, this approach cannot be used to describe⁵

- A) Fracture in materials which exhibit R-curve behavior
- B) Fracture in stabilizing stress fields.

In both of these cases, stable crack growth may occur so that the flaw distribution when fracture occurs is not the same as the initial flaw distribution. Nor can the weakest link approach be used directly to describe constrained cracking such as fractures in brittle coatings or in the fragmentation of brittle fibers in composite materials. In these cases, a given fracture event may be dependent on the whole history of fracture.

The Weibull theory for an uniaxial stress state can be written as:

$$P_f = 1 - \exp \int \left\{ - \left[\frac{(s - s_{th})}{s_o} \right]^m \right\} (dA/a) \quad \text{-----(4)}$$

In equation (4), P_f is the probability of failure, A is the surface area and a is a unit area which is introduced for consistency of units. It can be seen that there are three parameters, which control the failure probability: s_o , s_{th} and m . There are, respectively, a value related to the mean strength of the brittle material, a threshold stress below, which the brittle material will not fail, and a measure of the scatter in the failure strengths of nominally identical components. s is the failure stress and, in this case, the equation is integrated over the surface area. However, most analyses ignore the threshold stress and assume that it is zero. This is done because it gives a conservative prediction and because it is much simpler to find the remaining two parameters.

3.1.2 Problems of using the Weibull theory

Because of the statistical nature of brittle fracture, there is considerable uncertainty in the estimated parameters and this leads to the question as to how many specimens need to be tested⁶. It has been shown that there can be considerable variation in the value for the Weibull modulus, m , and that the standard deviation of m divided by its mean can be approximated by $\frac{1}{\sqrt{n}}$ where n is the number of samples. This possible variation in m , caused by a finite sample size, can lead to errors in the prediction of component failure stresses.

A further problem arises as to the failure origin. The failure theories can be based on an integral over the surface or over the volume. The surface integral can account for surface damage due to machining and for pores and cracks, which penetrate the surface. The volume integral can account, in addition, for internal cracks and porosity. It is possible that both surface and volume flaws are present. Specimen failure will depend on whether the surface or volume flaw is the most critical and this will vary with loading condition and specimen geometry. Specimen failure depending on the surface or volume flaw will be based on the 'effective surface' or 'effective volume' model respectively. Recently, a new model, namely the 'effective shell' model⁷, which is a combination between the effective surface and effective volume model, has been introduced.

An underlying assumption of using equation (4) to describe the failure strength is that there exists a single unimodal flaw distribution. Specifically, a unimodal flaw distribution will mean that there is just one fixed size and one fixed orientation distribution. However, in reality, there may be more than one flaw distribution (a bimodal or even a trimodal) in the specimens. Different flaw distributions can be attributed to the different orientation of the flaws at different locations or locations of the flaws (surface, volume). Moreover, the loading method (combined loading, pure bending or pure torsion) or geometry of the specimen may have led to a seemingly bimodal or trimodal flaw distribution.

The concept of "concurrent flaws" has been introduced in some literature⁹. For instance, "concurrent flaws", which means present in all volumes, may be the result of two different flaw distributions existing in the same single specimen. The 'concurrent flaws' can be modeled using the multiplicative bimodal Weibull distribution. Moreover, another approach, namely the "non-concurrent flaw", which means not present in all volumes (for example, scratches originating from a grinding procedure, which occur for only some specimens), can be modeled by an additive bimodal Weibull distribution.

Theoretically, the bimodal Weibull distribution can be identified graphically by the appearance of two conspicuous peaks in the PDF plot. However, in reality, if the flaw distribution cannot be identified in the first place, the strength distribution is thus unknown. Thus, strength tests are initially performed and failure strengths are then obtained and the Weibull plot made. When the experimental data are treated

using the Weibull plot, identification of a bimodal flaw distribution is difficult. As such, when treating experimental data using the Weibull plot, the underlying bimodal flaw distribution may go unnoticed.

3.1.3 Significance of the Weibull modulus m

The Weibull modulus defines the width of the probability distribution. If m is large, the distribution is narrow, showing a small spread of failure strength. If m is small, the distribution is wide, showing a large variation in failure strength. Poor ceramics have m in the range of 3~10. Good engineering ceramics have m in the range of 10~40, usually closer to 10 except for high toughness materials. In short, it can be assumed that the Weibull modulus m is representative of the homogeneity of the flaw distribution¹⁰. A larger Weibull modulus m will signify a more homogeneous sample.

3.1.4 Estimating the Weibull parameters using the Maximum Likelihood Estimator (MLE)

The method of maximum likelihood is a commonly used procedure because it shows the smallest coefficient of variation⁶. Let $x_1, x_2, x_3, x_4, \dots, x_n$ be a random sample of size n drawn from a probability density function, $f_x(x; \theta)$, where θ is an unknown parameter. The likelihood function of this random sample is the joint density of the n random variables and is a function of the unknown parameter.

$$L = \prod_{i=1}^n f_{x_i}(x_i, \theta) \quad \text{-----(5)}$$

Thus equation (5) shows the likelihood function. The maximum likelihood estimator (MLE) of θ , say $\hat{\theta}$, is the value of θ that maximizes L or, equivalently, the logarithm of L . Often, but not always, the MLE of θ is a solution of equation (6)

$$\frac{d \log L}{d \theta} = 0 \quad \text{-----(6)}$$

where solutions that are not functions of the sample values $x_1, x_2, x_3, x_4, \dots, x_n$ are not admissible, nor are solutions which are not in the parameter space. Now, we are going to apply the MLE to estimate the Weibull parameters, namely the shape β and the scale η parameters. Consider the Weibull PDF (equation (7)):

$$f(x) = \frac{\beta}{h} \left(\frac{x}{h} \right)^{\beta-1} e^{-\left(\frac{x}{h} \right)^\beta} \quad \text{-----(7)}$$

Then likelihood function will be shown in equation (8):

$$L(x_1, \dots, x_n; \mathbf{b}, \mathbf{h}) = \prod_{i=1}^n \left(\frac{\mathbf{b}}{\mathbf{h}} \right) \left(\frac{x_i}{\mathbf{h}} \right)^{\mathbf{b}-1} e^{-\left(\frac{x_i}{\mathbf{h}} \right)^{\mathbf{b}}} \quad \text{-----(8)}$$

On taking the logarithms, differentiating with respect to \mathbf{b} and \mathbf{h} in turn and equating to zero, we obtain the estimating equations (9) and (10):

$$\frac{\partial \ln L}{\partial \mathbf{b}} = \frac{n}{\mathbf{b}} + \sum_{i=1}^n \ln x_i - \frac{1}{\mathbf{h}} \sum_{i=1}^n x_i^{\mathbf{b}} \ln x_i = 0 \quad \text{-----(9)}$$

$$\frac{\partial \ln L}{\partial \mathbf{h}} = -\frac{n}{\mathbf{h}} + \frac{1}{\mathbf{h}^2} \sum_{i=1}^n x_i^{\mathbf{b}} = 0 \quad \text{-----(10)}$$

On eliminating \mathbf{h} between these two equations and simplifying, we have equation (11):

$$\frac{\sum_{i=1}^n x_i^{\mathbf{b}} \ln x_i}{\sum_{i=1}^n x_i^{\mathbf{b}}} - \frac{1}{\mathbf{b}} - \frac{1}{n} \sum_{i=1}^n \ln x_i = 0 \quad \text{-----(11)}$$

which may be solved to get the estimate $\hat{\mathbf{b}}$. This can be accomplished by the use of standard iterative procedures (i.e., Newton-Raphson method). Once $\hat{\mathbf{b}}$ is determined, $\hat{\mathbf{h}}$ can be estimated by:

$$\hat{\mathbf{h}} = \frac{\sum_{i=1}^n x_i^{\hat{\mathbf{b}}}}{n} \quad \text{-----(12)}$$

3.2 Load factor analysis

3.2.1 Definition

For a more general case, the load factor is defined as shown in equation (13):

$$\boxed{\text{load factor} = \frac{1}{\text{volume}} \iiint_{\text{region}} (f(x, y, z))^m dx dy dz} \text{-----(13)}$$

whereby $f(x, y, z) = \frac{s(x, y, z)}{s_{\text{nominal}}}$ is the position function and m is the Weibull modulus.

The position function $f(x, y, z)$ is a dimensionless stress function and gives the ratio of the stress at a particular position $s(x, y, z)$ with respect to s_{nominal} , which is often taken to be the maximum principal stress for the case of brittle fracture. For a line of flaw under stress is defined as, the load factor which in this case also known as the stress-length integral (shown in equation (14):

$$\boxed{\text{load factor} = \frac{1}{L} \int_0^L (f(l))^m d(l)} \text{-----(14)}$$

whereby L is the length of the flaw under consideration.

3.2.2 Interpretation

Since the stress varies with position and is not uniformly distributed across the concerned dimension (length or area or volume), there is a need for an index (load factor) that shows the intensity of the stress distribution with respect to the case when the stress does not vary with position and is uniformly distributed across the concerned dimension.

The load factor in the case of uniform tensile stress acting on the concerned dimension is one. For all the other cases, namely pure bending, combined loading and pure torsion, the load factor is less than one.

The load factor is path-dependent, meaning that its value will change depending on the location of the integration path.

3.2.3 Load factor PDF (probability density function)

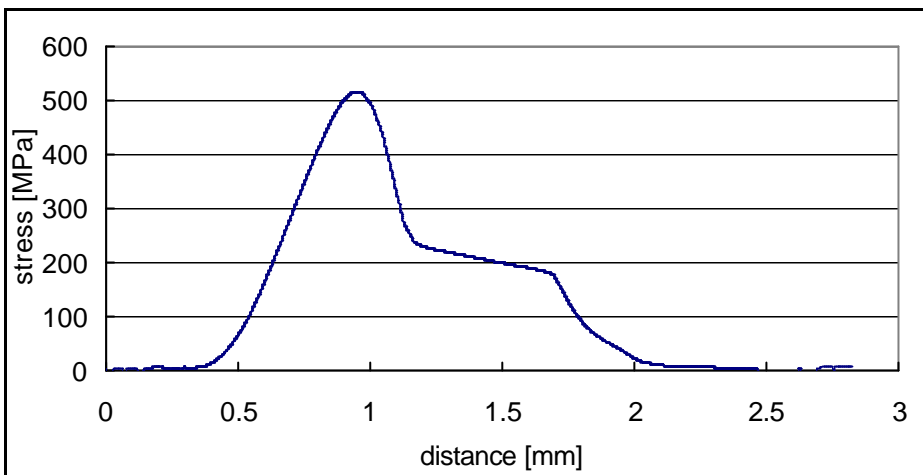


Fig 4: A typical stress distribution along the edge length of beam

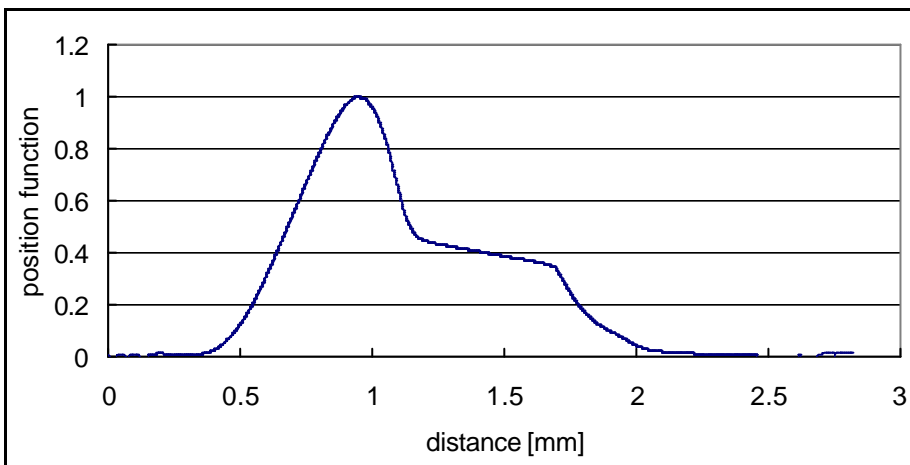


Fig 5: Position function is obtained by dedimensionalizing the stress distribution with a nominal stress (usually the maximum stress in the region concerned)

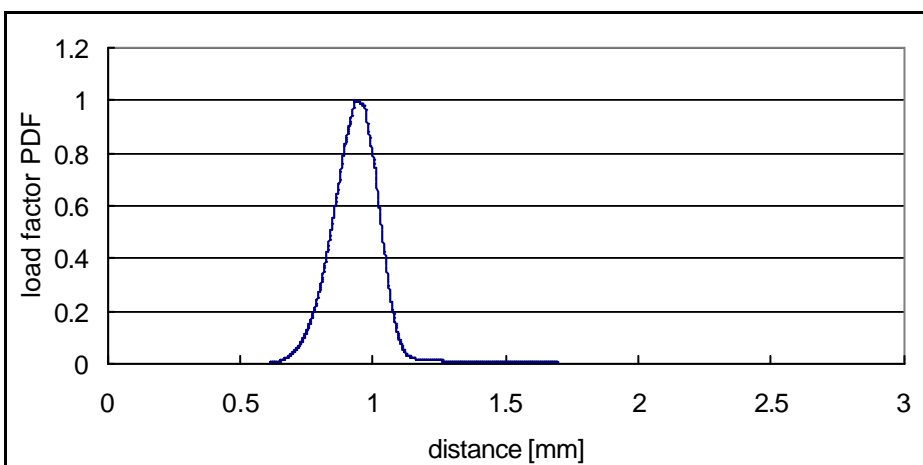


Fig 6: Load factor PDF is obtained by raising the value of the position function to the power of Weibull modulus

The peak maximum value of the load factor PDF is always one. One can construct a load factor PDF and used it to locate regions of stress severity. Such a load factor PDF can be used to compare samples with different fracture stresses since the load factor PDF like the load factor is a constant for a particular loading mode and geometry. Note that the load PDF graph (Fig 6) is much narrower than the stress graph (Fig 4 and Fig 5) and it implies that the region of severe stress and high fracture probability is concentrated to a narrow region.

$$\boxed{\text{load factor PDF} \propto \text{severity of stress distribution}} \quad \text{-----(15)}$$

3.2.4 Load factor CDF (cumulative distribution function)

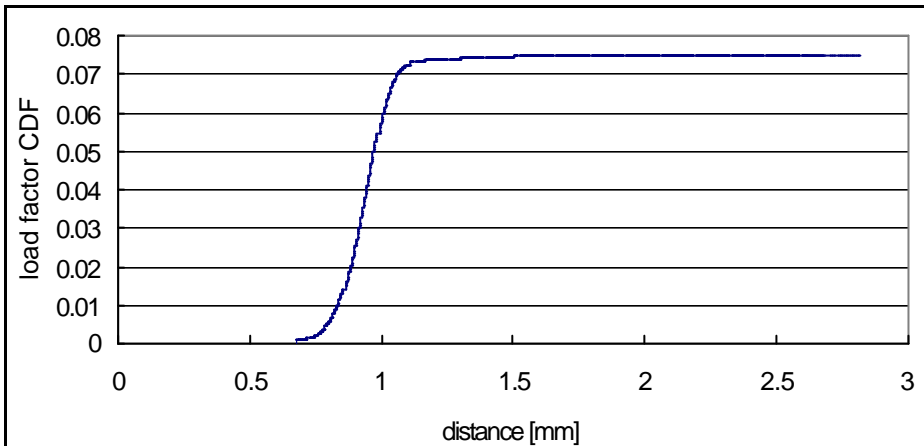


Fig 7: Load factor CDF obtained by integrating the load factor PDF

The maximum value of the load factor CDF gives the load factor for a particular geometrical and loading system. The load factor CDF like both the load factor and load factor CDF is a constant for a particular loading mode and geometry.

3.2.5 Other essential points

- No reference is made about the nature of the flaw PDF, which is assumed uniform in the concerned dimension. Since the definition of the load factor originated from the Weibull PDF, it is assumed that the flaws are independent: i.e. no interactions between the flaws.
- The stress function to be used in the analysis of the load factor is not specified. However, for the case of brittle material, the stress function used is normally taken to be the principal stress function
- The load factor obtained from a mode of loading cannot be directly compared to another mode. For instance, a load factor obtained for a pure bending cannot be compared directly with that compared from a combined loading since the direction of the principal stresses are different for the two cases. On the other hand, for the case of pure bending, since the direction of the principal is the same as that in the case of the uniform normal tensile stress, comparison can be made. Besides, load factor obtained for the case of the combined loading can also be compared to a certain extent with that obtained for the case of pure torsion.
- A higher load factor, i.e. a load factor that is closer to the value of one will be “penalized” less in the cumulative failure probability distribution. Thus, the load factor can be interpreted as follows:

$$\boxed{\text{load factor} \propto \frac{1}{\text{penalty}}} \quad \text{-----(16)}$$

- Load factor, load factor PDF and load factor CDF are the same for all the different fractured stress of the same geometry and loading mode. Thus, one can use the load factor to characterize the stress distribution for a particular type of geometry and mode of loading.

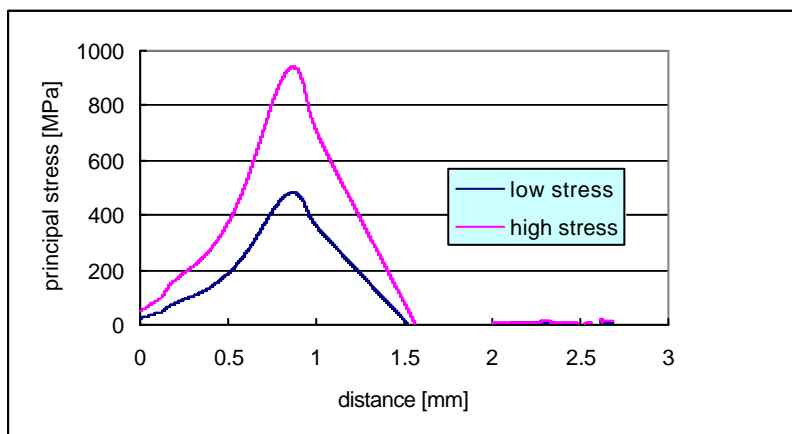


Fig 8: Principal stress distribution for two extreme cases: high fractured stress and low fracture stress along the edge length of the beam

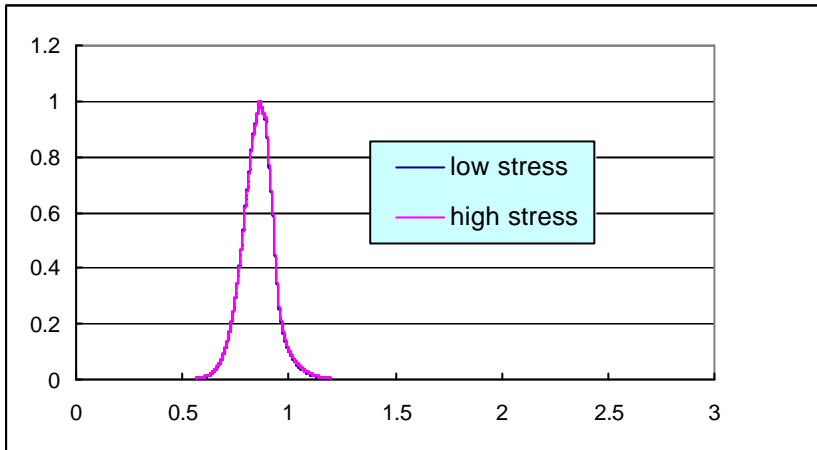


Fig 9: Load factor PDF for two extreme cases: high fractured stress and low fracture stress (300um pure bending)

- Relationship between Weibull modulus and the load factor is given below:

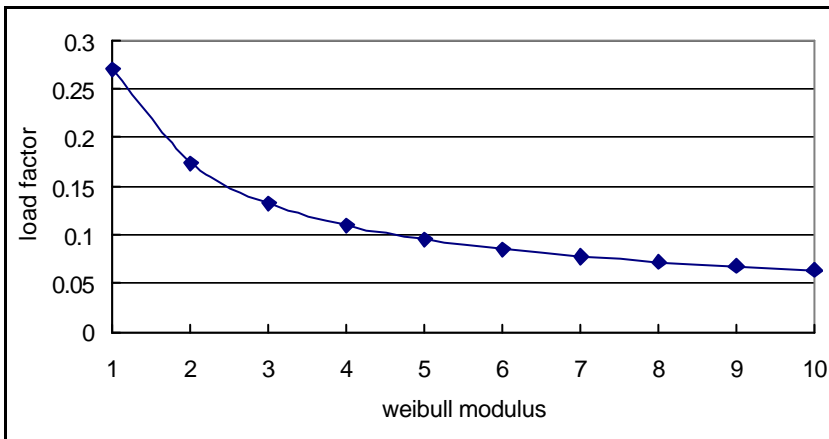


Fig 10: Relationship between Weibull modulus and load factor

The load factor is inversely proportional to the Weibull modulus (Fig 10). As the Weibull modulus becomes larger, the load factor PDF becomes narrow and as a result, the load factor CDF has a lower peak, which in turn implies a lower value for the load factor.

3.3 FEM modeling

3.3.1 Necessity of FEM analysis and accurate experimental displacement

Since the specimen geometry is complicated, FEM analysis is indispensable to the estimation of the fracture stress. Moreover, it should be considered together with experiment. Hence, it is important that the result obtained from the FEM analysis is reliable. In the case of pure bending, accurate experimental displacement can be obtained by measuring the specimen's displacement with the LDM (laser displacement meter). The experimental displacement is used to ensure that result from the FEM analysis is reliable. In the case of combined loading, accurate LDM experimental displacement is not available. This is because the beam surface and the laser head are not parallel to each other after the beam undergoes relatively large downward displacement and the laser spot reflected off the beam surface cannot be captured by the laser head. However, since the specimen is depressed at the 5th or 4th hole, stiffness (spring constant) is relatively low and thus, the experimental displacement from the EZTest (bore screw displacement) can still be used as a form of guidance. (Note: in this research, 2 types of experimental displacement are available: LDM and EZTest displacement: bore screw displacement)

3.3.2 Submodeling

Submodeling is a finite element technique used to obtain more accurate results in a region of interest in the FEM model. Often, in FEM analysis, the finite element mesh may be too coarse to produce satisfactory results in a region of interest such as a stress concentration region. The results away from this region, however, may be adequate. To obtain accurate results in such a region, you have two options:

- a) Reanalyze the entire model with greater mesh refinement
- b) Generate an independent, more finely meshed mesh model of only the region of interest and analyze it

Submodeling is also known as the cut-boundary displacement method or the specified boundary displacement method. The cut boundary is the boundary of the submodel, which represents a cut through the coarse model. Displacements calculated on the cut boundary of the coarse model are specified as boundary conditions for the submodel

Submodeling is based on the St. Venant's principle: If an actual distribution of forces is replaced by a statically equivalent system, the distributions of stress and strain are altered only near the regions of load application. This implies that stress concentration effects are localized around the concentration. Therefore, if the boundaries of the submodel are far enough away from the stress concentration, reasonably accurate results can be calculated in the submodel. Aside from the

obvious benefit of giving you results that are more accurate in a region of your FEM model, the submodeling has other advantages:

- a) It reduces, or even eliminates, the need for complicated transition regions in solid finite element models
- b) it enables you to experiment with different designs for the region of interest (different fillet radius, etc.)
- c) it helps you in demonstrating the adequacy of mesh refinements

Some restrictions for the use of submodeling (in ANSYS) are:

- a) It is valid only for solid elements and shell elements
- b) The principle behind submodeling assumes that the cut boundaries are far enough away from stress concentration region. Hence, the cut-off boundary should not be in a region of high stress region and the location of the cut-boundary is essential to the accuracy of submodeling.

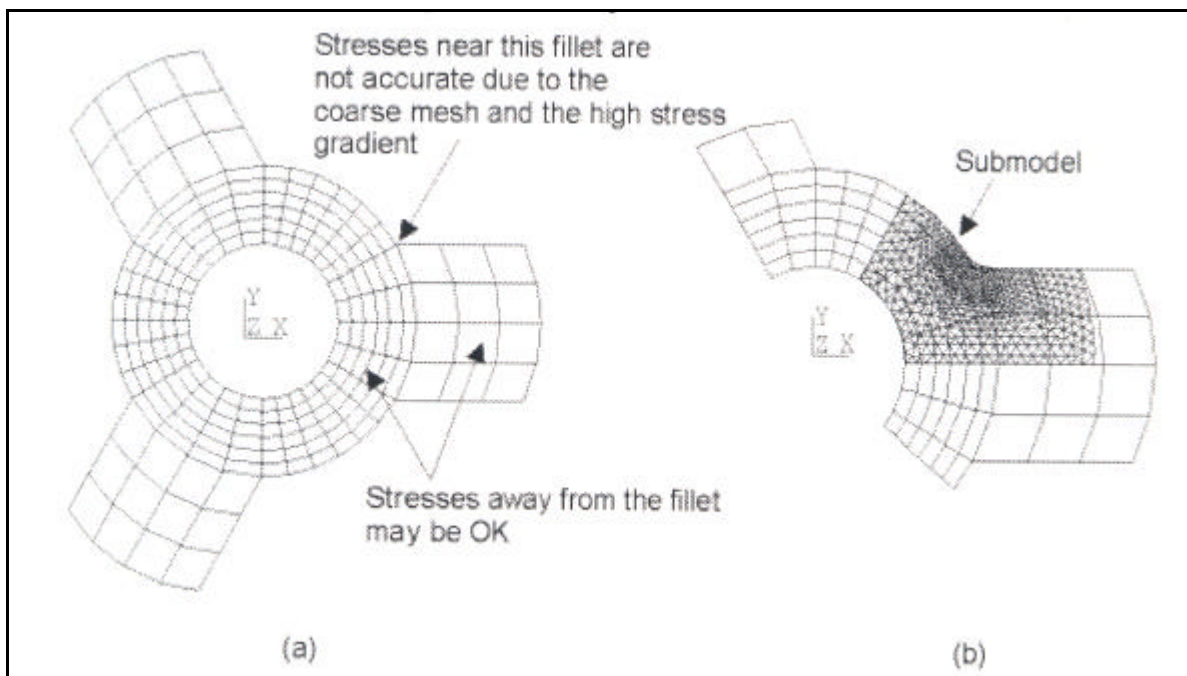


Fig 11: Submodeling of a pulley hub and spokes: (a) coarse model, (b) submodel shown superimposed over the coarse model

3.3.3 Construction of a good initial FEM model based on pure bending experimental results

To ensure that the FEM model constructed is accurate, LDM displacement from pure bending experiment was compared with that obtained from the FEM model. Since material constant is fixed, the thickness of the wafer and the extent of the sub model are the only variables. The thickness of the wafer can be estimated in two ways:

- 1) It can be measured directly using the LDM and then inputted into the FEM model.
- 2) Determined from an interpolation procedure.

When the experiment displacement matches the FEM displacement, one can use the FEM model to predict the fracture stress. Here, the initiation of the crack is determined by fractography, which is used together with the FEM model to pinpoint the fracture stress in the interested region. **However, it should be noted that matching of displacement between the FEM and experiment is a necessary but not sufficient condition.** Displacement can be matched accurately and yet the fracture stress obtained could be inaccurate or meaningless as being observed in the case of using the shell element or tetrahedron element to model the beam. Furthermore, FEM stress result should be analyzed in accordance with fractured stress estimated from conventional Weibull theory to ensure that the results obtained are reliable and meaningful.

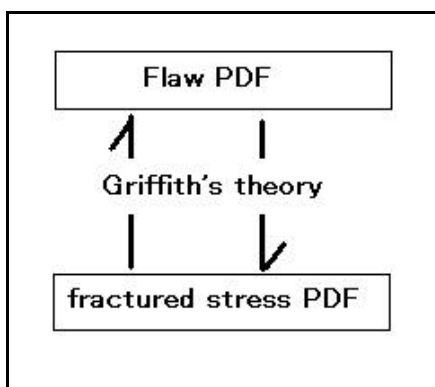


Fig 12: Relationship between the flaw PDF and fractured stress PDF

Usually the flow is from the top to bottom. The flaw PDF is first identified and then the fractured stress PDF can be estimated using the Griffith's theory. In this research, the flow goes both ways.

3.3.4 Problems of the different types of FEM elements

Solid 95

SOLID95 is a higher order version of the 3-D 8-node solid element SOLID45. It can tolerate irregular shapes without as much loss of accuracy. SOLID95 elements have compatible displacement shapes and are well suited to model curved boundaries. The element is defined by 20 nodes having three degrees of freedom per node: translations in the nodal x, y, and z directions. The element may have any spatial orientation. SOLID95 has plasticity, creep, stress stiffening, large deflection, and large strain capabilities.

Shell 93

SHELL93 is particularly well suited to model curved shells. The element has six degrees of freedom at each node: translations in the nodal x, y, and z directions and rotations about the nodal x, y, and z-axes. The deformation shapes are quadratic in both in-plane directions. The element has plasticity, stress stiffening, large deflection, and large strain capabilities.

Shell elements are used to model structures whose one dimension (the thickness) is much smaller than the other dimensions. Because of this assumption, the stresses through the thickness of the shell are assumed negligible. In this research, the Shell93 (quadratic shell element) is used to model the deformation of the whole wafer and hexahedron Solid95 is used to model the each specimen. **It is advisable not to use Shell93 element and tetrahedron Solid95 to model the beam of each specimen.** For the case of the Shell93 element, the traverse shear stresses SYZ and SXZ (Fig 13 and Fig 15) are assumed constant through the thickness. Compare these with that for hexahedron Solid 95: Fig 14 and Fig 16. Such assumptions will result in erroneous principal stress, which is used to estimate the fracture stress. Thus, the principal stress calculated along the length of the beam will be wrong too.

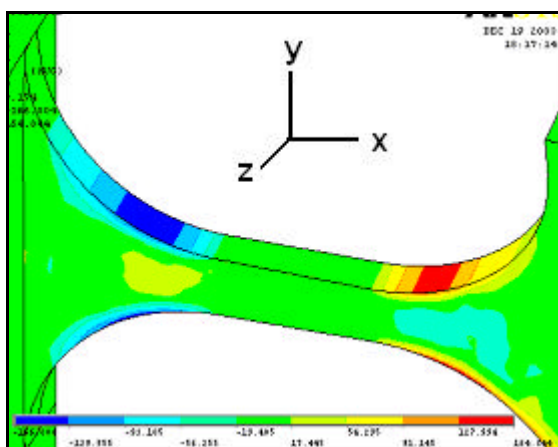


Fig 13: Shear stress SYZ distribution for Shell 93

[Note: The axis direction will be the same as that in Fig 13 throughout the thesis]

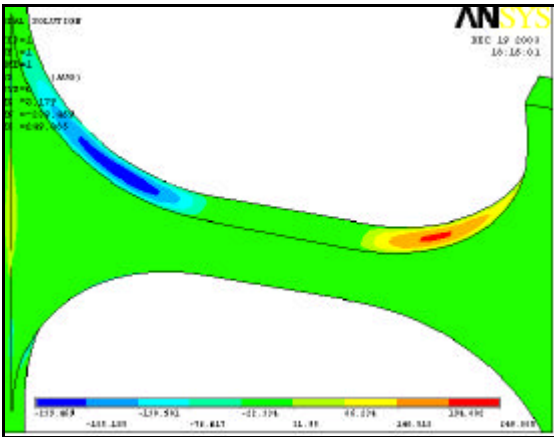


Fig 14: Shear stress SYZ distribution for hexahedron Solid 95

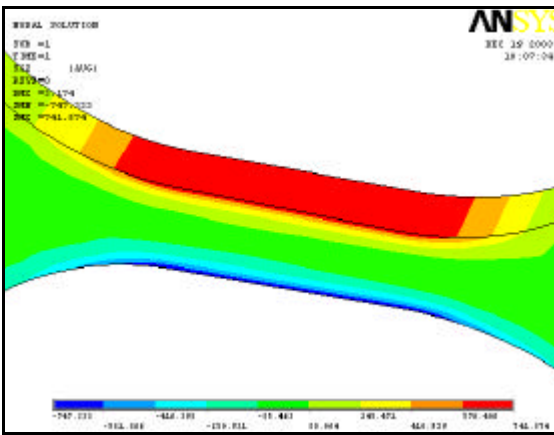


Fig 15: Shear stress SXZ distribution for Shell 93

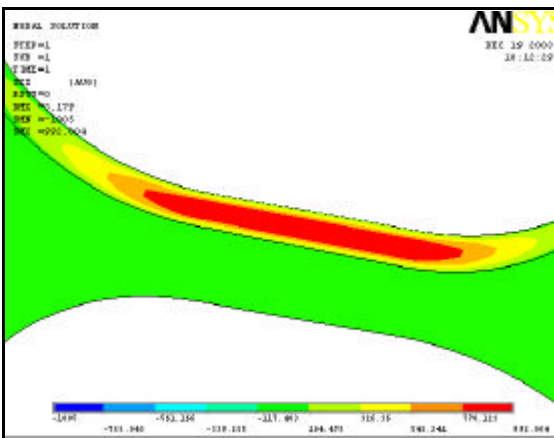


Fig 16: Shear stress SXZ distribution for hexahedron Solid 95

When **tetrahedron Solid95** is used to model the beam, there seems to be inaccurate nodal stress interpolation problem. (Fig 17 and Fig 18). Although the magnitudes of the stress are of the same order, for the case of tetrahedron Solid95, the edges of the shear stress SXY contour plot are zigzagged. For the case of the hexahedron Solid95 (Fig 19 and Fig 20), the edges of contour plots are smooth.

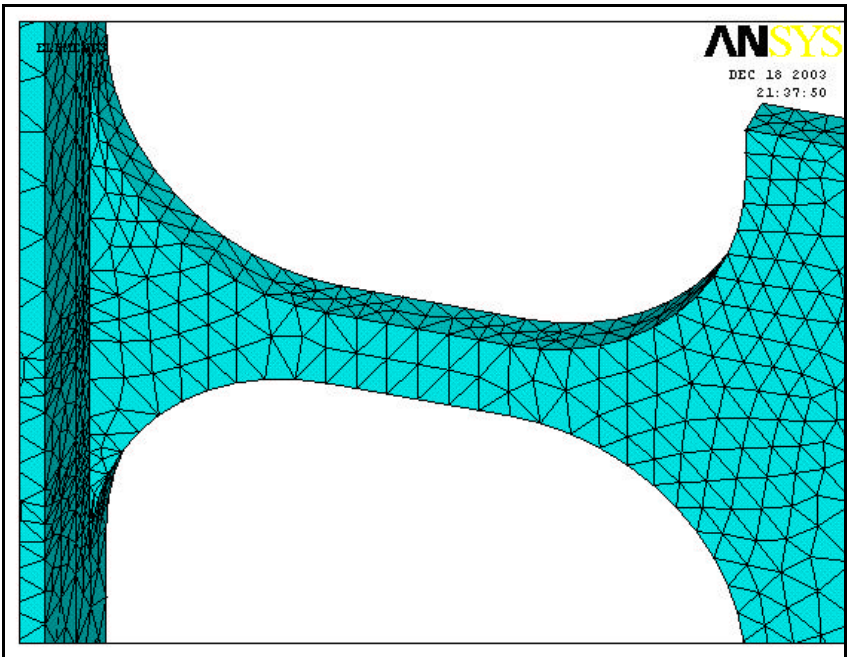


Fig 17: Mesh for tetrahedron Solid 95

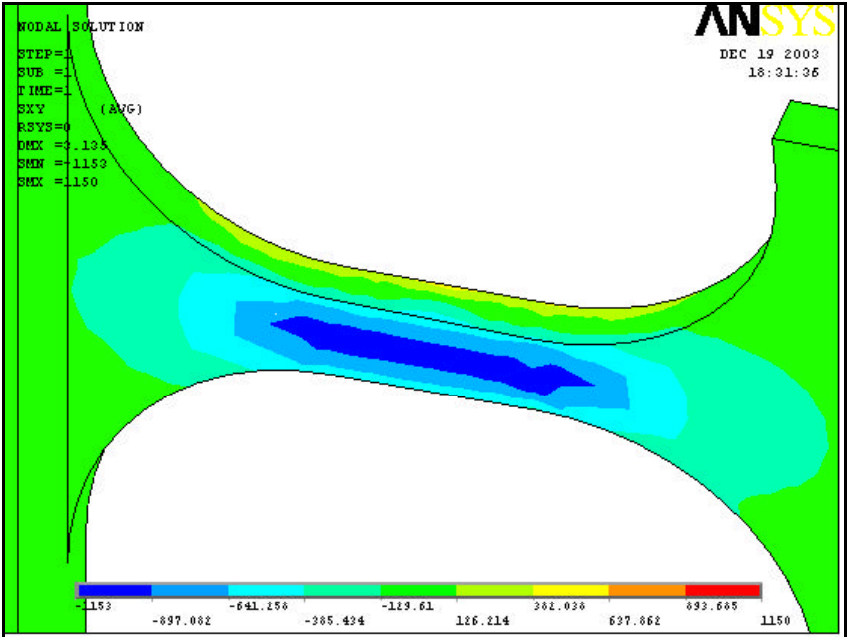


Fig 18: Shear stress SXY distribution for tetrahedron Solid 95

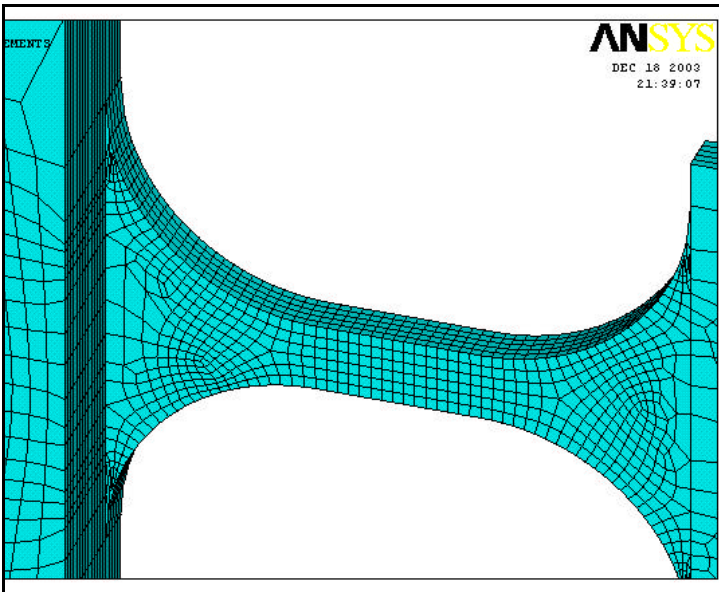


Fig 19: Mesh for hexahedron Solid 95

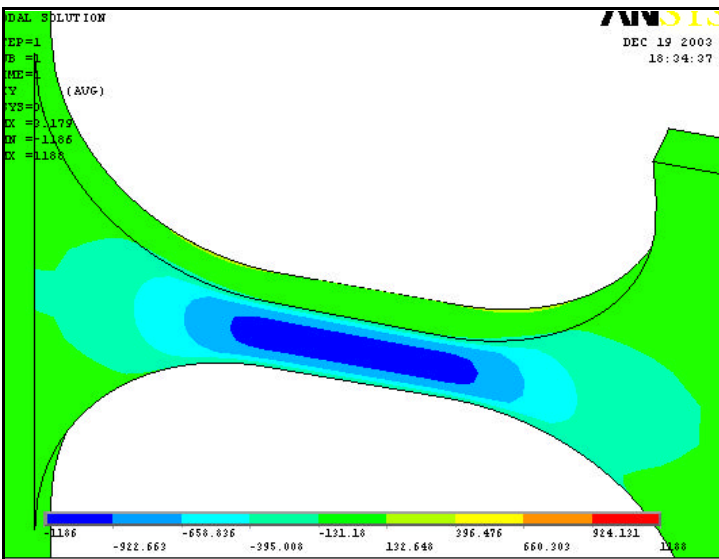


Fig 20: Shear stress SXY distribution for hexahedron Solid 95

In conclusion, Hexahedron Solid95 is used to construct the beam in view of the problems associated with shell and tetrahedron elements. The height of the beam consists of five layers of elements. When only 3 layers of elements are used, the edges of stress contour plot are zigzagged. When 5 layers of elements are used, the edges of stress contour plot become smoother. The displacements from both models are almost the same. (3-layered: 2.827mm 468MPa; 5-layered: 2.828 440MPa for a typical combined loading FEM analysis).

Note: As far as displacement is concerned, the different elements (shell 93, tetrahedron solid 95, hexahedron solid 95) give almost the same displacement (almost 100% matching). Shell 93 elements cannot be used to evaluate through thickness stress and tetrahedron solid 95 elements has low accuracy for nodal

stress interpolation along straight path. Hence, hexahedron solid 95 is suitable for analysis of nodal stress interpolation along relatively straight path.

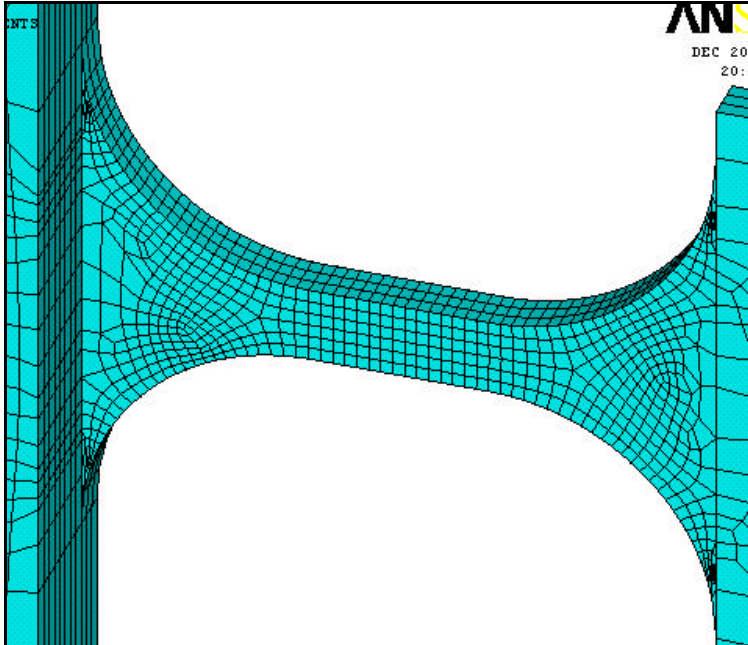


Fig 21: 3-layered FEM model

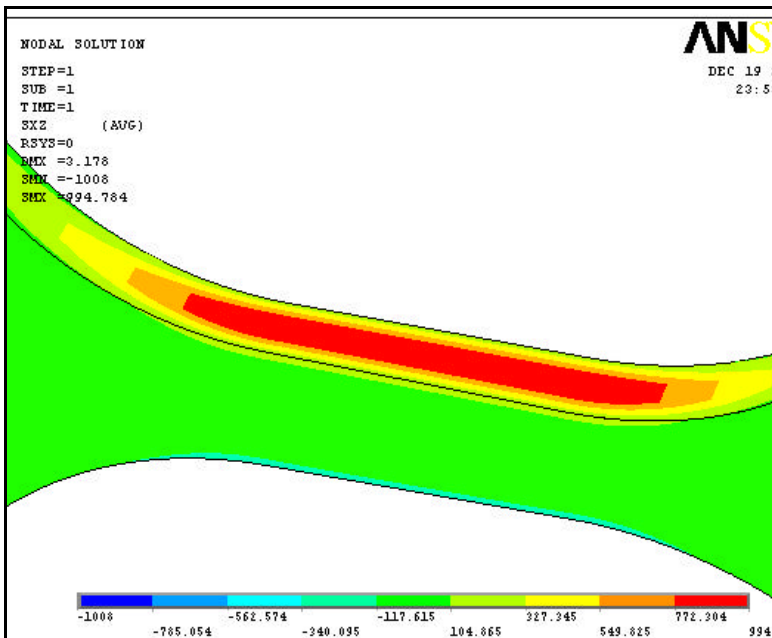


Fig 22: Shear stress SXZ distribution for 3-layered FEM model

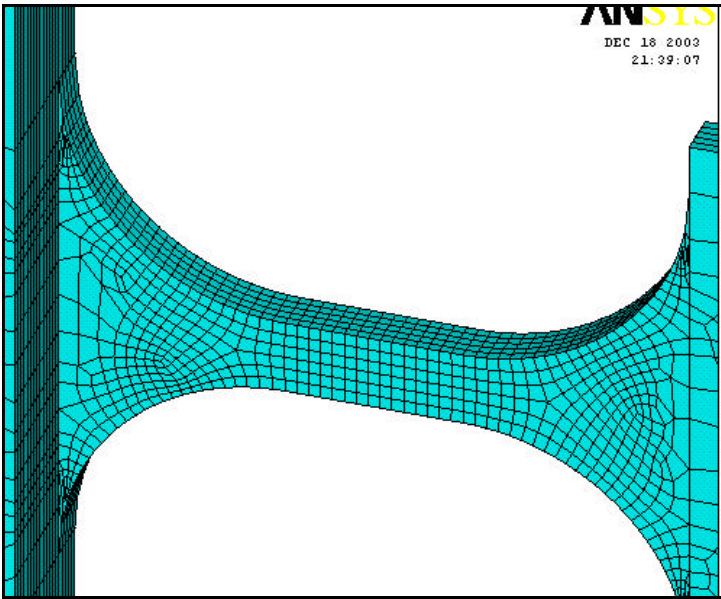


Fig 23: 5-layered FEM model

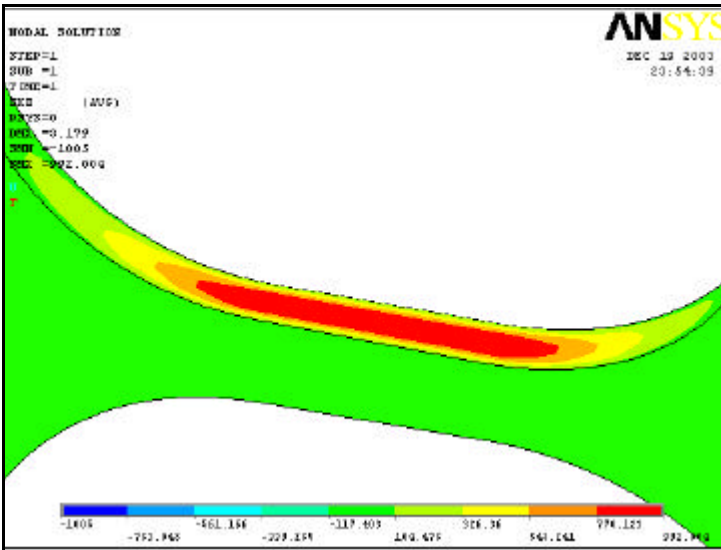


Fig 24: Shear stress SXZ distribution for 5-layered FEM model

3.3.5 Relationship between the site of crack initiation and the maximum principal stress

The determination of the crack initiation site is not simple, but can be inferred to a certain extent with the aid of fractography and FEM analysis. For brittle material, the maximum principal stress is often used as the fracture criterion: i.e. failure is expected when the largest principal normal stress reaches the uniaxial strength of the material expressed below in equation (17):

$$\mathbf{s}_{fracture} = MAX(|\mathbf{s}_1|, |\mathbf{s}_2|, |\mathbf{s}_3|) \text{ at fracture} \text{ -----(17)}$$

(Assumption: tensile strength and compressive strength is the same)

If there is a single type flaw of a particular size (uniform flaw distribution at all locations) and the geometry of the stressed specimen is simple (for instance, a straight rectangular beam with no fillet), one could say that the crack initiation site would coincide with the location of the maximum principal stress along the edge length of the beam.

However, in reality, the flaw exhibits a non-uniform size distribution (size PDF) and orientation PDF. As a result, the location of the crack initiation site may not coincide with the location of maximum principal stress. For instance, a particular location may show a maximum principal stress when stressed. The site of crack initiation may be at another location where a more critical flaw exists but exhibits a lower principal stress.

Hence, the use of the maximum principal stress as the prediction of the crack initiation stress could be an over-estimation of the actual crack initiation stress. From a design point of view, if one were to assume a higher strength distribution when the actual strength distribution is lower, one will underestimate the failure probability, which could be detrimental. However, if the flaw distribution is not highly skewed in the region of consideration, the use of the maximum principal stress is appropriate.

3.3.6 Degree of fineness of mesh

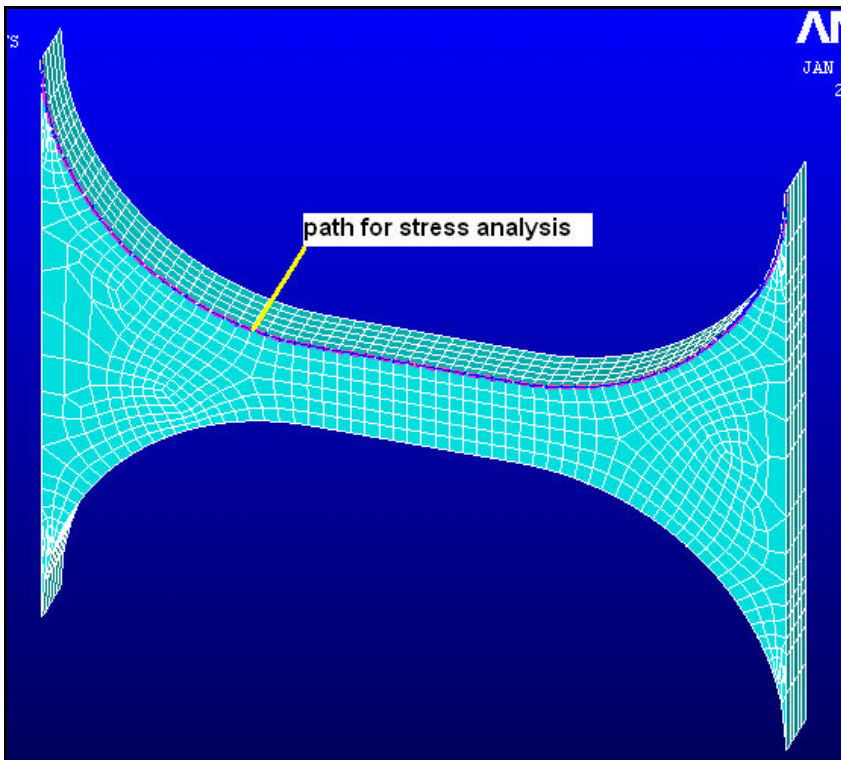


Fig 25: Fine mesh

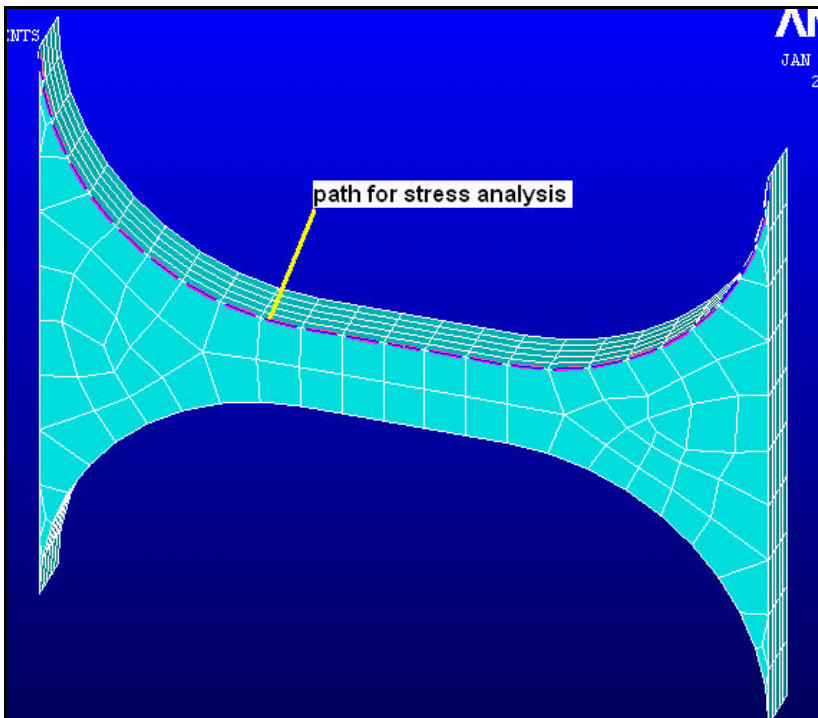


Fig 26: Rough mesh

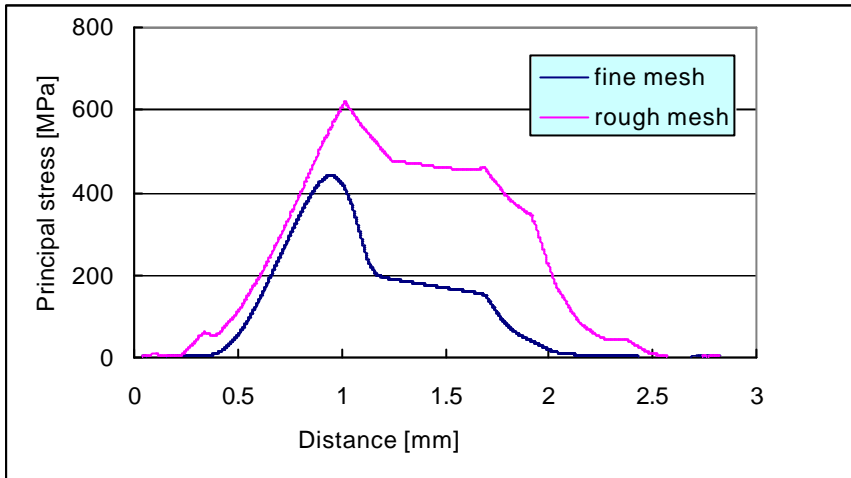


Fig 27: Stress comparison for different levels of meshing (combined loading 240um) along the path indicated

There seems to be an overestimation of the principal stress when the mesh is rough. For consistency, the same meshing is used for the submodels in different parts of the wafer.

3.3.7 Anisotropic material constant for silicon

The general Hooke's law is given as:

$$\mathbf{s}_{ij} = C_{ijkl} \mathbf{e}_{kl} \quad \text{-----(18)}$$

$$\mathbf{e}_{ij} = S_{ijkl} \mathbf{s}_{kl} \quad \text{-----(19)}$$

whereby $i, j, k, l = 1, 2, 3$

\mathbf{s}_{ij} : Stress tensor (9 components)

\mathbf{e}_{kl} : Strain tensor (9 components)

C_{ijkl} : Stiffness coefficient (81 components)

S_{ijkl} : Compliance coefficient (81 components)

Stiffness matrix of cubic crystal for (001) orientation:

$$\begin{bmatrix} \mathbf{s}_1 \\ \mathbf{s}_2 \\ \mathbf{s}_3 \\ \mathbf{s}_4 \\ \mathbf{s}_5 \\ \mathbf{s}_6 \end{bmatrix} = \begin{bmatrix} C_{11} & C_{12} & C_{12} & 0 & 0 & 0 \\ C_{12} & C_{11} & C_{12} & 0 & 0 & 0 \\ C_{12} & C_{12} & C_{11} & 0 & 0 & 0 \\ 0 & 0 & 0 & C_{44} & 0 & 0 \\ 0 & 0 & 0 & 0 & C_{44} & 0 \\ 0 & 0 & 0 & 0 & 0 & C_{44} \end{bmatrix} \begin{bmatrix} \mathbf{e}_1 \\ \mathbf{e}_2 \\ \mathbf{e}_3 \\ \mathbf{e}_4 \\ \mathbf{e}_5 \\ \mathbf{e}_6 \end{bmatrix} \quad \text{-----(20)}$$

\mathbf{s}_{ij} : Stress tensor (6 components):

$$\begin{bmatrix} \mathbf{s}_1 = \mathbf{s}_{11} \\ \mathbf{s}_2 = \mathbf{s}_{22} \\ \mathbf{s}_3 = \mathbf{s}_{33} \\ \mathbf{s}_4 = \mathbf{s}_{23} = \mathbf{s}_{32} \\ \mathbf{s}_5 = \mathbf{s}_{13} = \mathbf{s}_{31} \\ \mathbf{s}_6 = \mathbf{s}_{12} = \mathbf{s}_{21} \end{bmatrix} \quad \text{-----(21)}$$

\mathbf{e}_{ij} : Stress tensor (6 components):

$$\begin{bmatrix} \mathbf{e}_1 = \mathbf{e}_{11} \\ \mathbf{e}_2 = \mathbf{e}_{22} \\ \mathbf{e}_3 = \mathbf{e}_{33} \\ \mathbf{e}_4 = \mathbf{e}_{23} = \mathbf{e}_{32} \\ \mathbf{e}_5 = \mathbf{e}_{13} = \mathbf{e}_{31} \\ \mathbf{e}_6 = \mathbf{e}_{12} = \mathbf{e}_{21} \end{bmatrix} \quad \text{-----(22)}$$

C_{ijkl} : Stiffness coefficient (3 components)

$$\begin{bmatrix} C_{ijkl} = C_{mn} \\ ij(kl) \rightarrow m(n) \\ 11 \rightarrow 1, \\ 22 \rightarrow 2 \\ 33 \rightarrow 3 \\ 23 \rightarrow 4 \\ 13 \rightarrow 5 \\ 12 \rightarrow 6 \end{bmatrix} \quad \text{-----(23)}$$

Compliance matrix of cubic crystal:

$$\begin{bmatrix} \mathbf{e}_1 \\ \mathbf{e}_2 \\ \mathbf{e}_3 \\ \mathbf{e}_4 \\ \mathbf{e}_5 \\ \mathbf{e}_6 \end{bmatrix} = \begin{bmatrix} S_{11} & S_{12} & S_{12} & 0 & 0 & 0 \\ S_{12} & S_{11} & S_{12} & 0 & 0 & 0 \\ S_{12} & S_{12} & S_{11} & 0 & 0 & 0 \\ 0 & 0 & 0 & S_{44} & 0 & 0 \\ 0 & 0 & 0 & 0 & S_{44} & 0 \\ 0 & 0 & 0 & 0 & 0 & S_{44} \end{bmatrix} \begin{bmatrix} \mathbf{s}_1 \\ \mathbf{s}_2 \\ \mathbf{s}_3 \\ \mathbf{s}_4 \\ \mathbf{s}_5 \\ \mathbf{s}_6 \end{bmatrix} \quad \text{-----(24)}$$

Compliance coefficient on silicon (001) rotated in the [001] direction as shown in the Fig 28 below:

$$[S_{ij}] = \begin{bmatrix} S_{11} - \frac{1}{2} S_c [\sin(2q)]^2 & S_{12} + \frac{1}{2} S_c [\sin(2q)]^2 & S_{12} & 0 & 0 & -\frac{1}{2} S_c [\sin(4q)] \\ S_{12} + \frac{1}{2} S_c [\sin(2q)]^2 & S_{11} - \frac{1}{2} S_c [\sin(2q)]^2 & S_{12} & 0 & 0 & \frac{1}{2} S_c [\sin(4q)] \\ S_{12} & S_{12} & S_{11} & 0 & 0 & 0 \\ 0 & 0 & 0 & S_{44} & 0 & 0 \\ 0 & 0 & 0 & 0 & S_{44} & 0 \\ -\frac{1}{2} S_c [\sin(4q)] & \frac{1}{2} S_c [\sin(4q)] & 0 & 0 & 0 & S_{44} + 2 S_c [\sin(2q)]^2 \end{bmatrix} \quad \text{-----(25)}$$

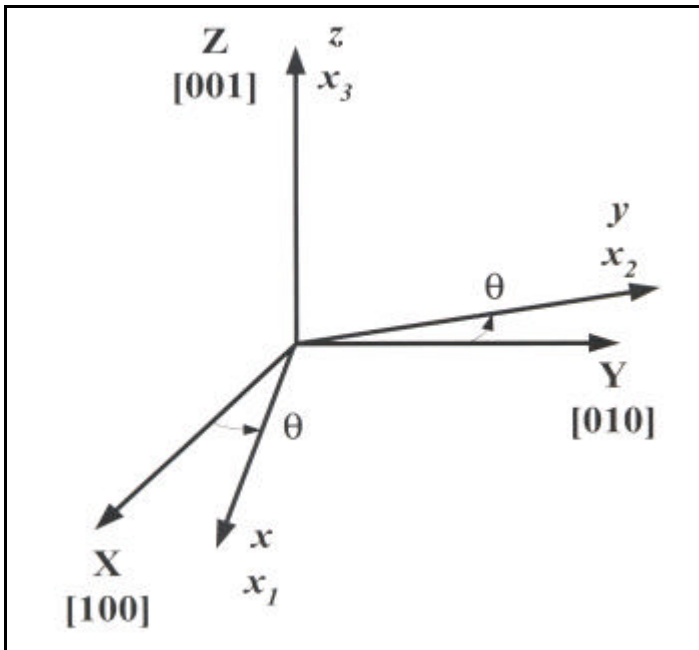


Fig 28: Diagram showing rotation in the [001] direction

(Note for this research, θ is taken to be 45°)

To substitute into the Ansys FEM software, some adjustments have to be made:

$$\begin{aligned}
 E_x = E_y &= \frac{1}{S_{11} - \frac{1}{2}S_C [\sin(2q)]^2}; E_z = \frac{1}{S_{11}} \\
 u_{xy} = u_{yx} &= \frac{S_{12} + \frac{1}{2}S_C [\sin(2q)]^2}{S_{11} - \frac{1}{2}S_C [\sin(2q)]^2} \\
 u_{xz} &= \frac{S_{12}}{S_{11} - \frac{1}{2}S_C [\sin(2q)]^2}; u_{zx} = \frac{S_{12}}{S_{11}} \\
 u_{yz} &= \frac{S_{12}}{S_{11} - \frac{1}{2}S_C [\sin(2q)]^2}; u_{zy} = \frac{S_{12}}{S_{11}} \\
 G_{yz} = G_{xz} &= \frac{1}{S_{44}}; G_{xy} = \frac{1}{S_{44} + 2S_C [\sin(2q)]^2}
 \end{aligned}
 \tag{26}$$

Note that:

$$\begin{aligned}
 \mathbf{n}_{xy} &= \mathbf{n}_{yx} \\
 \mathbf{n}_{xz} &\neq \mathbf{n}_{zx} \\
 \mathbf{n}_{yz} &\neq \mathbf{n}_{zy}
 \end{aligned}
 \tag{27}$$

$E_x, E_y, E_z, \mathbf{n}_{xy}, \mathbf{n}_{yz}, \mathbf{n}_{xz}$ were calculated using the above formula (refer to equation (26)) and then substituted into the material constant in the Ansys FEM model.

3.3.8 Limitations of FEM analysis

Although computational methods such as FEM analysis are very useful in fields like fracture mechanics, they cannot replace experiments. A numerical fracture simulation of a cracked body can compute crack tip parameters, but such an analysis alone cannot predict when fracture will occur. FEM analysis relies on continuum theory. A continuum does not contain voids, microcracks, second-phase particles, grain boundaries, dislocations, atoms, or any of the other microscopic or submicroscopic features that control fracture behavior in engineering materials.

A numerical analysis of a cracked body can provide information on local stresses and strains at the crack tip, as well as global fracture parameters. Existing analyses, however, model only the deformation of the material. Fracture can be modeled, but a separate fracture criterion is required. For example, one might model cleavage fracture by imposing a stress-based failure criterion, in which the analysis would predict failure when a user-specified stress is reached at a particular point ahead of the crack tip. Predictions of fracture could not be made a priori in such cases, but would require one or more experiments to infer material-dependent parameters in the local fracture model.

Several researchers have attempted to combine flow and fracture behavior into a single constitutive model, and have incorporated such approaches into finite element analyses. The Gurson model, for instance, was intended to model both plastic flow and ductile fracture in metals. Because this approach is a continuum model and does not include voids, however, it does not capture the important microscopic events that lead to fracture, and it is unable to predict failure in real materials. A number of adjustable parameters have recently been added to this model in order to bring predictions in line with experimental data, but such parameters are based on curve fitting rather than sound physics.

Numerical analysis will undoubtedly play a major role in developing micromechanical models for fracture. Computer simulation of processes such as microcrack nucleation, void growth, and interface fracture should lead to new insights into fracture and damage mechanisms. Such research may then lead to rational failure criteria that can be incorporated into global continuum models of cracked bodies.

Computer modeling cannot replace experimentation. Any mathematical model, regardless of how sophisticated it is, will omit much of the real world in its formulation. Unlike a mathematical model, an experiment is obliged to obey all laws of nature, down to the quantum level. Thus, an experiment often conveys important information that a simulation overlooks.

3.4 Bayesian reliability analysis

3.4.1 Introduction

Bayesian parameter estimation is a method often used to estimate parameter when there is insufficient data. A prior PDF (probability density function) is first assumed for the unknown parameter. Then, this prior PDF together with sample data are used to obtain the posterior PDF. Because there is much freedom in choosing the prior PDF, Bayesian reliability is often criticized as being subjective. The general formula for Bayesian analysis is shown below in equation (28):

$$f_1(\mathbf{q}) = f(\mathbf{q} | A) = \frac{P(A | \mathbf{q})f_0(\mathbf{q})}{\int P(A | \mathbf{q})f_0(\mathbf{q}) d\mathbf{q}} \quad \text{-----(28)}$$

$f_0(\mathbf{q})$: Prior PDF

$f_1(\mathbf{q})$ Or $f(\mathbf{q} | A)$: posterior PDF (PDF given that event A has occurred)

$P(A | \mathbf{q})$: Probability of event A given a certain value of parameter

\mathbf{q} : Unknown parameter to be estimated

For example, assuming that $P(A | \mathbf{q}) = \prod_{i=1}^n \{g(x_i | \mathbf{q})\}$ whereby $g(x | \mathbf{q})$ is the PDF of a variable x (for instance, fatigue life) and x_i is the sample data for the variable x. Then, the posterior PDF can be written as shown below in equation (29):

$$f_1(\mathbf{q}) = \frac{\left(\prod_{i=1}^n g(x_i | \mathbf{q}) \right) f_0(\mathbf{q})}{\int \left(\prod_{i=1}^n g(x_i | \mathbf{q}) \right) f_0(\mathbf{q}) d\mathbf{q}} \quad \text{-----(29)}$$

A Bayesian analysis combines prior information about model parameters with information from observed data, thereby generating a posterior distribution. Such an analysis requires two inputs, namely the prior distribution and the likelihood function. The prior distribution can be chosen to represent the beliefs of the researcher before observing the results of an experiment; this results in a subjective Bayesian analysis. Often, however, it is difficult for a researcher to specify prior beliefs about model parameters, and to cast them into the form of a prior probability distribution.

Thus, one problem with Bayesian reliability analysis is what prior PDF to assume. Very often, **conjugate prior** is used because of simpler mathematical computation. A noteworthy point is that conjugate PDF is assumed only to simplify the mathematical computation and if some other forms of prior PDF are more appropriate, such prior PDF should be used instead.

3.4.2 Non-informative prior¹²

In Bayesian statistics, the choice of the prior distribution is often controversial. In the absence of strong prior evidence or opinion, it is intuitively instructive to assume a “**non-informative prior**” for the prior PDF. A noninformative prior is a function, which is used in place of a subjective prior distribution when little or no prior information is available. The term “noninformative” is used to connote the lack of subjective beliefs used in formulating such a prior. Intuitively speaking, a prior distribution is non-informative if the prior is “flat” relative to the maximum likelihood function and if it has minimal impact on the posterior PDF of the unknown parameter. A noteworthy point is that a non-informative prior is not always the same thing as a flat uniform distribution.

An important property to be satisfied by a noninformative prior is the **local uniformity property**: the prior does not change very much over the region in which the likelihood is appreciable and does not assume large values outside that range. **Jeffrey’s prior** is a prior that satisfies this property and is based on the Fisher information matrix. Furthermore, it is invariant to transformation of the parameter vector. This is the most important property of the Jeffrey’s prior.

The fisher information matrix is defined as shown below in equation (30):

$$I(\mathbf{q}) = -E \left[\frac{\partial^2 \log p(x|\mathbf{q})}{\partial q_i \partial q_j} \right]_{p \times p} \quad \text{-----(30)}$$

whereby θ is a $(p \times 1)$ vector and $I(\mathbf{q})$ is a $(p \times p)$ matrix. (x : variable; θ : parameter).

Jeffrey’s prior is defined as shown in equation (31) below:

$$p(\mathbf{q}) \propto |I(\mathbf{q})|^{-\frac{1}{2}} \quad \text{-----(31)}$$

In spite of its success in one-parameter problems, the Jeffrey’s prior is often seriously deficient in multi-parameter problems. To overcome the deficiencies of using the Jeffrey’s prior, reference prior approach has been developed. The reference prior method introduced by Bernardo (1979) and further described by Berger and Bernardo (1992), was motivated by the notion of maximizing the expected amount of information about θ provided by the data, x . The amount of information provided by the experiment is quantified by the Kullback-Liebler divergence, which is defined by equation (32):

$$D(p(\mathbf{q}|x), p(\mathbf{q})) = \int_y p(\mathbf{q}|x) \log \left(\frac{p(\mathbf{q}|x)}{p(\mathbf{q})} \right) d\mathbf{q} \quad \text{-----(32)}$$

A prior that maximizes the expected value of the Kullback-Liebler divergence is then formulated as shown below in equation (33):

$$E[D(\mathbf{p}(\mathbf{q} | x), \mathbf{p}(\mathbf{q}))] \text{ -----(33)}$$

The posterior PDF of Weibull modulus and scale parameter based on the reference prior approach are given below in equations (34) and (35):

$$\mathbf{p}(\mathbf{q} | X_n) = \frac{\int_0^\infty \left\{ \frac{\mathbf{b}^{n-1}}{\mathbf{q}^{nb+1}} \prod_{i=1}^n X_i^{\mathbf{b}} \exp\left(\frac{-\sum_{j=1}^n X_j^{\mathbf{b}}}{\mathbf{q}^{\mathbf{b}}}\right) \right\} d\mathbf{b}}{\Gamma(n) \int_0^\infty \left\{ s^{n-2} \prod_{i=1}^n X_i^s (\sum_{j=1}^n X_j^s)^{-n} \right\} ds} \text{ -----(34)}$$

$$\mathbf{p}(\mathbf{b} | X_n) = \frac{\mathbf{b}^{n-2} (\prod_{i=1}^n X_i)^{\mathbf{b}} (\sum_{j=1}^n X_j^{\mathbf{b}})^{-n}}{\int_0^\infty \left\{ s^{n-2} (\prod_{i=1}^n X_i)^s (\sum_{j=1}^n X_j^s)^{-n} \right\} ds} \text{ -----(35)}$$

$X_n = \{X_1, X_2, \dots, X_n\}$: Data

$\Gamma(x) = \int_0^\infty t^{x-1} e^{-t} dt, x > 0$: Gamma function

\mathbf{q} : Scale parameter

\mathbf{b} : Weibull modulus

3.4.3 Effectiveness of the Bayesian method with respect to the MLM (maximum likelihood method)

The effectiveness of the Bayesian method with respect to the maximum likelihood method is compared and the results are shown in Table 1 and Table 2. [Note: The underlying parameter values are 700 for the scale parameter and 10 for the Weibull modulus.] In the absence of sufficient data (less than 10 samples), the Weibull modulus was more efficiently estimated by the Bayesian method. In the case of the scale parameter, no noticeable difference could be observed.

Table 1: Comparison between Bayesian and MLM (absolute value)

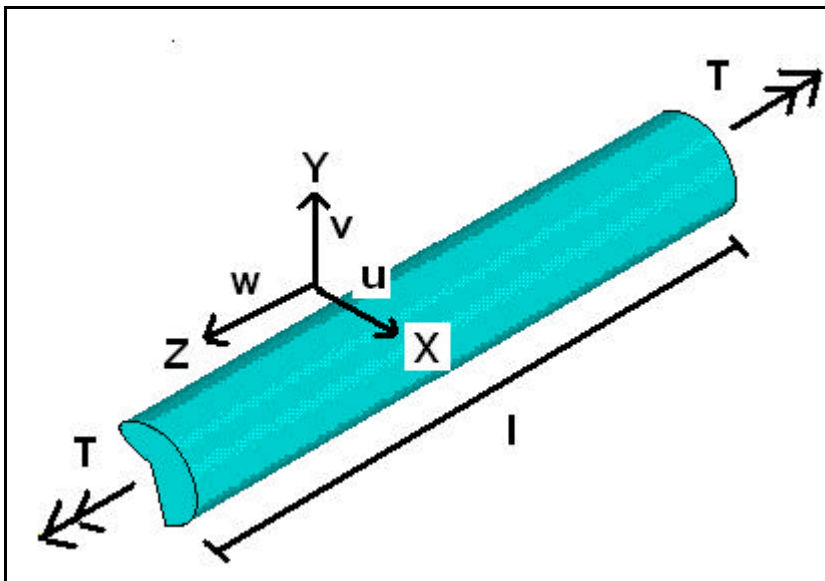
No of data	Scale parameter		Weibull modulus	
	Bayesian	MLM	Bayesian	MLM
2	680	669	NA	23.7
4	660	657	13.9	20.9
6	680	686	12.5	15.8
8	740	728	9.3	10.9
10	720	728	10.5	11.9
15	720	712	10	10.9
20	700	696	8.6	9.15
25	700	701	9.7	10.2

Table 2: Comparison between Bayesian and MLM (%value)

No of data	Scale parameter		Weibull modulus	
	Bayesian	MLM	Bayesian	MLM
4	94.3	93.9	139.0	209.0
6	97.1	98.0	125.0	158.0
8	105.7	104.0	93.0	109.0
10	102.9	104.0	105.0	119.0
15	102.9	101.7	100.0	109.0
20	100.0	99.4	86.0	91.5
25	100.0	100.1	97.0	102.0

When there is a need to obtain information regarding parameters from few experiment data, the Bayesian method is effective. Posterior PDF obtained from an actual prior subjective opinion can then be compared with those derived from a non-informative prior so as to assess the relative importance of the initial opinions on the final inference.

3.5 St. Venant torsion theory



$X, Y,$ and Z :
directions

u, v, w :
displacement
direction

l : length of
prismatic beam

T : end torques
applied to beam

Fig 29: Representation of general long prismatic rod (note: length $l \gg$ dimensions in the X and Y directions)

The classical torsion theory considers a long prismatic rod (Fig 29) whereby the length dimension is much greater than the cross-sectional dimensions. Furthermore, it does not consider how the end torque is applied. This is related to the Saint-Venant's principle.

Important geometrical assumptions made in the classical torsion theory:

- Each cross-section rotates as a rigid body (no distortion of the cross-section shape in the x and y direction)
- Rate of twist, k is constant
- Cross-sections are free to warp in the z-direction but the warping is the same for all cross-sections. (Warping: extensional deformation in the direction of the axis about which the torque is applied.)

Problems of applying the classical torsion theory to actual problems:

- In reality, the member under the influence of force will have to be constrained in certain ways and the method of application of the end torque will have significant influences on the stress distribution in the beam.
- Prediction of the stress distribution near the end constraint will highly depend on the member geometry at the end constraint and FEM analysis should be used.
- Moreover, the length dimension of the prismatic bar has to be sufficiently long compared to the cross-sectional dimensions. However,

how long the length dimension should be is not specified explicitly in the classical torsion theory.

- In addition, beam section of the test specimen is not prismatic due to the presence of the “R” at the end of the beam designed to avoid stress concentrations.

At distance away from the end constraint (stress distribution at the center of the beam), stress distribution of the member subjected to torsional loading can still be predicted by the classical torsion theory.

3.6 Saint-Venant’s principle

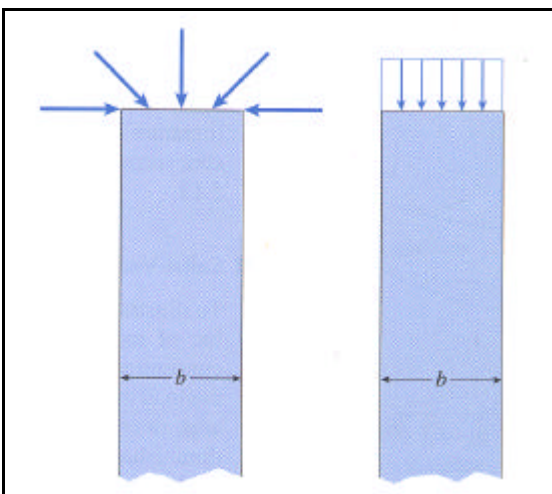


Fig 30: Saint-Venant’s principle

With rare exceptions, this principle applies to linearly elastic bodies of all types. To understand Saint-Venant’s principle, imagine that we have a body with a system of loads acting over a small part of its surface. For instance, suppose we have a prismatic bar of width b subjected to a system of several concentrated loads acting at the end. (Refer to Fig 30) For simplicity, assume that the loads are symmetrical and have a vertical resultant. Next, consider a different but statically equivalent load system acting over the same small region of the bar. “Statically equivalent” means that the two load systems have the same force resultant and same moment resultant. Saint-Venant’s principle states that the stresses in the body caused by either of the two systems of loading are the same, provided we move away from the loaded region a distance at least equal to the largest dimension of the loaded region. This principle is not a rigorous law of mechanics but is a common-sense observation based upon theoretical and practical experience.

Saint-Venant's principle has great practical significance in the design and analysis of structures encountered in the mechanics of materials. Because the effects of stress concentrations are localized and have little effect on the overall behavior of a member, we can use all of the standard stress formulas at cross sections a

sufficient distance away from the source of the concentration. Close to the source, the stresses depend upon the details of the loading and the shape of the member.

3.7 Safety design in the context of reliability engineering

3.7.1 Introduction to Crystal Ball

Crystal Ball is an easy-to-use simulation program that helps you to analyze the risks and uncertainties associated with your Excel spreadsheet models. The first step to using Crystal Ball is to determine which model inputs are uncertain. Once you have identified these, you use your knowledge of the uncertainty around the input to create a PDF for that cell (what we call an assumption). The next step is to identify a forecast. A forecast is a formula cell that you want to measure and analyze. You can define multiple assumptions and forecasts. Once finished, you use the Crystal Ball command or toolbar icon to run a simulation. Simulation results are displayed in interactive histograms, or frequency charts.

The Developer Kit for Crystal Ball describes many functions that can enhance the modeling experience. One of the most useful functions is `CB.GetForeStatFN`. `CB.GetForeStatFN` calculates a specified statistic for the specified forecast and places it in the cell calling the function. The statistics can be fed back to the assumption parameters to create a dynamic simulation.

OptQuest is an optimization tool that enhances simulation models by automatically searching for and finding optimal solutions. OptQuest surpasses the limitations of genetic algorithm optimizers because it uses multiple, complimentary search methodologies, including advanced tabu search and scatter search, to help find the best global solutions. While running solutions, OptQuest also checks for compliance with the constraints and requirements. In addition, OptQuest applies adaptive and neural network technologies to help it learn from past optimizations so it can achieve better results in less time.

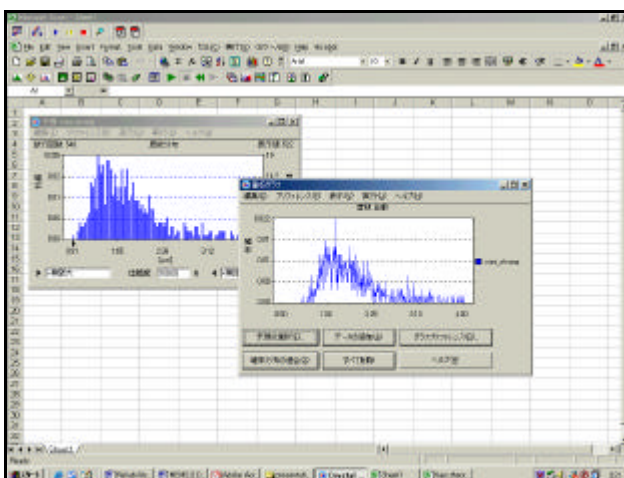


Fig 31: Reliability analysis using crystal ball

3.7.2 Monte Carlo simulation and importance sampling simulations

The probability of failure for the general case is given by the expression below in equation (36):

$$P_{failure} = \int \dots \int_{g(X_1, X_2, \dots) < 0} f(X_1, X_2, \dots) dx \quad \text{-----(36)}$$

$f(X_1, X_2, \dots)$ is the design joint PDF and $g(X_1, X_2, \dots)$ is the limit state function. Usually, $f(X_1, X_2, \dots)$ is a complicated function and the expression of probability of failure in a closed form is difficult. Thus, Monte Carlo simulation is often employed. The probability of failure can be expressed explicitly in a cell in the Excel sheet using the crystal ball function. When one uses Monte Carlo simulation to find the occurrence probability of a rare event, it is necessary to run much iteration to get a good approximation. To obtain a good approximation in a smaller number of iterations, it is advisable to use the importance sampling method.

Monte Carlo method is shown below in equation (37):

$$\begin{aligned} \Pr(x > c) &= \int_{-\infty}^{\infty} I_{MC}(x) f(x) dx \\ I_{MC}(x) &= 1 \quad (x > c) \\ I_{MC}(x) &= 0 \quad (x \leq c) \end{aligned} \quad \text{-----(37)}$$

Importance sampling method is shown below in equation (38):

$$\begin{aligned} \Pr(x > c) &= \int_{-\infty}^{\infty} I_{IS}(x) g(x) dx, \quad g(x) : \int_{-\infty}^{\infty} g(x) dx = 1 \\ I_{IS}(x) &= \frac{f(x)}{g(x)} \quad (x > c) \\ I_{IS}(x) &= 0 \quad (x \leq c) \end{aligned} \quad \text{-----(38)}$$

Both the Monte Carlo method and the importance sampling method can be easily implemented to find the probability of failure using the Crystal Ball and Excel functions. There is no fixed rule for the choice of the function $g(x)$ (weight function). However, it is advisable to initially run the simulation using the Monte Carlo method for a small number of iterations. Then choose the appropriate parameters for $g(x)$ by observing the PDF initially generated.

3.7.3 Proof test of brittle material

Proof test is often used as a means to screen off defective products or products with strength less than that stipulated in the proof test. The PDF after the proof test should be adjusted upwards or else the initial probability of failure will be underestimated. An importance assumption here is that during the proof test process, the strength of the product remains static and hence unchanged. However, in reality, cracks inherent in the product may propagate during the proof test. It has been shown theoretically that samples that pass the proof test have strengths less than the proof test level. But this is a small probability event. To account for this, probability of failure associated with the screening stress should be adjusted upwards accordingly based on the characteristics of the proof test such as loading rate, dwell time and unloading rate. If there are uncertainties involving the proof test level, they can be modelled by a 2nd order random variable.

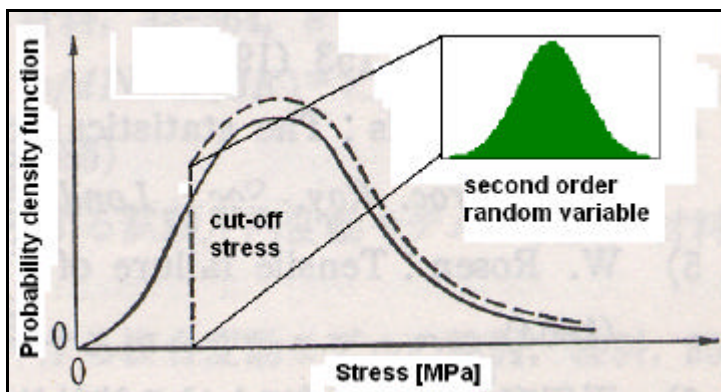


Fig. 32: PDF of product strength before and after proof test, and setting of the 2nd order random variable for the cut-off stress (proof test level)

It should be noted that proof test be performed on the final form of the product.

3.7.4 Dynamic simulation

The concept of time can be introduced in a number of ways. In crystal ball, the passage of time can be monitored by means of the number of iterations. However, the relationship between the simulation time unit and the actual real time unit has to be determined. For instance, both the strength and stress can be modeled using normal PDF. As time passes by (number of iterations increase), the mean of the strength distribution decreases linearly. On the other hand, the mean of the stress distribution is assumed constant. As the mean of the strength distribution decreases, the failure probability increases until it stabilizes at a certain value. The fact that the simulation results can be extracted using the Crystal Ball functions enables one to modify the input pdf based on the output results to create a dynamic simulation.

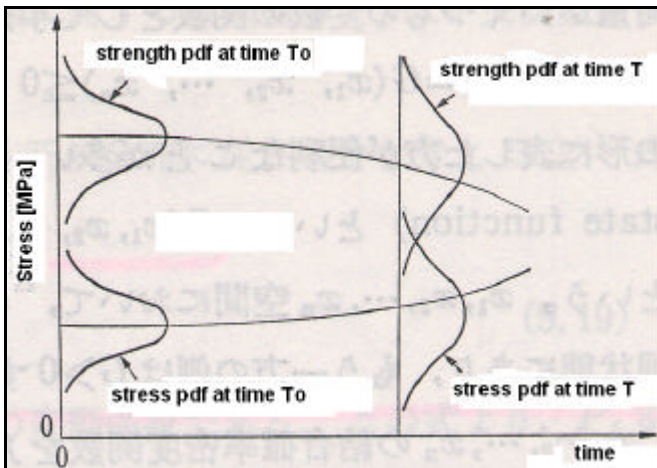


Fig 33: An example of a dynamic simulation in which the stress and strength PDF parameters (mean and standard deviation) change over time

3.7.5 Probabilistic design

Probabilistic Design is a technique you can use to assess the effect of uncertain input parameters and assumptions on your analysis model. Probabilistic design can be used to determine the effect of one or more variables on the outcome of the analysis.

Using a probabilistic analysis you can find out how much the results of a finite element analysis are affected by uncertainties in the model. An uncertainty or random quantity is a parameter where it is impossible to tell the exact value at a given point in time (if it is time dependent) or at a given location (if it is location dependent). One example of this is ambient temperature, where you never know exactly what the temperature will be one week from now in a certain city. In a probabilistic analysis these uncertain parameters are described by statistical distribution functions such as the Gaussian or normal distribution, the uniform distribution, etc.

Computer models are expressed and described with specific numerical and deterministic values; material properties are entered using certain values, the geometry of the component is assigned a certain length or width, etc. An analysis based on a given set of specific numbers and values is called a *deterministic analysis*. Naturally, the results of a deterministic analysis are only as good as the assumptions and input values used for the analysis. The validity of those results depends on how correct the values were for the component under real life conditions.

In reality, literally every aspect of an analysis model is subjected to scatter (in other words, is uncertain in some way). Material property values are different if one specimen is compared to the next. This kind of scatter is inherent for materials and varies among different material types and material properties. For example, the scatter of the Young's modulus for many materials can often be described as a Gaussian distribution with standard deviation of $\pm 3 - 5\%$. Likewise, the geometric properties of components can only be reproduced within certain manufacturing

tolerances. The same variation holds true for the loads that are applied to a finite element model. However, in this case the uncertainty is often due to a lack of engineering knowledge. For example, at elevated temperatures the heat transfer coefficients are very important in a thermal analysis, yet it is almost impossible to measure the heat transfer coefficients. This means that almost all input parameters used in a finite element analysis are inexact, each associated with some degree of uncertainty.

It is neither physically possible nor financially acceptable to eliminate the scatter of input parameters completely. The reduction of scatter is typically associated with higher costs either through better and more precise manufacturing methods and processes or increased efforts in quality control. Hence, accepting the existence of scatter and dealing with it rather than trying to eliminate it makes products more affordable and production of those products more cost effective. If the input variables of a finite element model are subjected to scatter, how large is the scatter of the output parameters? How robust are the output parameters? Examples are the temperature, stress, strain, or deflection at a node, the maximum temperature, stress, strain, or deflection of the model, etc. If the output is subjected to scatter due to the variation of the input variables, then what is the probability that a design criterion given for the output parameters is no longer met? How large is the probability that an unexpected and unwanted event takes place (what is the failure probability)? Which input variables contribute the most to the scatter of an output parameter and to the failure probability? What are the sensitivities of the output parameter with respect to the input variables?

3.7.6 Traditional (deterministic) vs. probabilistic design analysis methods

In traditional deterministic analyses, uncertainties are either ignored or accounted for by applying conservative assumptions. Uncertainties are typically ignored if the analyst knows for certain that the input parameter has no effect on the behavior of the component under investigation. In this case, only the mean values or some nominal values are used in the analysis. However, in some situations the influence of uncertainties exists but is still neglected; for example, the Young's modulus mentioned above or the thermal expansion coefficient, for which the scatter is usually ignored. Let's assume you are performing a thermal analysis and you want to evaluate the thermal stresses (thermal stresses are directly proportional to the Young's modulus as well as to the thermal expansion coefficient of the material). The equation is:

$$\boxed{s_{therm} = Ea\Delta T} \quad \text{-----(39)}$$

If the Young's modulus alone has a Gaussian distribution with a 5% standard deviation, then there is almost a 16% chance that the stresses are more than 5% higher than what you would think they are in a deterministic case. This figure

increases if you also take into account that, typically, the thermal expansion coefficient also follows a Gaussian distribution.

Table 3: Differences in results between deterministic and probabilistic design

Random Input Variables taken into account	Probability that the thermal stresses are more than 5% higher than expected	Probability that the thermal stresses are more than 10% higher than expected
Young's modulus (Gaussian distribution with 5% standard deviation)	~16%	~2.3%
Young's modulus and thermal expansion coefficient (each with Gaussian distribution with 5% standard deviation)	~22%	~8%

When a conservative assumption is used, this actually tells you that uncertainty or randomness is involved. Conservative assumptions are usually expressed in terms of safety factors. Sometimes regulatory bodies demand safety factors in certain procedural codes. If you are not faced with such restrictions or demands, then using conservative assumptions and safety factors can lead to inefficient and costly over-design. **You can avoid over-design by using probabilistic methods while still ensuring the safety of the component.**

Probabilistic methods even enable you to quantify the safety of the component by providing a probability that the component will survive operating conditions. Quantifying a goal is the necessary first step toward achieving it. Probabilistic methods can tell you how to achieve your goal.

3.7.7 Surface response method

Surface response method is a modern technique for sequentially optimizing process parameters to optimize process response. For instance, determine the level of temperature X_1 and pressure X_2 that maximizes the yield Y of a process. If data follows a flat surface, a first order model (equation (40)) is usually sufficient:

$$y = \mathbf{b}_0 + \mathbf{b}_1 X_1 + \mathbf{b}_2 X_2 + \dots + \mathbf{b}_k X_k \quad \text{-----(40)}$$

If there is curvature in the data, a first order model would show a significant lack of fit, and a higher order model (equation (41)) must be used to “mold” to the curvature:

$$y = b_0 + \sum_{i=1}^k b_i X_i + \sum_{i=1}^k b_{ii} X_i^2 + \dots + \sum_{i=1}^k \sum_{\substack{j=1 \\ i < j}}^k b_{ij} X_i X_j + e \quad \text{-----(41)}$$

In industries, experiments are conducted to discover which values of given factor variables optimize a response. If each factor is measured at three or more values, a quadratic response surface can be estimated by least-squares regression. The predicted optimal value can be found from the estimated surface if the surface is shaped like a simple hill or a valley. If the estimated surface is more complicated, or if the predicted optimum is far from the region of experimentation, then the shape of the surface can be analyzed to indicate the directions in which new experiments should be performed.

Suppose that a response variable y is measured at combinations of values of two factor variables, x_1 and x_2 . The quadratic response-surface model for this variable is written as shown in equation (42):

$$y = b_0 + b_1 x_1 + b_2 x_2 + b_3 x_1^2 + b_4 x_2^2 + b_5 x_1 x_2 + e \quad \text{-----(42)}$$

The steps in the analysis for such data are

- Model fitting and analysis of variance to estimate parameters
- Canonical analysis to investigate the shape of the predicted response surface
- Ridge analysis to search for the region of optimum response

The first task in analyzing the response surface is to estimate the parameters of the model by least-squares regression and to obtain information about the fit in the form of an analysis of variance. The estimated surface is typically curved: a "hill" whose peak occurs at the unique estimated point of maximum response, a "valley," or a "saddle-surface" with no unique minimum or maximum. Use the results of this phase of the analysis to answer the following questions:

- What is the contribution of each type of effect -linear, quadratic, and crossproduct -to the statistical fit? The ANOVA table with sources labeled "Regression" addresses this question.
- What part of the residual error is due to lack of fit? Does the quadratic response model adequately represent the true response surface?
- What is the contribution of each factor variable to the statistical fit? Can the response be predicted as well if the variable is removed?
- What are the predicted responses for a grid of factor values?

The second task in analyzing the response surface is to examine the overall shape of the curve and determine whether the estimated stationary point is a maximum, a minimum, or a saddle point. The canonical analysis can be used to answer the following questions:

- Is the surface shaped like a hill, a valley, a saddle surface, or a flat surface?

- If there is a unique optimum combination of factor values, where is it?
- To which factor or factors are the predicted responses most sensitive?

The eigenvalues and eigenvectors in the matrix of second-order parameters characterize the shape of the response surface. The eigenvectors point in the directions of principle orientation for the surface, and the signs and magnitudes of the associated eigenvalues give the shape of the surface in these directions. Positive eigenvalues indicate directions of upward curvature, and negative eigenvalues indicate directions of downward curvature. The larger an eigenvalue is in absolute value, the more pronounced is the curvature of the response surface in the associated direction. Often, all of the coefficients of an eigenvector except for one are relatively small, indicating that the vector points roughly along the axis associated with the factor corresponding to the single large coefficient. In this case, the canonical analysis can be used to determine the relative sensitivity of the predicted response surface to variations in that factor.

If the estimated surface is found to have a simple optimum well within the range of experimentation, the analysis performed by the preceding two steps may be sufficient. In more complicated situations, further search for the region of optimum response is required. The method of ridge analysis computes the estimated ridge of optimum response for increasing radii from the center of the original design. The ridge analysis answers the following question: If there is not a unique optimum of the response surface within the range of experimentation, in which direction should further searching be done in order to locate the optimum?

In this research, the relationship between the design stress (output: dependent variable) and the displacement (input: independent) is to be determined. Since there is only one independent variable, a simple regression analysis is all that is needed to obtain the relationship between the design stress and displacement.

4 Design of test specimen

4.1 Overview

Since it is almost impossible to perform a pure torsional test experimentally, the **stress ratio** (to be defined later in the discussion) will be maximized, and combined loading will be performed and the effect of pure torsional loading extrapolated based on the **load factor analysis** (refer to Theory). Pure bending test is first accomplished by depressing the specimen at location **A** (Refer to Fig 34), and then combined loading test by depressing the specimen at location **B**. The effect of self-weight could be neglected based on FEM analysis. Two main factors have to be considered when designing a specimen for micro testing: experimental and mechanical considerations.

4.2 Experimental considerations

The load cell has a maximum capacity of 5N (note: now 1N and 2.5N load cells are available) and the applied load can be measured to within $\pm 1\%$ of its value. The range of the LDM (laser displacement meter) about 600 μm and its accuracy is 0.5 μm . Here, the slowest testing speed of 0.5mm/min is used in order to get the maximum number of sampling results. Next, the rotational angle cannot be too large or slippage of the loading needle may occur. Moreover, if the rotation angle is too large, curvature shortening may lead to unwanted tensile forces acting on the beams. The maximum rotational angle is preferably taken to be 30° . In the design process, the center deflection is taken to be in the order of 100 μm and the edge deflection in the order of 1mm.

4.3 Mechanical considerations

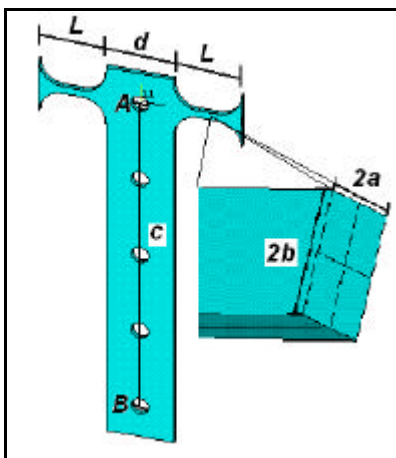


Fig. 34: Representation of the beam

$2a$: Height of beam
 $2b$: Width of beam
 c : Length of plate
 d : Width of plate
 L : Length of beam
 q : Rotational angle
 G : Shear modulus

A: Midpoint of plate
B: Edge of plate (at a distance of c from **A**)

It has to be ensured that the specimen fails under torsional loading. The shear stress due to torsion can be expressed as a function of a , b , θ , L and G . (Refer to Fig. 34) The normal stress due to flexure can be expressed as a function of a , b , c , d , θ , L and G . When the ratio of the shear stress to the normal stress is taken, θ and G are being cancelled out. Thus, the **stress ratio** (ratio of maximum shear stress to maximum normal stress, irrespective of location in the beam) depends on a , b , c , d and L .

4.4 Stress ratio

The stress ratio is defined as ratio of maximum shear stress to maximum normal stress, irrespective of location in the beam. It can be considered a measure of the intensity of shear stress in the beam with respect to the normal stress. At the time of design of test specimen, the flaw population (distribution and orientation) is still unclear. Hence, the stress ratio is considered irrespective of the location in the beam. The stress ratio is defined below as shown in equation (43):

$$\text{stress ratio} = \frac{t_{\max}}{s_{\max}} \quad \text{-----(43)}$$

$$\text{stress ratio} \propto \text{function}(a, b, c, d, L) \quad \text{-----(44)}$$

It can be shown that stress ratio is a function of a , b , c , d and L . (equation (44))

4.5 Maximum shear stress calculation

Maximum fictitious shear stress, t_F , due to torsion alone (equation (45):

$$t_F = \frac{3T_F}{8ba^2} \left[1 + 0.6095 \left(\frac{a}{b} \right) + 0.8865 \left(\frac{a}{b} \right)^2 - 1.8023 \left(\frac{a}{b} \right)^3 + 0.9100 \left(\frac{a}{b} \right)^4 \right] \quad (45)$$

at the midpoint of each longer side for $b \geq a$.

Shear stress due to transverse stress, t_T (equation (46):

$$t_T = \frac{F/2}{A} = \frac{F}{8ab} \quad (46)$$

Total maximum shear stress, t_{\max} (equation (47):

$$t_{\max} = t_T + t_F \quad (47)$$

If the transverse shear, t_T , is negligible compared to the fictitious shear stress, t_F , the maximum shear stress can be expressed in the following form (equation (48):

$$t_{\max} \approx \frac{Gq f_1(a,b)}{L} \quad (48)$$

whereby $f_1(a,b)$ is a function of dimension a and b .

4.6 Maximum normal tensile stress calculation

Due to warping, the longitudinal fibers are stretched, and the longitudinal stretch generates a **warping tensile stress**, s_{warp} proportional to t_F^2 is given by equation (49):

$$s_{warp} = \frac{Et_F^2}{12G^2} \left(\frac{b}{a}\right)^2 \quad \text{-----(49)}$$

Flexural stress due to bending, s_{flex} is given by equation (50):

$$s_{flex} = \pm \frac{3.M}{4a^2b} \quad \text{-----(50)}$$

whereby moment, M , at the edge of the beam (since the beams are constrained, maximum flexure stress will occur at the edge of the beam) is given by equation (51):

$$M = \frac{F(2L+d)}{8} = \frac{(2L+d)kGq}{4Lc} \quad \text{-----(51)}$$

Total maximum normal tensile stress, s_{max} is given by equation (52):

$$s_{max} = s_{warp} + s_{flex} \quad \text{-----(52)}$$

If the warping tensile stress is negligible compared to the flexural stress, the maximum normal tensile stress can be expressed as shown in equation (53):

$$s_{max} \approx \frac{Gq f_2(a,b,L,d)}{c} \quad \text{-----(53)}$$

whereby $f_2(a,b,L,d)$ is a function of dimension a and b .

4.7 Torque calculation

Geometric factor, k , is given by equation (54):

$$k = ba^3 \left[\frac{16}{3} - 3.36 \frac{a}{b} \left(1 - \frac{a^4}{12b^4} \right) \right] \quad \text{-----(54)}$$

(Refer to Fig 34; note that $b \geq a$)

This geometric factor, k , can be used to calculate the **fictitious torque** T_F induced by the applied rotation, θ , and generated by shear stress alone. The fictitious torque, due to torsion alone and neglecting the additional torque due to the end constraints is given by equation (55):

$$T_F = KG \frac{q}{L} \quad \text{-----(55)}$$

Fiber elongation torque, T_E , is given by equation (56):

$$T_E = \frac{8}{45} E \left(\frac{q}{L} \right)^3 ab^5 \quad \text{-----(56)}$$

The **actual reaction torque**, T_A , is given by equation (57):

$$T_A = 2(T_F + T_E) \quad \text{(Due to symmetry) \quad \text{-----(57)}}$$

4.8 Points to be noted in the design process

The normal and shear stresses are calculated based on the linear elasticity theories. In reality, the test specimen may undergo large displacement and geometric nonlinearity will have to be considered. Moreover, in the design process, the test specimen is assumed prismatic. In reality, the test specimen is non-prismatic and has fillets at its edges to prevent stress concentration. Besides, in the design process, it is assumed that the material is isotropic. However, in reality, silicon is anisotropic and material properties will vary with directions. In view of these problems encountered in the design process, it is advisable to employ FEM analysis in the design process. However, detailed FEM modeling and analysis will require much computational time and as such in time-constrained circumstances, only simple theories will be used in the design process.

4.9 Excel sheet calculation

	A	B	C	D	E	F	G	H	I	J	K
1	rotation (rad)	E (N/mm ²)	poisson	G (N/mm ²)	a (mm)						
2	0.27925269	150000	0.3	57692.30769	7.50E-02						
3	1a										
4				b (mm)	L (mm)	2a					
5	Fin. Torque (Nmm)	k (mm ⁴)									
6	1.87E+00	2.02E-04									
7	finis elon. Torque (Nmm)										
8	4.13E-04										
9				shear stress (MPa)							
10	total torque (Nmm)			normal stress (MPa)							
11	8.73E+00			force (N)							
12				% force							
13	finic max shear stress (MPa)			centre deflection (um)							
14	1.12E+03			edge deflection (mm)							
15	transverse shear stress (MPa)	force QD	plate length c	stress ratio							
16	4.15E+00	3.73E-01	10								
17											
18	total shear stress (MPa)	% torsional shear stress									
19	1.13E+03	0.00E+01									
20	tensile stress (warp) (MPa)	% tensile stress (warp)									
21	1.375468183	0.549455008									
22											
23	stress (flexure) (MPa)	moment (Nmm)	I (mm ⁴)	whole length (mm)	width of plate d						
24	248.0564840	0.280076046	0.000084376	5	2						
25											

Fig 35: Excel sheet employed in the design process

The excel sheet is a useful tool that can be used in the design process. Some of the commonly used excel functions are “Table” and “Solver”.

Table function: A data table is a range of cells that shows how changing certain values in your formula affects the results of the formulas. Data tables provide a shortcut for calculating multiple versions in one operation and a way to view and compare the results of all of the different variations together on your worksheet.

Solver function: You can also determine resulting values when you need to change more than one cell used in a formula and have multiple constraints for those values. Solver adjusts the values in the cells you specify to produce the result you want from the formula. Moreover, one can use the solver function to perform simple linear and nonlinear optimization calculations.

Table 4: A typical Excel sheet calculation (for the case of 240um beam rotated through an angle of 15°)

Shear stress [MPa]	987.44
Normal stress [MPa]	207.75
Force [N]	0.25
% Force	4.99
Center deflection [um]	27.70
Edge deflection [mm]	2.62
Stress ratio	4.75

Table 5: A typical Excel sheet calculation using the Table Function showing the stress ratio for various a and b combinations (a: column ; b: row)

	0.05	0.06	0.07	0.08	0.09	0.10	0.11	0.12
0.05	5.35	5.06	4.89	4.75	4.63	4.53	4.43	4.35
0.06	5.94	5.35	5.10	4.94	4.82	4.71	4.61	4.53
0.07	7.14	5.81	5.35	5.13	4.98	4.87	4.77	4.68
0.08	9.42	6.64	5.72	5.35	5.15	5.02	4.91	4.82
0.09	13.37	8.11	6.35	5.66	5.35	5.17	5.04	4.94
0.10	19.69	10.52	7.38	6.16	5.62	5.35	5.18	5.06
0.11	29.19	14.24	9.01	6.94	6.03	5.59	5.35	5.19
0.12	42.82	19.69	11.43	8.11	6.64	5.94	5.56	5.35

4.10 Final dimensions of beams

The final dimensions of the beam are as follow:

$2a=150\mu\text{m}$;

$2b=240$ and $300\mu\text{m}$;

$c=10\text{mm}$;

$d=2\text{mm}$

$L=2\text{mm}$.

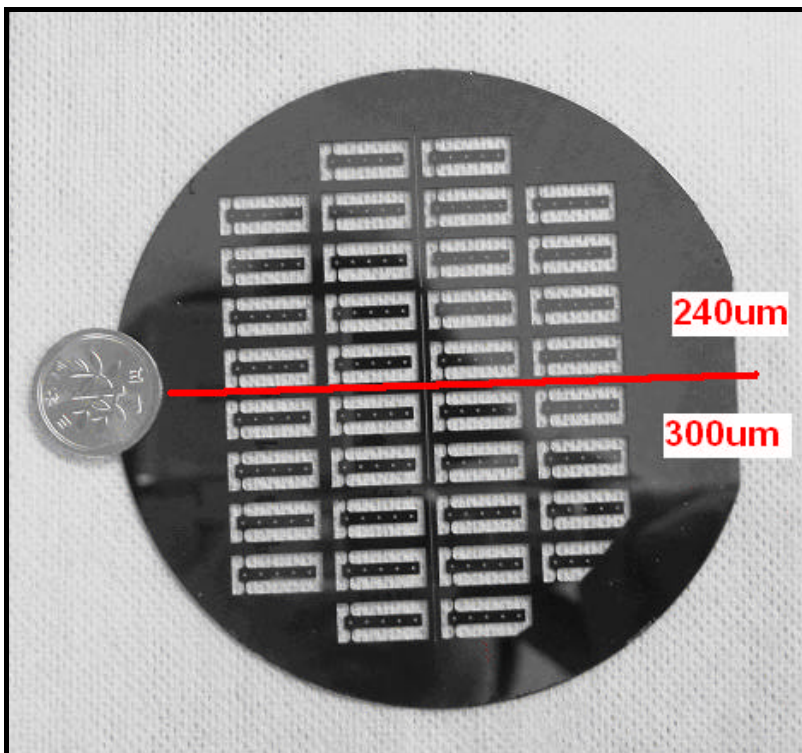


Fig 36: Test specimens on wafer (note: 36 test specimens on one wafer, 18 specimens of each type)

5 Experimental apparatus and procedures

5.1 Experimental setup

5.1.1 Introduction

In this research, (refer to Fig 37 and Fig 38) a 5N load cell was used and the needle moved downwards at a speed of 0.5mm/min towards the sample on the wafer and depressed it downward. The wafer is placed on a wafer holder. The downward displacement of the sample is measured by the LDM (laser displacement meter) placed underneath the wafer. The CCD camera is used for observing the site of depression to ensure that the needle fits into the hole in the sample. The force (load cell) and displacement (LDM and EZTest displacement) until the point of fracture are recorded simultaneously by a proprietary software in the PC.

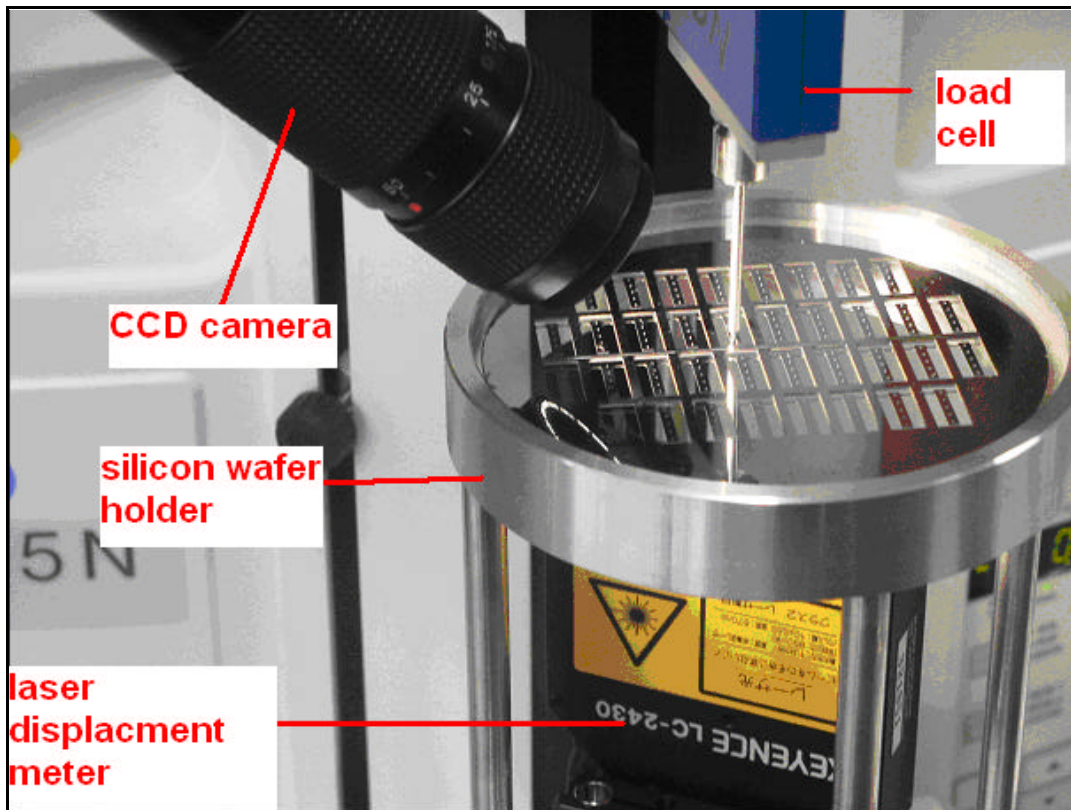


Fig 37: Experimental setup

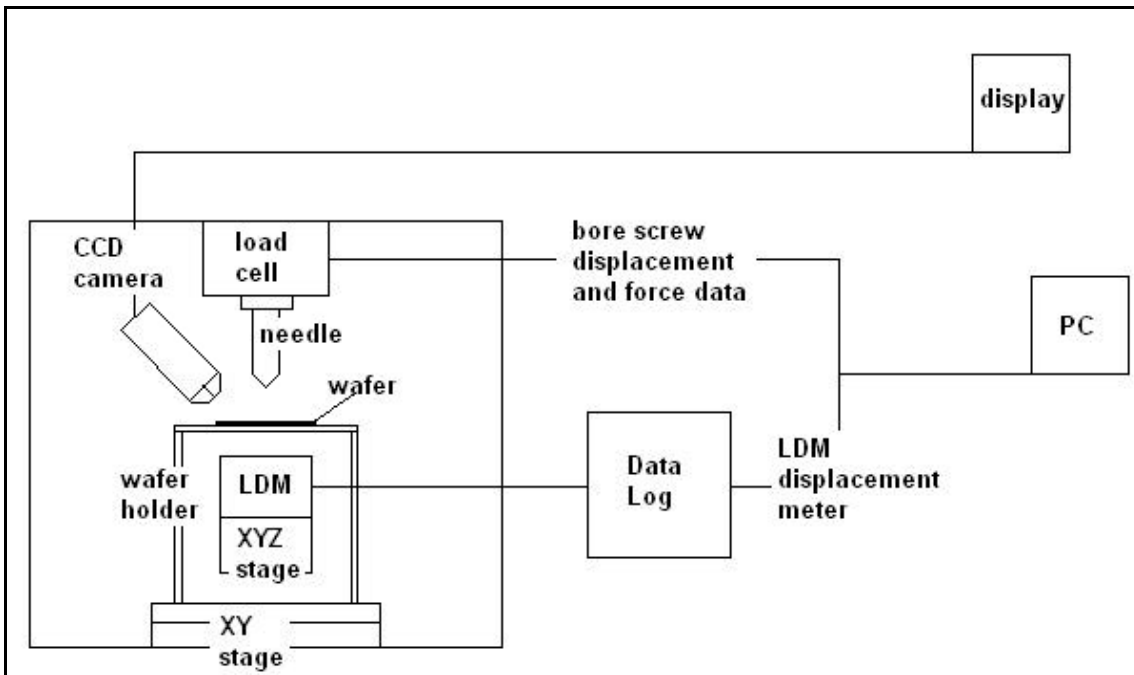


Fig 38: A schematic diagram showing the experimental setup

5.1.2 Wafers containing the test samples

4-inch (100)-oriented 150/1/400um thick SOI wafers were used. Bulking silicon micromachining was performed by means of the ICP-RIE equipment from Sumitomo Precision Products.

5.1.3 Silicon etching process

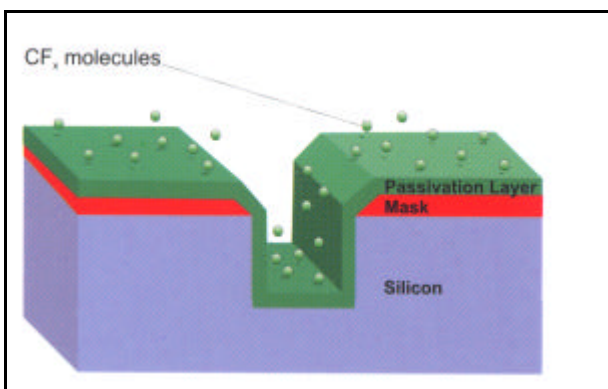


Fig 39: Passivation step

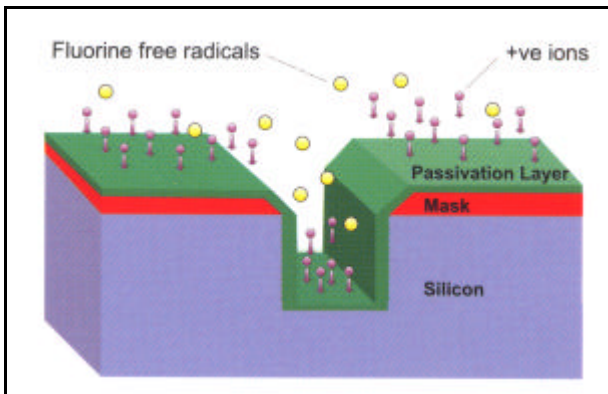


Fig 40: Etching step 1

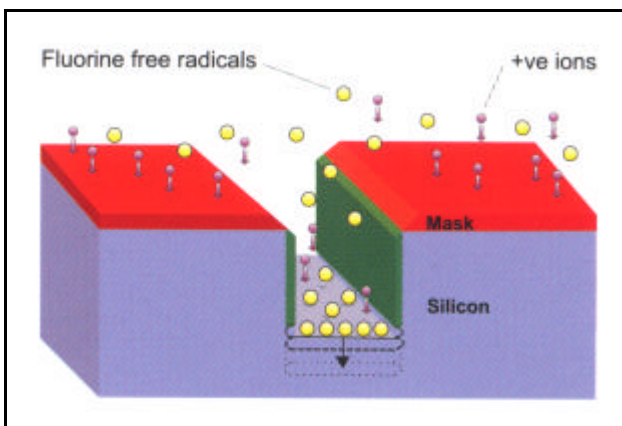


Fig 41: Etching step 2

Passivation step: (refer to fig (39)) At the beginning of each cycle, a C_4F_8 based plasma is used to conformally deposit a few monolayers of PTFE-like fluorocarbon polymer across all surfaces exposed to the plasma.

Etching step 1: (refer to fig (40)) The plasma gas is then switched to SF_6 to create a plasma chemistry that isotropically etches the silicon. Through the application of a D.C bias to the platen, ions from the plasma bombard the surface of the wafer, removing the polymer. Increased ion energy in the vertical direction results in a much higher rate of removal of fluorocarbon polymer from the surfaces parallel to the wafer surface.

Etching step 2: (refer to fig (41)) Following selective polymer removal, the silicon surface at the base of the trench is exposed to reactive fluorine-based species that isotropically etch the unprotected silicon. The remaining fluorocarbon polymer protects the vertical walls of the trench from etching.

By repeating the etching/passivation cycles and carefully controlling the etch time during each step, the degree of lateral etch is limited, allowing a trench to be etched vertically through the wafer.

Problem of lateral etching:

When reaching the insulator interface, charging of the dielectric surface leads to ion deflection that causes breakdown of the passivation at the base of the trench. The result of this breakdown is lateral etching known as notching, or “footing”, and this is undesirable for many applications.

5.1.4 Apparatus

- ‘EZ TEST’ testing machine from Shimadzu Corporation
- ‘LC-2400’ LDM (laser displacement meter) from Keyence Corporation
- Silicon wafer holder (made from Al)
- Load cell 5N (now 1N and 2.5N available)
- Artificial wafer used for laser alignment (made from acrylic)
- Software to process both force and displacement data
- XY stage and XYZ stage (manual alignment)
- Data logger (NS2000 from Keyence Corporation)
- PC (to display and record load cell and displacement data)
- CCD camera and flat-screen television (to locate and display the needle)
- LDM magnetic holder (to hold the LDM firmly to the surface)

5.1.5 Alignment of the laser spot

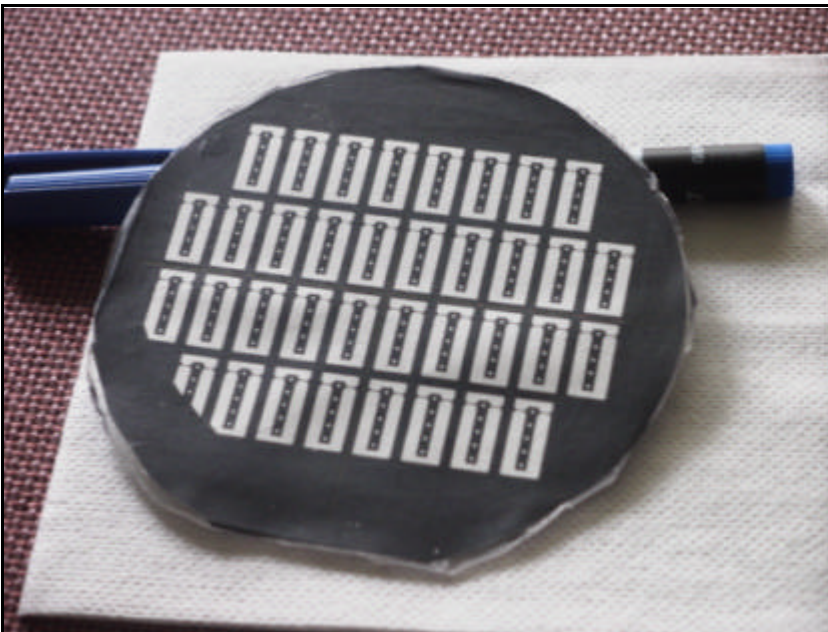


Fig 42: Artificial wafer used for laser spot alignment

Fig 42 shows an artificial wafer constructed to aid the laser spot alignment. The laser spot alignment is first achieved. Then the artificial wafer is removed and the actual wafer containing the specimens is put in its place. Note that after the laser spot alignment, care should be taken to ensure that the LDM magnetic holder is not disturbed or else laser spot alignment should be repeated once again.

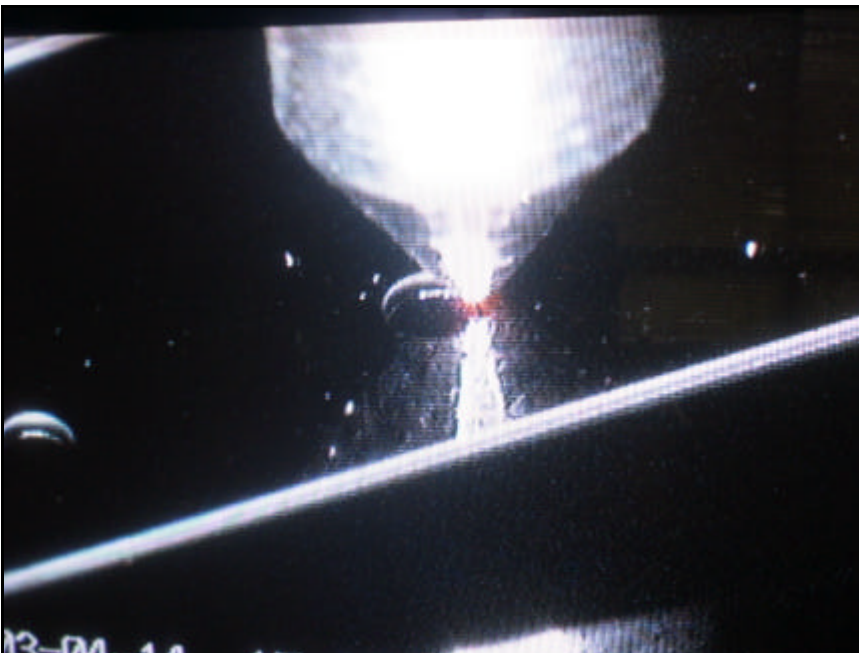


Fig 43: Aligning the position of the laser spot (note that the laser spot is at the tip of the needle)

5.1.6 Estimating the thickness of the wafer

- Direct measurement
- Interpolation method

Direct measurement:

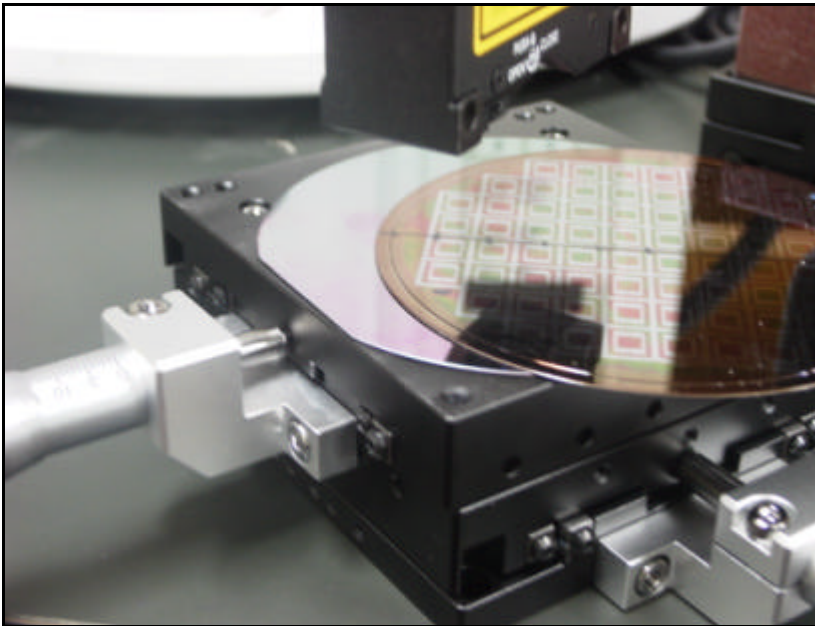


Fig 44: Directly measuring the thickness of wafer using the LDM

Interpolation method:

First, construct a displacement distribution function (refer to equation (58) shown below) for a range of wafer thickness from the FEM model at various initially specified locations on the wafer.

$$\boxed{\text{displacement} = F(t, x, y)} \text{ ----- (58)}$$

whereby x , y are the co-ordinates and t is the wafer thickness.

Then, depress the wafer at various locations and measure the displacement at each specified location using the LDM. Using the experimental displacement, interpolate the wafer thickness at various locations and obtain the mean wafer thickness. **The mean wafer thickness obtained in this manner will take into account the elastic properties of both the wafer and the testing system.**

5.1.7 Precautions in performing the test

- As a rough guide (in the case of pure bending), if the laser spot is off the point of maximum displacement by 10 μ m, the resulting difference in vertical displacement will be only about 0.033 μ m
- Next, it is noted that the spring constant K (change in force/ change in displacement) will not be adversely affected by the misalignment of the LDM.
- Finally, to prevent the slippage of needle during the experiment, it is advisable to initially depress the sample lightly several times (with the needle in the hole) before the main fracture test. Moreover, this is to also to ensure that the needle fits into the hole tightly.
- To aid easier fractography, it is advisable to label each sample systematic. Moreover, the front or back of each specimen should be labeled to enable easier recognition.
- The fixing of the laser spot can be aided by wearing a pair of green protective goggles. The green goggles cut off excessive light around the main laser spot.
- Calibration of the load cell should be done before the commencement of any experiment.
- Voltage drift may lead to slight difference in the LDM values recorded by the EZTest software and the data log software. Here, the LDM values from the data log software are more reliable and hence should be used instead.

5.2 Experimental procedures

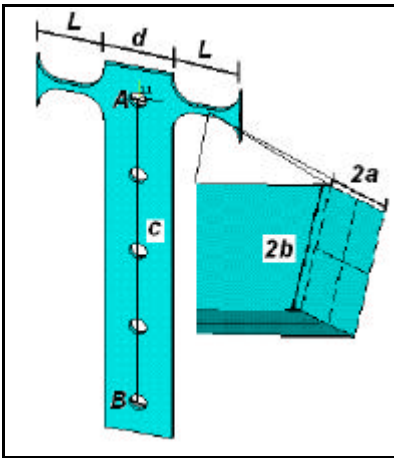


Fig 45: A: pure bending; B: combined loading

5.2.1 Pure bending

Firstly, pure bending was performed by applying the force at location **A** shown in Fig 45. Both the force and displacement (LDM) up to the point of fracture were recorded and then used to derive the nominal stresses (maximum principal stress) in the beam at the point of failure.

5.2.2 Combined loading

Next, combined loading test was performed by applying force at locations away from the mid-point of the plate, for instance at location **B** shown in Fig 45. Since the LDM displacement is not available as explained earlier in **3.3.1**, bore screw displacement from the testing machine (EZTEST) was recorded and used for analysis.

6 Experimental test results and discussion

6.1 FEM model overview

FEM model was constructed using ANSYS (FEM commercial software). Shell 93 elements were used to model the bulk of the wafer while hexahedron solid 95 elements were used to model the specimen in the submodel. In the coarse model, boundary conditions were applied to the edge of the wafer such that displacement in the z-direction was restricted. Besides, two separate points (refer to Fig (46) shown below) on the wafer were further restricted; one was restricted in both the x and y directions and the other was restricted in either x or y direction. (Note that if only one point was further restricted in both the x and y directions, the wafer will rotate about the point). Anisotropic material constant was used and geometrical nonlinearity was taken into account.

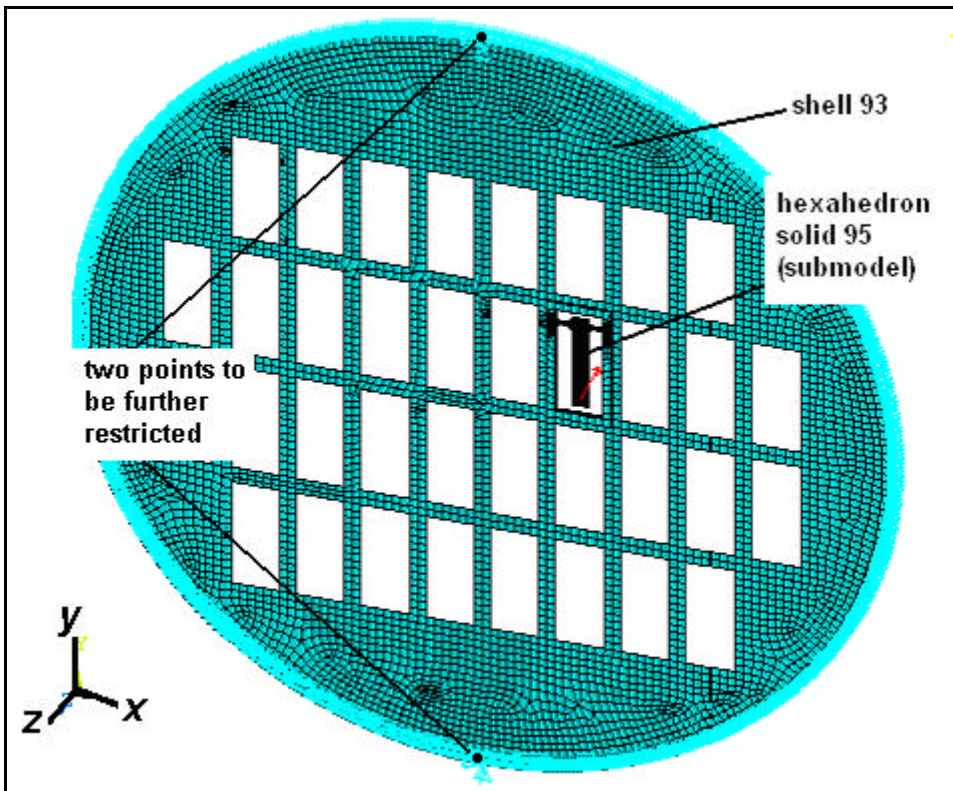


Fig 46: The overall FEM model (note that the submodel is superimposed over the coarse model)

Important note: the coordinate system in this research will be that shown in Fig 46 above.

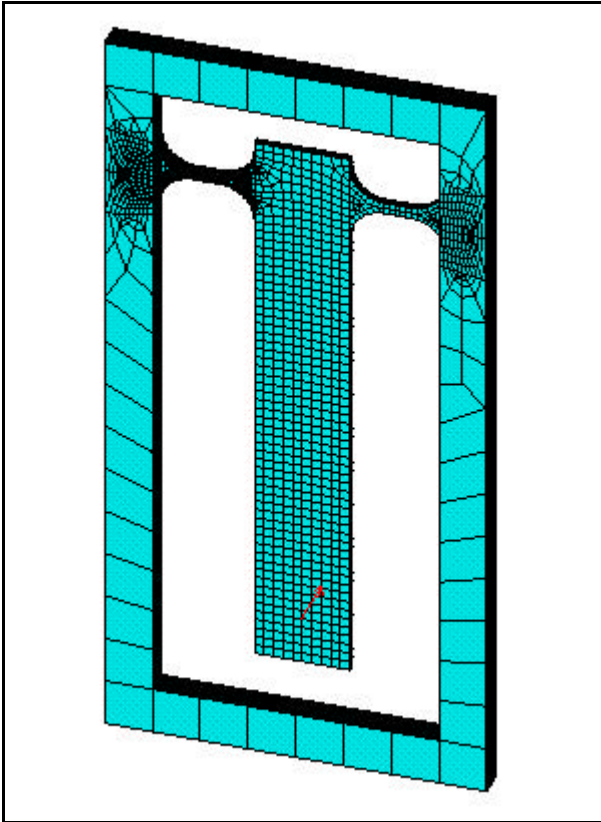


Fig 47: Submodel (constructed using hexahedron solid 95 elements)

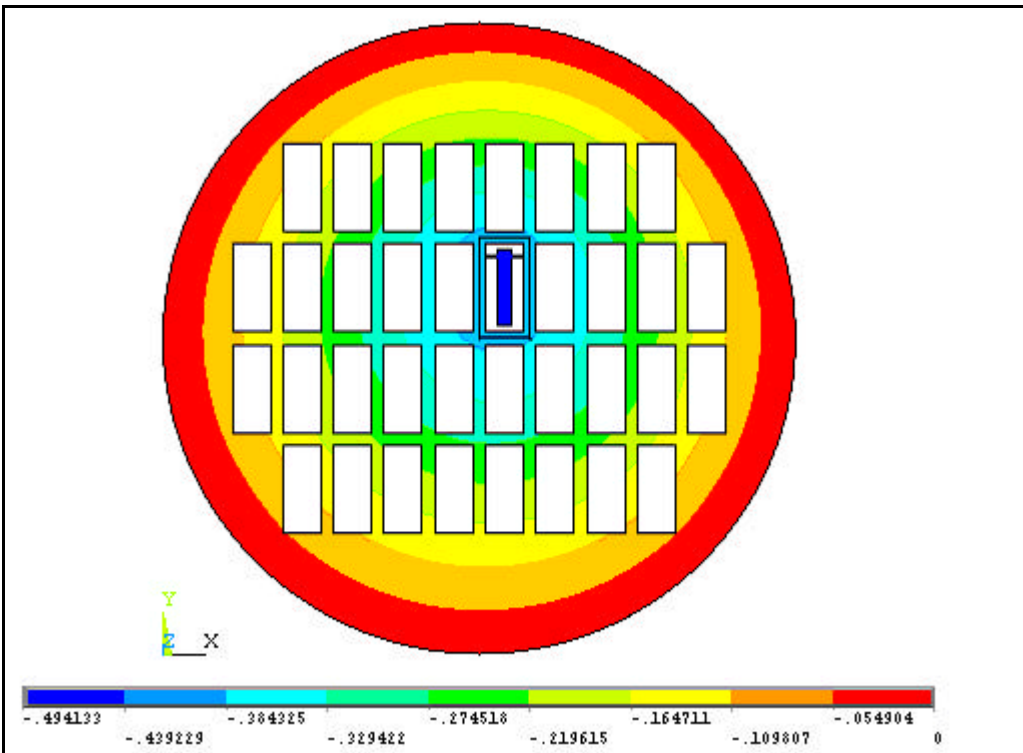


Fig 48: A typical displacement distribution in the z-direction for pure bending (note the nonsymmetrical distribution)

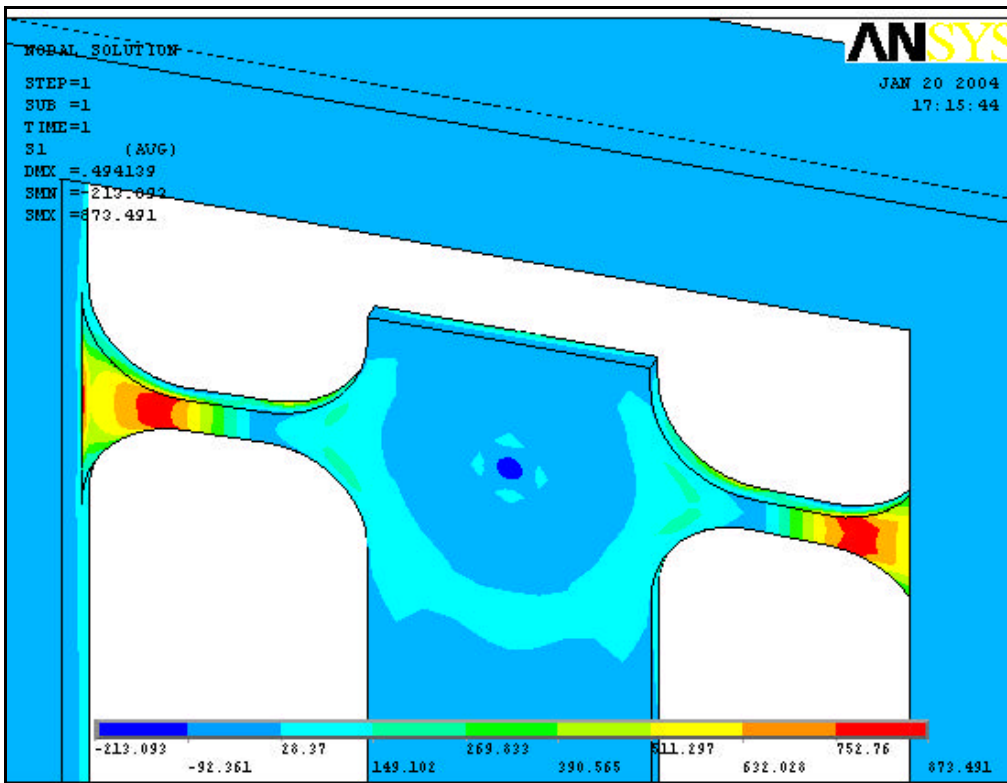


Fig 49: A typical principal stress distribution for pure bending (note that the mesh on the left beam is much finer than the mesh on the right beam)

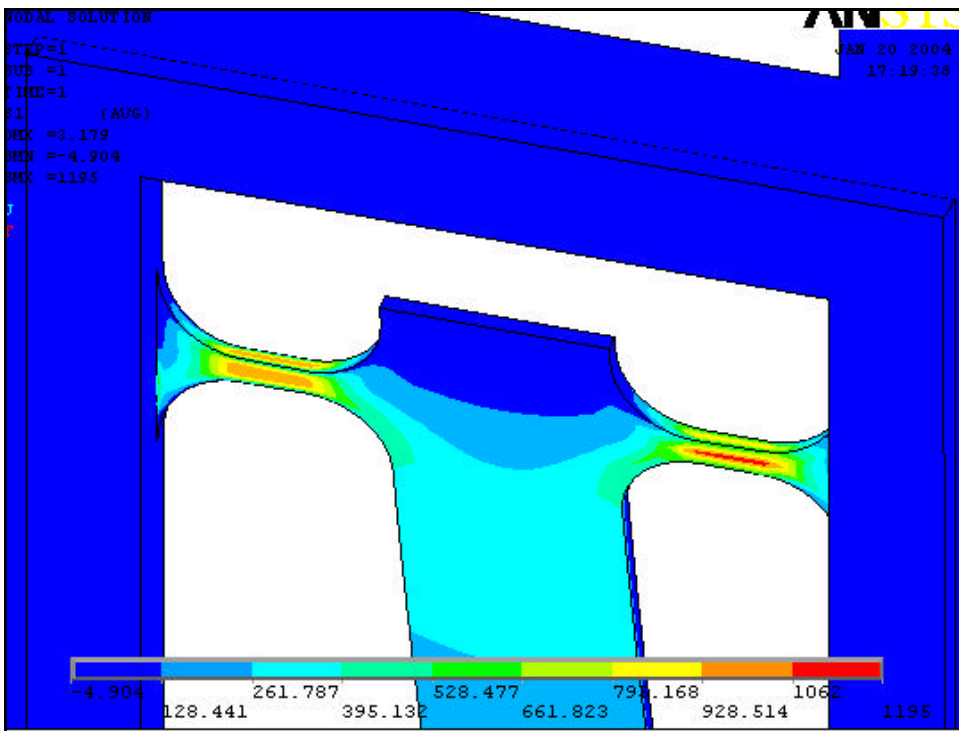


Fig 50: A typical principal stress distribution for combined loading (note that the mesh on the left beam is much finer than the mesh on the right beam)

6.2 Pure bending experimental and FEM results (batch 1; batch 2)

6.2.1 FEM fractured stresses

Table 5: Fractured stress for 240um samples (**batch 1**)

Sample No	FEM 1 [MPa]	FEM 2 [MPa]	Matching [%]
1	890	838	94
2	861	845	98
3	554	537	97
11	767	747	97
12	701	679	97

Table 6: Fractured stress for 300um samples (**batch 1**)

Sample No	FEM 1 [MPa]	FEM 2 [MPa]	Matching [%]
1	743	763	103
2	671	667	99
3	504	482	96
11	742	744	100
12	631	627	99

Table 7: Fractured stress for 240um samples (**batch 2**)

Sample No	FEM 2 [MPa]
1	737
10	811
11	795
12	759
13	732
15	812

Table 8: Fractured stress for 300um samples (**batch 2**)

Sample No	FEM 2 [MPa]
10	872
11	943
15	591

Note:

FEM 1: tetrahedron solid 95 is used to model the beam

FEM 2: hexahedron solid 95 is used to model the beam

6.2.2 Experimental and FEM displacements

Table 9: Displacement for 240um samples (**batch 1**)

Sample No	LDM disp [um]	FEM 1 [um]	FEM 2 [um]	Match b/w FEM 1 and Exp.	Match b/w FEM 2 and Exp.
1	515	526	494	102	96
2	497	501	474	101	95
3	288	291	281	101	98
11	480	494	468	103	98
12	401	405	388	101	97

Table 10: Displacement for 300um samples (**batch 1**)

Sample No	LDM disp [um]	FEM 1 [um]	FEM 2 [um]	Match b/w FEM 1 and Exp.	Match b/w FEM 2 and Exp.
1	476	478	453	100	95
2	NA	401	386	NA	NA
3	257	257	252	100	98
11	478	486	463	102	97
12	364	370	359	102	99

Table 11: Displacement for 240um samples (**batch 2**)

Sample No	LDM disp [um]	FEM 2 [um]	Match b/w FEM 1 and Exp.
1	462	445	96
10	540	521	96
11	511	493	96
12	433	427	99
13	329	333	101
15	462	434	94

Table 12: Displacement for 300um samples (**batch 2**)

Sample No	LDM disp [um]	FEM 2 [um]	Match b/w FEM 1 and Exp.
10	575	550	96
11	590	561	95
15	336	326	97

6.3 Combined loading experimental and FEM results (batch 1; batch 2)

6.3.1 FEM fractured stresses

Table 13: Fractured stress for 240um samples (**batch 1**)

Sample No	FEM 2 [MPa]
2	437
3	541
4	447
5	330
6	417
7	438
8	381
9	308
16	399
17	404
18	320

Table 14: Fractured stress for 300um samples (**batch 1**)

Sample No	FEM 2 [MPa]
2	359
3	337
4	269
5	199
6	260
7	251
8	224
9	224
16	247
17	221
18	196

Table 15: Fractured stress for 240um samples (**batch 2**)

Sample No	FEM 2 [MPa]
1	440
2	580
3	379
4	NA
5	454
6	599
7	675
8	670
9	598
10	549
11	587
12	529
13	506
14	514
15	455
16	443
17	482
18	NA

Table 16: Fractured stress for 300um samples (**batch 2**)

Sample No	FEM 2 [MPa]
1	310
2	288
3	368
4	285
5	248
6	295
7	280
8	291
9	241
10	333
11	395
12	371
13	391
14	201
15	267
16	340
17	NA
18	161

6.3.2 Experimental and FEM displacements

Table 17: Displacement for 240um samples (**batch 1**)

Sample No	Bore screw disp [μm]	FEM 2 [μm]
2	2.78	2.803
3	3.22	3.396
4	2.65	2.844
5	2.06	2.126
6	1.82	1.79
7	1.94	1.869
8	1.71	1.63
9	1.4	1.32
16	1.71	1.707
17	1.69	1.721
18	1.44	1.368

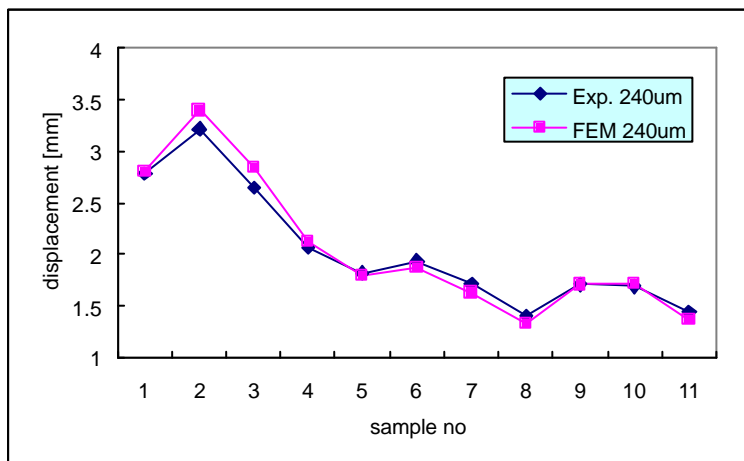


Fig 51: Matching of displacement between experiment and FEM for 240um combined loading (**batch 1**)

Table 18: Displacement for 300um samples (**batch 1**)

Sample No	Bore screw disp [um]	FEM 2 [um]
2	2.68	2.765
3	2.66	2.599
4	2.49	2.089
5	1.97	1.55
6	1.65	1.33
7	1.58	1.283
8	1.44	1.142
9	1.42	1.127
16	1.55	1.255
17	1.43	1.12
18	1.3	0.989

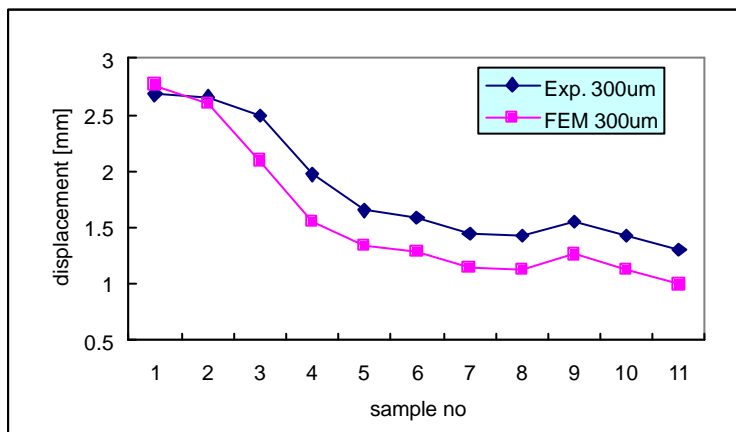


Fig 52: Matching of displacement between experiment and FEM for 300um combined loading (**batch 1**)

Table 19: Displacement for 240um samples (**batch 2**)

Sample No	Bore screw disp [um]	FEM 2 [um]
1	2.86	2.83
2	3.21	3.65
3	3.01	2.45
5	2.79	2.86
6	3.03	3.74
7	3.19	4.10
8	3.25	4.07
9	3.07	3.66
10	3.42	3.45
11	3.27	3.68
12	2.96	3.32
13	2.87	3.18
14	3.08	3.21
15	2.87	2.89
16	2.86	2.81
17	2.75	3.03

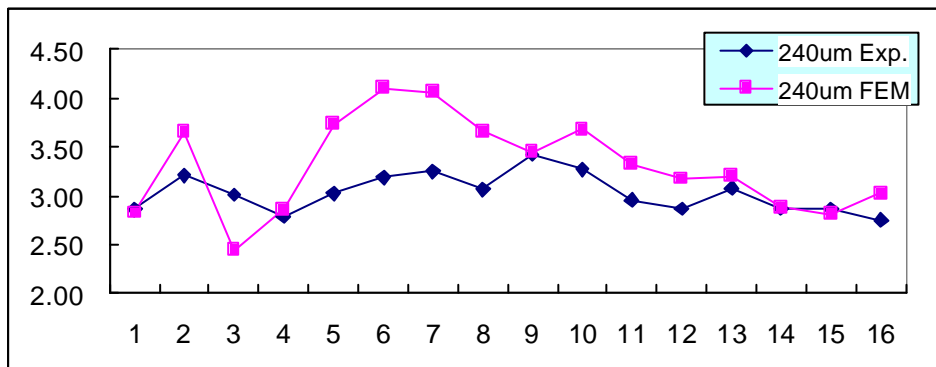


Fig 53: Comparison between the experiment and FEM displacement for 240um combined loading (**batch 2**)

Table 20: Fractured stress for 300um samples (**batch 2**)

Sample No	Bore screw disp [um]	FEM 2 [um]
1	2.67	2.42
2	2.51	2.25
3	2.82	2.82
4	2.54	2.20
5	2.20	1.92
6	2.56	2.29
7	2.40	2.18
8	2.46	2.25
9	2.25	1.87
10	2.75	2.58
11	2.94	3.01
12	2.59	2.83
13	2.50	2.96
14	1.75	1.57
15	2.40	2.07
16	2.32	2.60
18	1.81	1.27

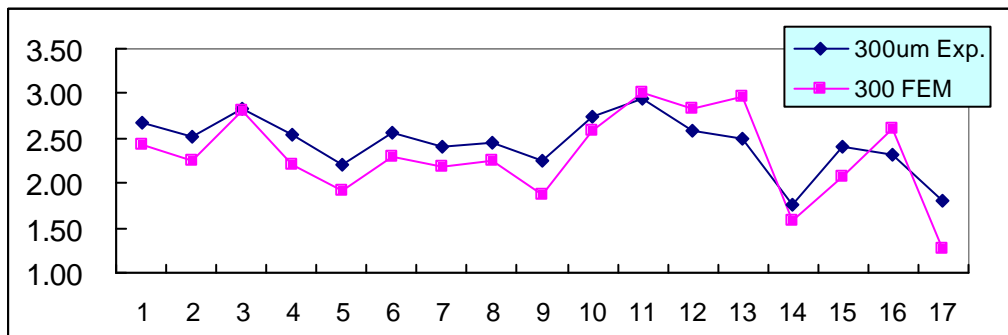


Fig 54: Comparison between the experiment and FEM displacement for 300um combined loading (**batch 2**)

6.4 Various types of fractured stress plots

6.4.1 Weibull plot for pure bending (240um and 300um samples)

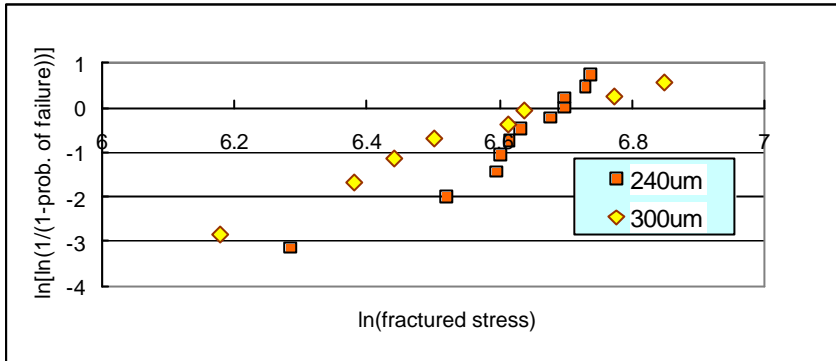


Fig 55: Separate Weibull plots for fractured stresses of 240um and 300um pure loading.

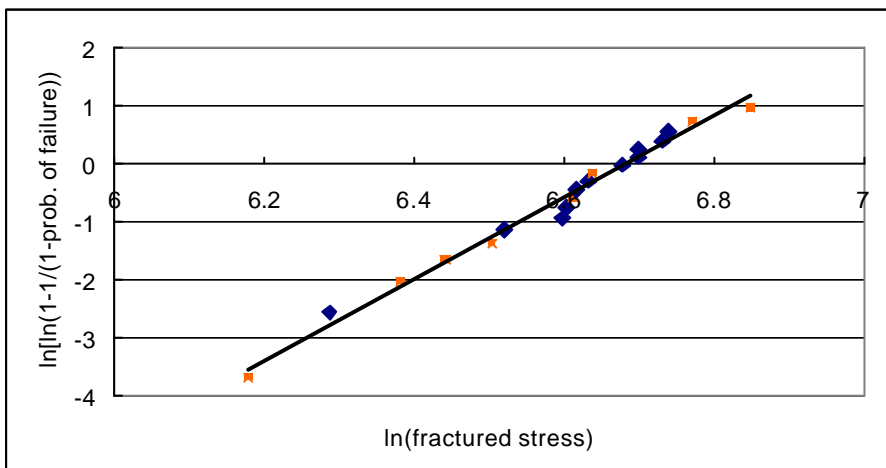


Fig 56: Combined Weibull plot for fractured stresses of 240um (blue) and 300um (orange) pure bending samples

From the separate Weibull plots (Fig 56) of the 240um and 300um samples, one can see that there is a high possibility that the flaw population in the 240um and 300um was of the same nature. Thus, a combined Weibull plot is then constructed. As can be seen from Fig 56, points for both the 240um and 300um samples fell on almost the same line.

[Note: in this research, median ranking is used for evaluating the failure probability.]

6.4.2 Weibull plot for combined loading (240um and 300um samples)

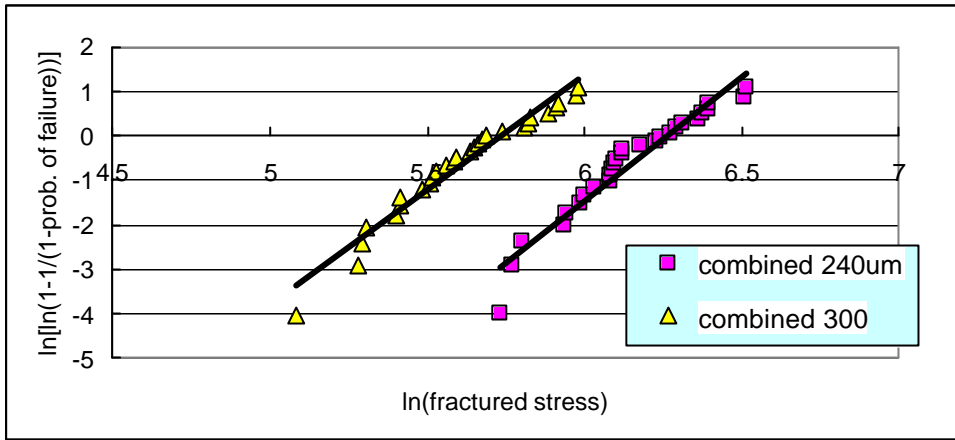


Fig 57: Weibull plot for combined loading fracture stresses (240um and 300um)

6.4.3 Fractured stress histogram

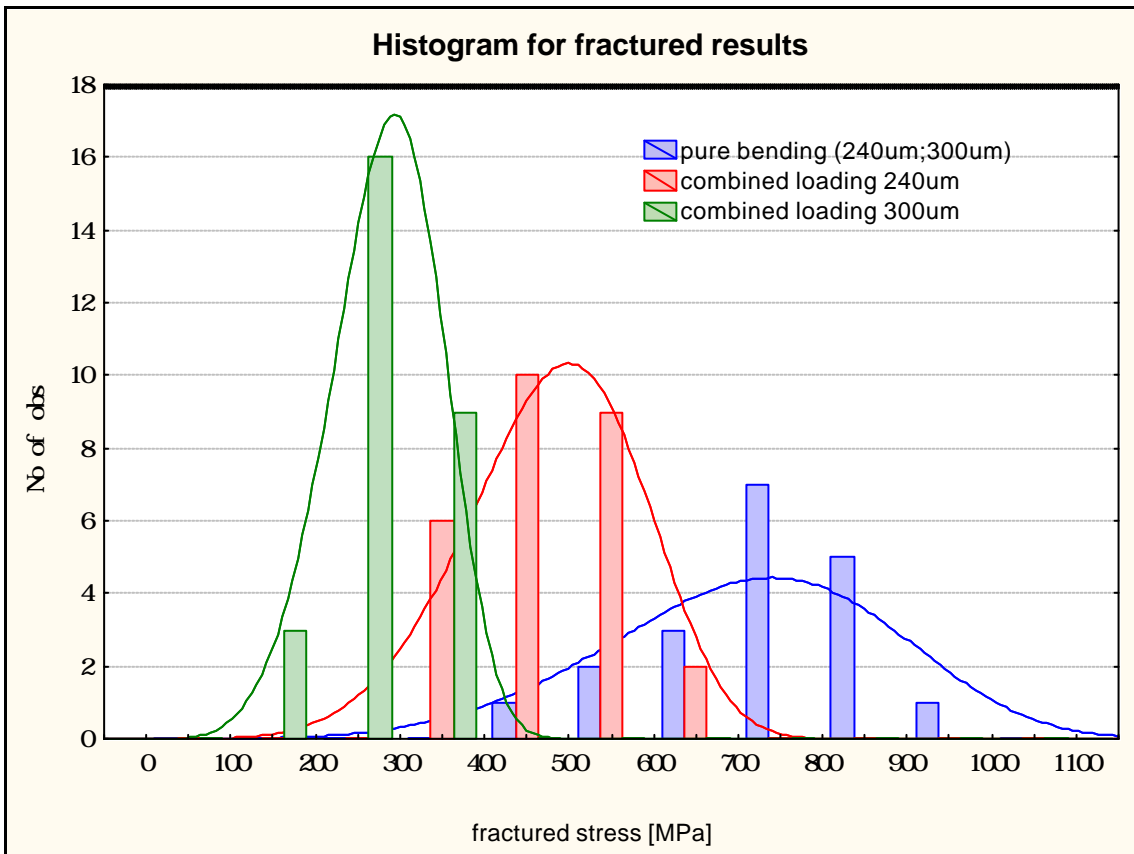


Fig 58: Fractured stress histograms

From the histogram (Fig 58), there appears to be three separate fractured stress distributions, pure bending being the strongest and 300um combined loading the weakest.

6.4.4 Weibull plot with 95% confidence intervals

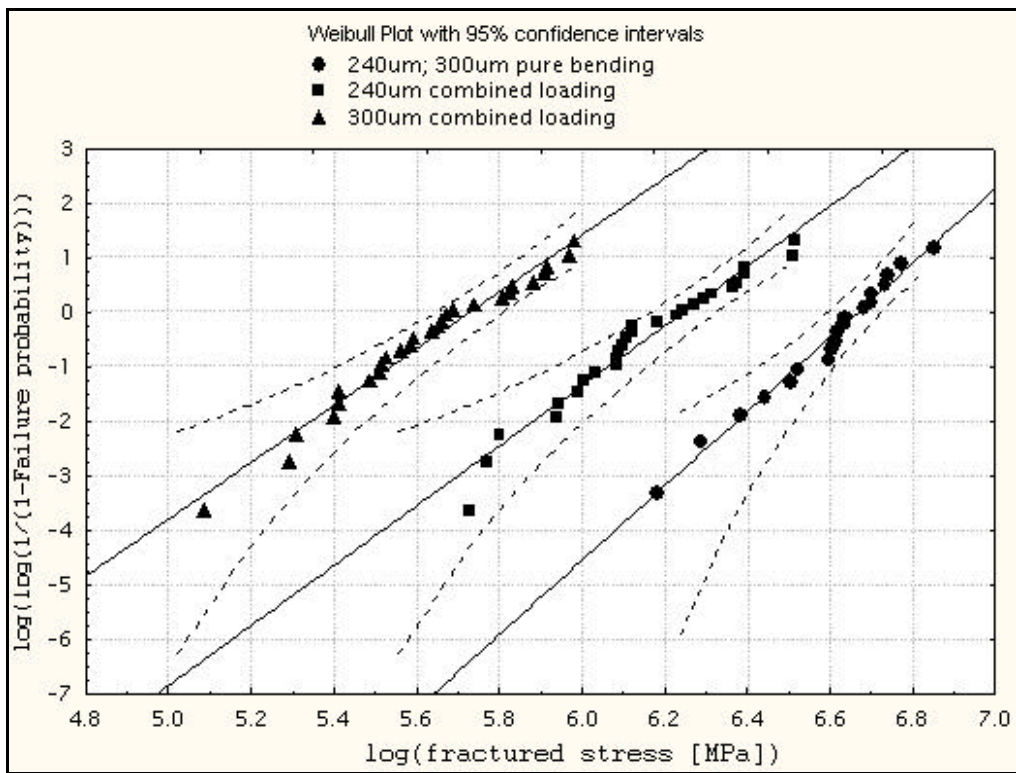


Fig 59: Weibull plot with 95% confidence intervals

6.5 Statistical treatment of experimental results

6.5.1 Overview

In this research, the Weibull parameters were estimated using the MLM (maximum likelihood method). Moreover, the goodness of fit (whether the distribution is indeed Weibull) was investigated by means of parametric (assumption of certain distribution) tests. Non-parametric tests (distribution-free) were also used to show that there was indeed difference in fractured stresses between the samples in the different geometry and loading configurations. Besides, two-parameter Weibull PDF was used to model the fractured stress and 95% confidence intervals were constructed by means of both the Bayesian update method and MLM. Both methods gave almost the same confidence intervals since both methods will be equivalent when there are many sample data. A three-parameter Weibull PDF was also used to fit the 240um and 300um combined loading samples and the possibility of a 3-parameter Weibull model briefly discussed.

6.5.2 Estimation of Weibull parameters

Table 21: MLM estimation of Weibull parameters

	Scale parameter [MPa]	Weibull modulus
Pure bending	783	7.77
240um combined	517	5.28
300um combined	306	4.98

Table 22: 95% confidence intervals for Weibull parameters calculated by means of the Bayesian update

	95% confidence interval			
	Scale [MPa]		Shape	
240 combined	475	563	3.70	6.60
300 combined	296	330	3.50	6.30
Pure bending	730	835	4.90	10.15

Table 23: 95% confidence intervals for Weibull parameters calculated by means of MLM (Maximum likelihood method)

	95% confidence interval			
	Scale [MPa]		Shape	
240 combined	480	558	3.97	7.03
300 combined	282	331	3.74	6.63
Pure bending	737	832	5.46	11.06

From the Table 22 and Table 23, one can see that the confidence intervals for the scale parameter do not overlap with one other. On the other hand, the shape (Weibull modulus) parameter for 240 and 300um combined loading overlaps largely. The shape parameter for pure bending overlaps to a smaller extent with combined loading.

6.5.3 Possibility of 3-parameter Weibull model

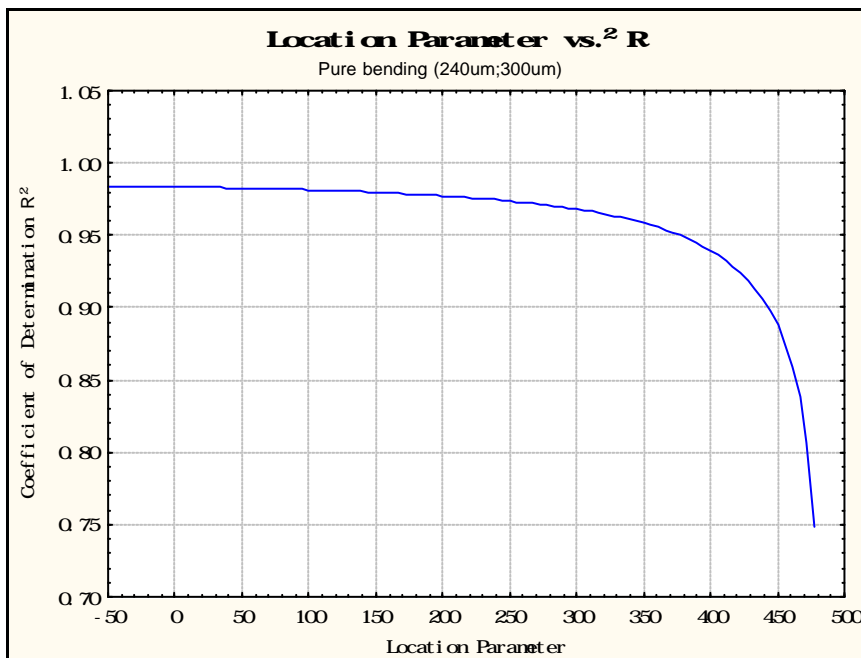


Fig 60: Plot of location parameter versus coefficient of determination for pure bending (240um; 300um)

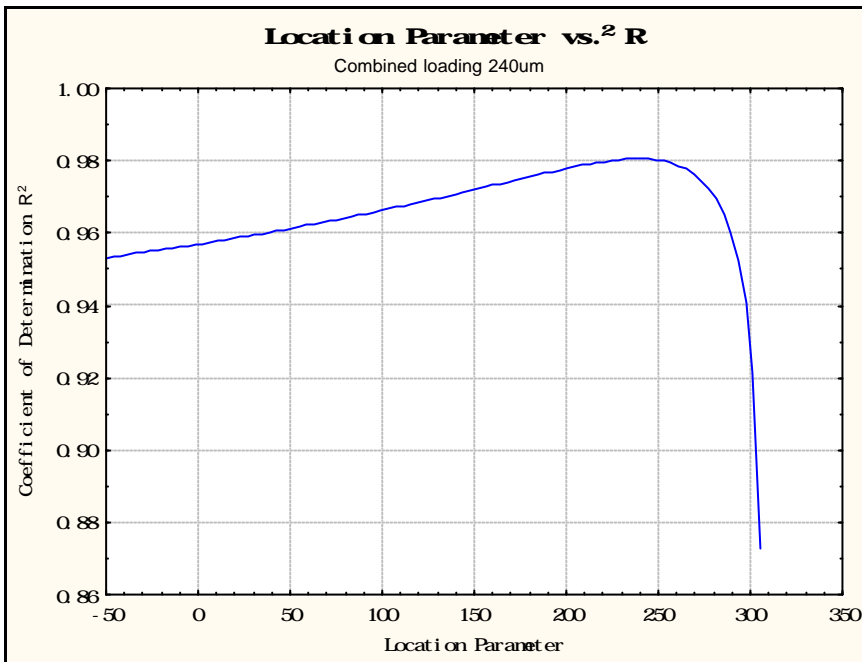


Fig 61: Plot of location parameter versus coefficient of determination for combined loading 240um

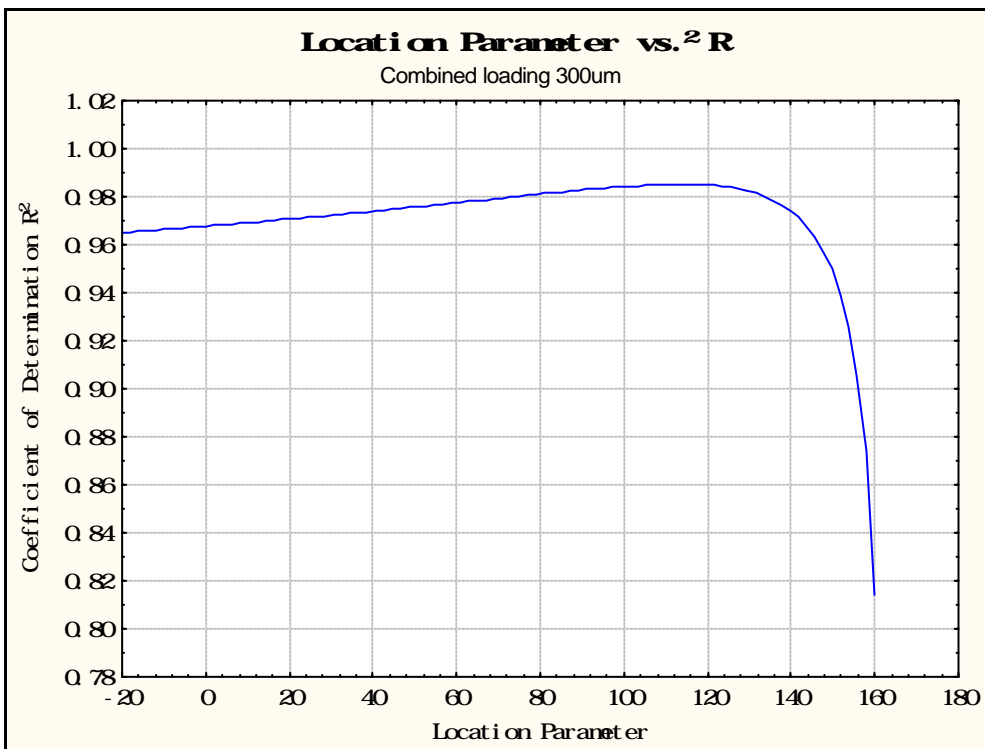


Fig 62: Plot of location parameter versus coefficient of determination for combined loading 300um

In the case of pure bending, since from Fig 60, one can see that there is no value of location parameter that leads to a maximum R^2 , the location parameter can be taken to be zero. On the other hand, for the cases of 240um and 300um combined loading, there exists a location parameter value that leads to a maximum R^2 . (Refer to Fig 61 and 62). Hence, the fracture stresses for 240um and 300um combined loading could be modeled by a 3-parameter Weibull parameters. Upon fitting a 3-parameter Weibull PDF to 240um and 300um combined loading samples, it was found that the both the both the scale and shape parameters became even smaller. (Refer to Table 24 and 25)

However, for this research the 2-parameter Weibull model was employed. Firstly, this is for simpler calculation. Secondly, there is no theoretical evidence that could suggest that a critical stress exists below which no fracture could possibly occur.

Table 24: 3-parameter Weibull PDF for 240um combined loading.

	Point estimation	Standard error	95% confidence intervals	
Location [MPa]	271.36	20.69	230.81	307.77
Shape	2.22	0.34	1.64	3.01
Scale [MPa]	232.29	21.12	194.37	277.61

Table 25: 3-parameter Weibull PDF for 300um combined loading.

	Point estimation	Standard error	95% confidence intervals	
Location [MPa]	135.30	15.06	105.79	161.48
Shape	2.53	0.38	1.88	3.40
Scale [MPa]	163.74	12.88	140.36	191.03

6.5.4 Parametric tests

A number of different tests have been proposed for evaluating the quality of the fit of the Weibull distribution to the observed data.

- Hollander-Proschan test: This test compares the theoretical reliability function to the Kaplan-Meier estimate. The Hollander-Proschan test is applicable to complete, single-censored, and multiple-censored data sets; however, the test may sometimes indicate a poor fit when the data are heavily single-censored. The Hollander-Proschan C statistic can be tested against the normal distribution.
- Mann-Scheuer-Fertig test: The null hypothesis for this test is that the population follows the Weibull distribution with the estimated parameters. Nelson (1982) reports this test to have reasonably good power, and this test can be applied to Type II censored data.
- Anderson-Darling test: The Anderson-Darling test (Stephens, 1974) is used to test if a sample of data came from a population with a specific distribution. It is a modification of the Komolgorov-Smirnov (K-S) test and gives more weight to the tails than does the K-S test. The K-S test is distribution free in the sense that the critical values do not depend on the specific distribution being tested. The Anderson-Darling test makes use of the specific distribution in calculating critical values. This has the advantage of allowing a more sensitive test and the disadvantage that critical values must be calculated for each distribution.
- Komolgorov-Smirnov test: An attractive feature of this test is that the distribution of the K-S test statistic itself does not depend on the underlying cumulative distribution function being tested. Another advantage is that it is an exact test (the chi-square goodness-of-fit test depends on an adequate sample size for the approximations to be valid). Despite these advantages, the K-S test has several important limitations: It only applies to continuous distributions. It tends to be more sensitive near the center of the distribution than at the tails. Perhaps the most serious limitation is that the distribution must be fully specified. That is, if location, scale, and shape parameters are estimated from the data, the critical region of the K-S test is no longer valid. It typically must be determined by simulation. Due to limitations above, many analysts prefer to use the Anderson-Darling goodness-of-fit test. However, the Anderson-Darling test is only available for a few specific distributions.
- Chi-square test: It is used to test if a sample of data came from a population with a specific distribution. An attractive feature of the chi-square goodness-of-fit test is that it can be applied to any univariate distribution for which you can calculate the cumulative distribution function. The chi-square

goodness-of-fit test is applied to binned data (i.e., data put into classes). This is actually not a restriction since for non-binned data you can simply calculate a histogram or frequency table before generating the chi-square test. However, the values of the chi-square test statistic are dependent on how the data is binned. Another disadvantage of the chi-square test is that it requires a sufficient sample size in order for the chi-square approximation to be valid. The chi-square test is an alternative to the Anderson-Darling and Komolgorov-Smirnov goodness-of-fit tests. The chi-square goodness-of-fit test can be applied to discrete distributions such as the binomial and the Poisson. The Komolgorov-Smirnov and Anderson-Darling tests are restricted to continuous distributions.

6.5.5 Anderson-Darling test

For the **Weibull** (and **Gumbel**) distributions, the test statistic, A^2 can be calculated from equation (59):

$$A^2 = -n - \frac{1}{n} \sum_{i=1}^n (2i-1) [\ln(w_i) + \ln(1-w_{n-i+1})] \quad \text{-----(59)}$$

w is the CDF for the distribution under consideration. For the Weibull PDF this is given in equation (60):

$$F(x) = 1 - \exp \left[- \left(\frac{x_i}{b} \right)^a \right] \quad \text{-----(60)}$$

whereby α , β , are the shape and scale parameters respectively. This formula needs to be modified for small samples (refer to equation (61)):

$$A_m^2 = A^2 \left(1 + \frac{0.2}{\sqrt{n}} \right) \quad \text{-----(61)}$$

and then compared to an appropriate critical value from the Table 26 below:

Table 26: Critical values for Anderson-Darling test

Level of significance	0.1	0.05	0.025	0.01
A^2_{crit}	0.637	0.757	0.877	1.038

The test is a one-sided test and the hypothesis that the distribution is of a specific form is rejected if the test statistic, A , is greater than the critical value.

6.5.6 Results of parametric tests

Table 27: Goodness of fit tests for testing samples.

	Pure bending		Combined loading 240um		Combined loading 300um	
	Test value	P value	Test value	P value	Test value	P value
Hollander-Proschan	-0.048004	.96171	0.239840	.81045	0.229276	.81865
Mann-Scheuer-Fertig	0.496904	P>.25	NA	NA	NA	NA
Anderson-Darling	0.181625	P>.20	0.391253	P>.20	0.364612	P>.20

Conclusion: There is statistical evidence to show that the test samples indeed follow a Weibull PDF.

6.5.7 Non-parametric test

Many statistical tests and procedures are based on specific distributional assumptions. The assumption of normality is particularly common in classical statistical tests. Much reliability modeling is based on the assumption that the distribution of the data follows a Weibull distribution.

There are many non-parametric and robust techniques that are not based on strong distributional assumptions. By non-parametric, we mean a technique, such as the sign test, that is not based on a specific distributional assumption. By robust, we mean a statistical technique that performs well under a wide range of distributional assumptions. However, techniques based on specific distributional assumptions are in general more powerful than these non-parametric and robust techniques. By power, we mean the ability to detect a difference when that difference actually exists. Therefore, if the distributional assumption can be confirmed, the parametric techniques are generally preferred.

If you are using a technique that makes a normality (or some other type of distributional) assumption, it is important to confirm that this assumption is in fact justified. If it is, the more powerful parametric techniques can be used. If the distributional assumption is not justified, a non-parametric or robust technique may be required.

The Kruskal-Wallis H test is a nonparametric test for deciding whether two samples come from the same population. A generalization for this for k samples is provided by the Kruskal-Wallis H test, or briefly the H test.

This test may be described as: Suppose that we have k samples of sizes $N_1, N_2, N_3, \dots, N_k$, with the total size of all samples taken together being given by $N = N_1 + N_2 + N_3 + \dots + N_k$. Suppose that further that the data from all the samples taken together are ranked and that the sums of the ranks for the k samples are $R_1, R_2, R_3, \dots, R_k$, respectively. If we define the statistic (equation (62)):

$$H = \frac{12}{N(N+1)} \sum_{j=1}^k \frac{R_j^2}{N_j} - 3(N+1) \quad \text{-----(62)}$$

Then it can be shown that the sampling distribution of H is very nearly a chi-distribution with $(k-1)$ degrees of freedom, provided that $N_1, N_2, N_3, \dots, N_k$ are all at least 5. The H test provides a nonparametric method in the analysis of variance for one-way classification, or one-factor experiments, and generalizations can be made.

In the case that there are too many ties among the observations in the sample data, the value of H given by the equation (62) is smaller than it should be. The

corrected value of H, denoted by H_c is obtained by dividing the value given in equation (62) by the correction factor given in equation (63):

$$1 - \frac{\sum T^3 - T}{N^3 - N} \text{-----(63)}$$

where T is the number of ties corresponding to each observation and where the sum is taken over all the observations. If there are no ties, then T=0 and the correction factor reduces to 1, so that no correction is needed. In practice, the correction is usually negligible (. i.e., it is not enough to warrant a change in the decision).

Assumptions and interpretation: It is assumed that the variable under consideration is continuous and that it was measured on at least an ordinal (rank order) scale. The test assesses the hypothesis that the different samples in the comparison were drawn from the same distribution or from distributions with the same median. Thus, the interpretation of the Kruskal-Wallis test is basically identical to that of the parametric one-way ANOVA, except that it is based on ranks rather than means

6.5.8 Results of non-parametric test

Table 28: H test results for 240 and 300um samples

Between	H statistics	Degree of freedom	Chi-Square 95 percentile value	Decision	Conclusion
240um and 300um pure bending	0.55	1	3.84	Do not reject H0	No difference between samples
240um and 300um combined loading	34.52	1	3.84	Reject H0	Significant difference between samples
Pure bending (240um, 300um), 240um combined loading and 300um combined loading	58.20	2	5.99	Reject H0	Significant difference between samples

Additional notes:

Null hypothesis, H₀: No significant difference in fracture stresses between the samples

Alternative hypothesis, H₁: Significant difference in fracture stresses between the samples

Level of significance: 5%

Conclusion: There is statistical evidence to show that the fractured stresses of the samples are indeed different from each other.

6.6 Explanations for differences in strength

6.6.1 Overview

The load factor analysis is used to explain the differences in fractured stresses between the samples. The load factor PDF is an intrinsic characteristic for a specific geometry and loading configuration. The differences in fracture stresses were postulated to be due to the differences in the apparent flaw distributions. In this research, it is assumed that a specific flaw population (flaw size, flaw orientation, density) exists in each location in the beam and this specific flaw population is assumed constant through the wafer. To be more specific, the flaw distribution (size, orientation, density) may vary depending on the location on each beam. However, there is no difference in flaw distribution between any two specimens at the same location of the beam.

Firstly, selection of a path suitable for stress and load factor analysis is discussed. Then, explanations for the differences in fractured stresses between the samples were offered, and the inferences on the nature of the flaw population were made, supported by SEM photos of flaws at various locations on the beams.

6.6.2 Selection of a suitable path

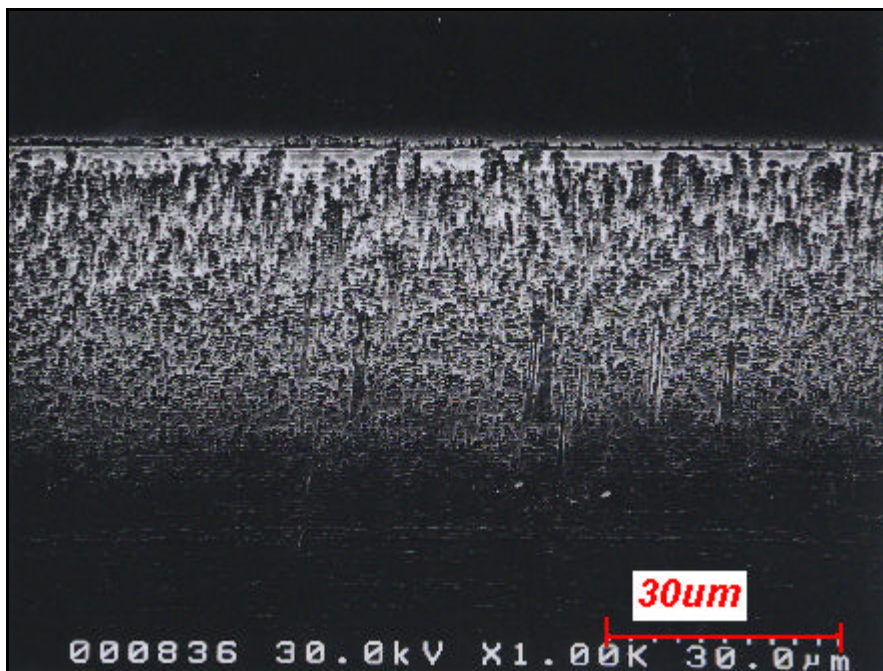


Fig 63: Extent of flaw across the beam height

There is fractographic evidence to show that the flaw at most covers about 25% of the beam sidewalls. (Refer to Fig 63) The rationale for using a line path instead of an area path for stress and load factor analysis is that crack initiation sites occur exclusively at the edge of the beam. Although higher principal stresses may occur

towards the middle section of the beam, there is no fractographic evidence that shows crack initiating at the middle section of the beam. Moreover, flaws become progressively larger as one approaches the edge of the beam. Furthermore, from a fracture mechanics point of view, a flaw on the surface of the beam will have a greater stress intensity factor than a flaw in middle of the beam and thus will be more susceptible to fracture. In using the line path, one will implicitly assume that cracks on the line path are independent and hence do not interact with each other. The validity of such an assumption is questioned since overlaps of flaw could be observed in SEM photos.

The reason for the formation of such flaws is given as:

When reaching the insulator interface, charging of the dielectric surface leads to ion deflection that causes breakdown of the passivation at the base of the trench. The result of this breakdown is lateral etching known as **notching**, or “footing”, and this is undesirable for many applications.

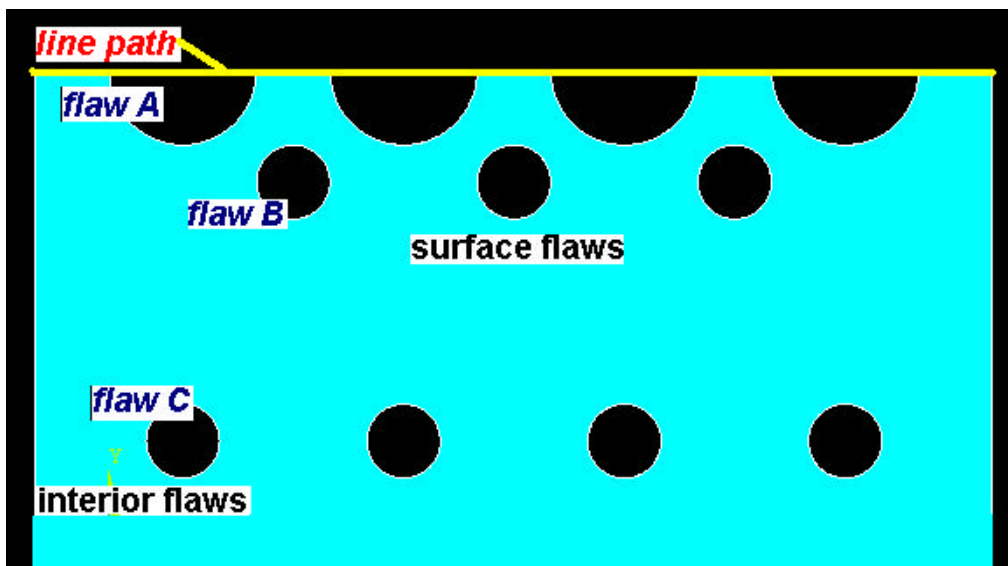


Fig 64: Explanation of interactions between flaws

Assume that a line path is chosen. Here, the validity of such a line path is discussed.

For instance, (refer to Fig 64) consider three flaws, namely flaw A, B and C. Flaw A and B are surface flaws while flaw C is an interior flaw. Suppose, a stress distribution acts on the beam and since surface flaws have a much higher probability of initiation, it is logical to assume that one of the surface flaws will be the site for crack initiation. Furthermore, suppose that there are interactions between flaw A and B.

- Case 1: assume that flaw A is the crack initiation site: since flaw A lies on the line path, the use of the line path is valid.
- Case 2: assume that flaw B is the crack initiation site (this is possible since flaw B is very near the edge of the beam: If flaw B were to crack initially, the stress around flaw B will be intensified and consequently, stress around flaw A will also be intensified. Hence, if flaw B were to interact with flaw A, flaw A will almost instantaneously crack after flaw B crack since the two cracks are in close proximity with each other. Since the two flaws are close to each other, the nominal stress estimated along line path can still be used for analysis.
- Case 3: assume that flaw C is the crack initiation site (the possibility of failure from in interior flaw is very low). The nominal stress at the interior of the beam should be higher than at the edge of the beam. Since the extent of the flaw is about 20% of beam sidewalls, the difference in nominal stress between the two locations (surface and interior) will not be too large. Thus, the stress estimated by the line path will be lower than the actual stress, which is safe from the point of view of design.

In conclusion, the use of the line path for this specific type of flaw population should be valid.

6.6.3 Illustrations of path A and path B

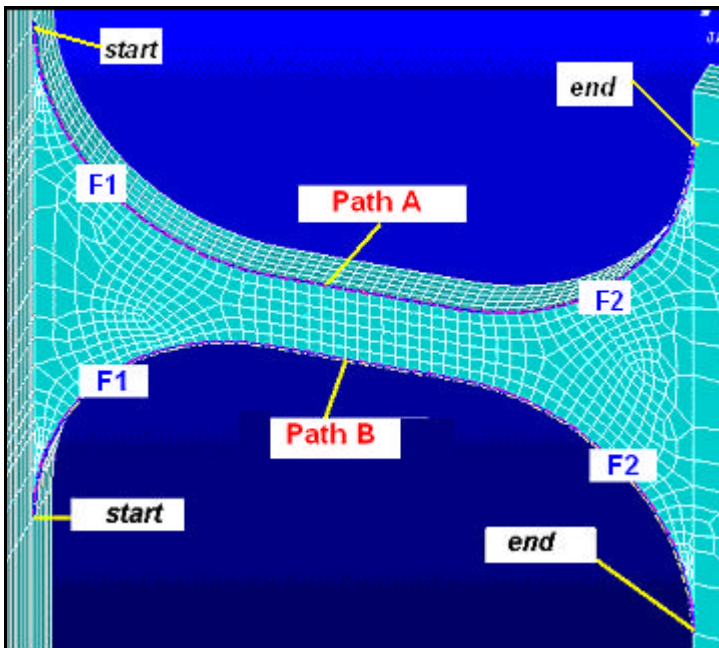


Fig 65: Representation of *path A and B* in the beam and *fillet region F1 and F2* on the beam. (Start: start of path; end: end of path)
[Shorter Path B used for pure bending and pure torsion]

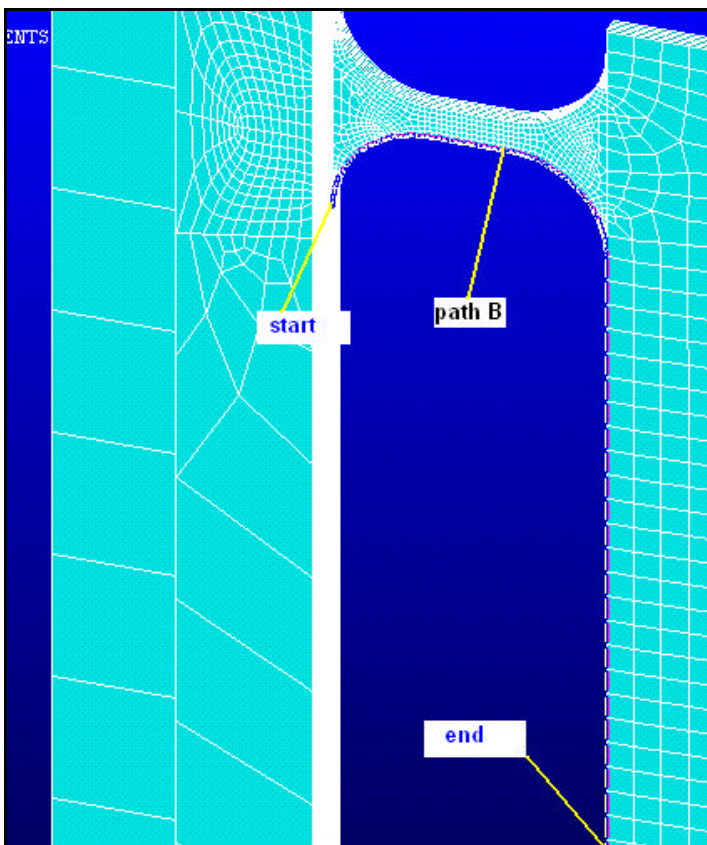


Fig 66: Longer Path B used for combined loading

For pure bending and pure torsion, the principal stress distribution at the path A and path B of the beams are the similar. Hence, only path A results will be shown.

In the case of combined loading, stress distribution at path A and B are dissimilar and results for both path A and path B will be shown.

Moreover, for the case of pure bending and pure torsion, path B shown in Fig 65 is sufficient. On the other hand, for the case of combined loading, because of the nature of combined loading, the stress distribution on path B is very board and a much longer path B (shown in Fig 66) was required.

6.6.4 Typical load factor values for path A and path B

Table 29: Typical load factor values

	Load factor	
	Path A	Path B
240 pure bending	0.0687	0.0687
300 pure bending	0.0637	0.0637
240 combined	0.0748	0.319
300 combined	0.0703	0.266

Table 30: No of times a sample appears to be stronger when compared to samples stressed by a uniform tensile stress (note that lower values will mean relative lower strength)

	Comparison with uniform tensile stress	
	Path A	Path B
240 pure bending	1.41	1.41
300 pure bending	1.43	1.43
240 combined	1.63	1.24
300 combined	1.70	1.30

$$\frac{\bar{s}_i}{\bar{s}_{tension}} = \left(\frac{1}{Lf_i} \right)^{1/m_i} \text{-----(64)}$$

whereby $\bar{s}_{tension}$ is the mean stress for uniform tension, and Lf_i the load factor, m_i the Weibull modulus and \bar{s}_i the mean stress for case i . The formula shown in equation (64) is used to calculate Table (30) shown above.

Table 31: mean and SD values for fractured stresses

	Pure bending	Combined 240um	Combined 300um
Mean [MPa]	736.33	476.18	280.89
SD [MPa]	112.27	103.77	64.58
COV	0.15	0.22	0.23

Typical load factor values are shown above in Table 29 and the number of times a sample appears to be stronger when compared to similar samples stressed by uniform tensile stress are given in Table 30.

As can be observed from Table 29 and Table 30, differences in the load factor alone cannot account for the large difference in strength between pure bending and combined loading samples.

It should be noted that since the principal stress direction for the case of pure bending is not the same as that for combined loadings, **the load factor value couldn't be compared directly**. However, one can infer that **any difference in strength not explained by the load factor could be attributed to the differences in maximum principal stress direction between the pure bending and combined loading**.

6.6.5 Typical stress distribution plots

Pure bending path and stress contrast plots:

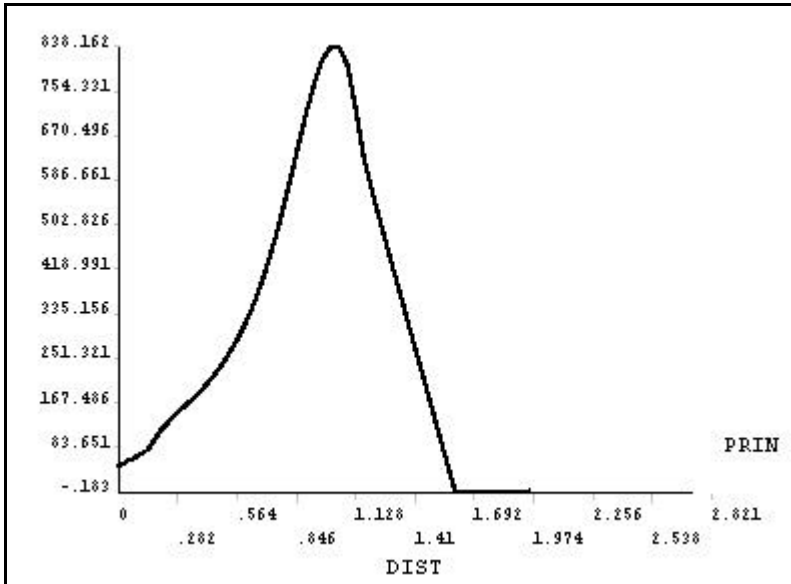


Fig 67: A typical maximum principal stress (nodal-stress) plot along **path A** or **path B**

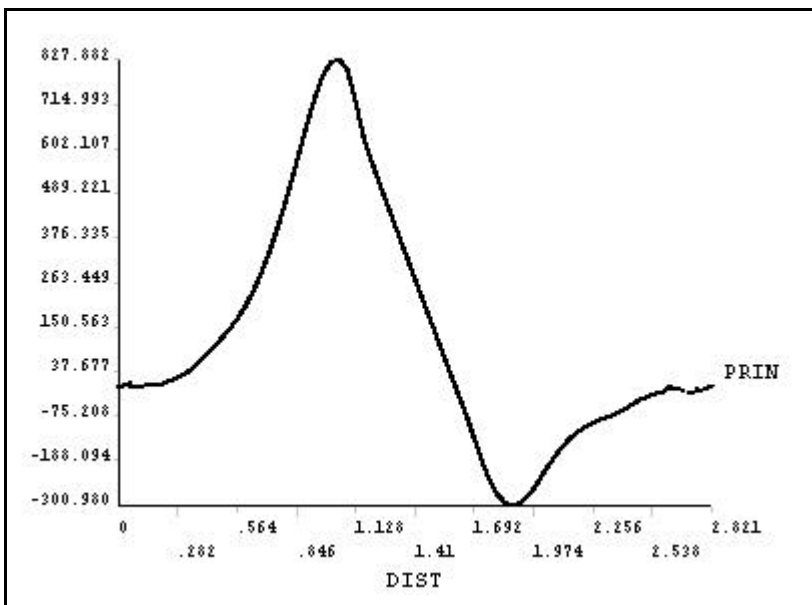


Fig 68: A typical stress X (nodal-stress) plot along **path A** or **path B**

It can be observed that the maximum value for both the maximum principal stress and stress X is almost the same. It is because the maximum principal stress direction is almost the same as that for stress X, i.e., that is along the beam-length direction.

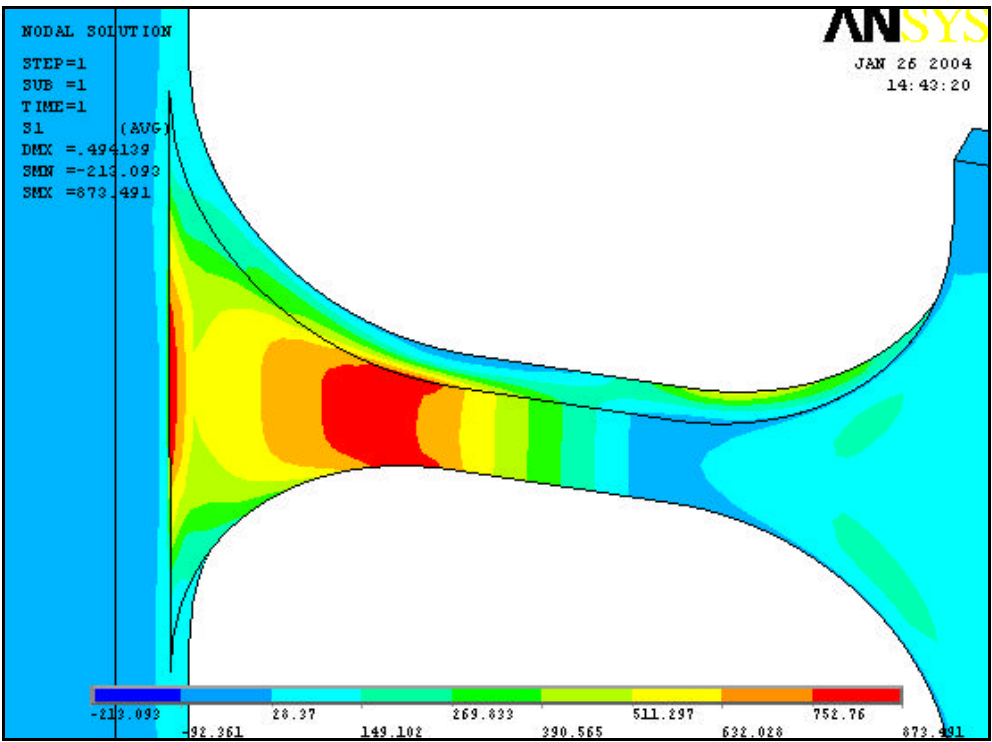


Fig 69: A typical maximum principal stress contrast plot for pure bending

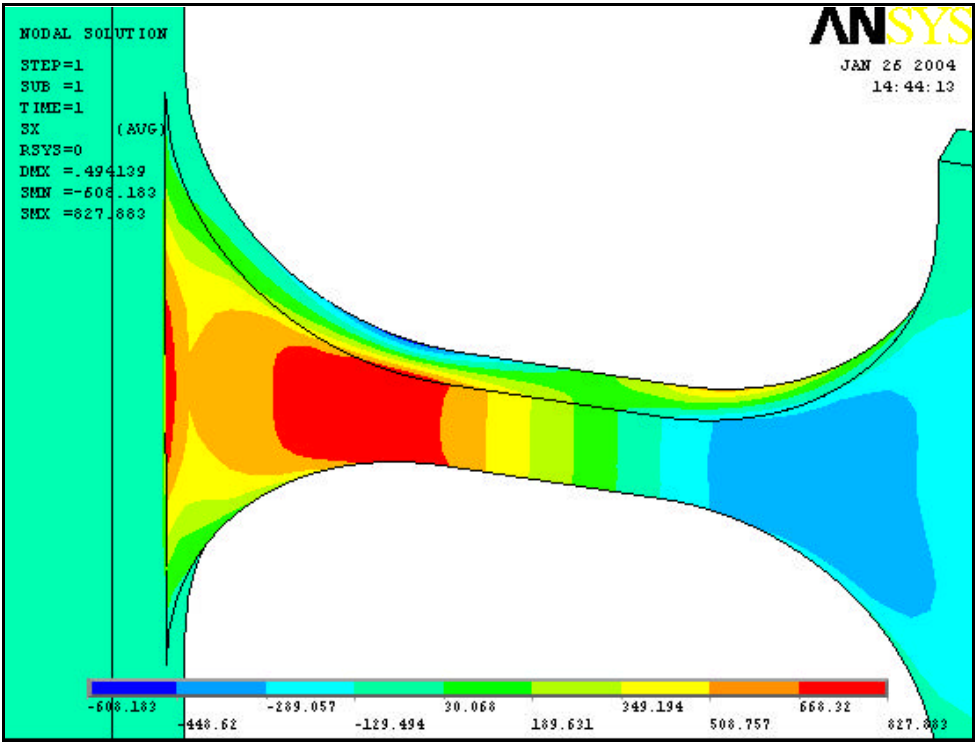


Fig 70: A typical stress X contrast plot for pure bending

Combined loading path plots:

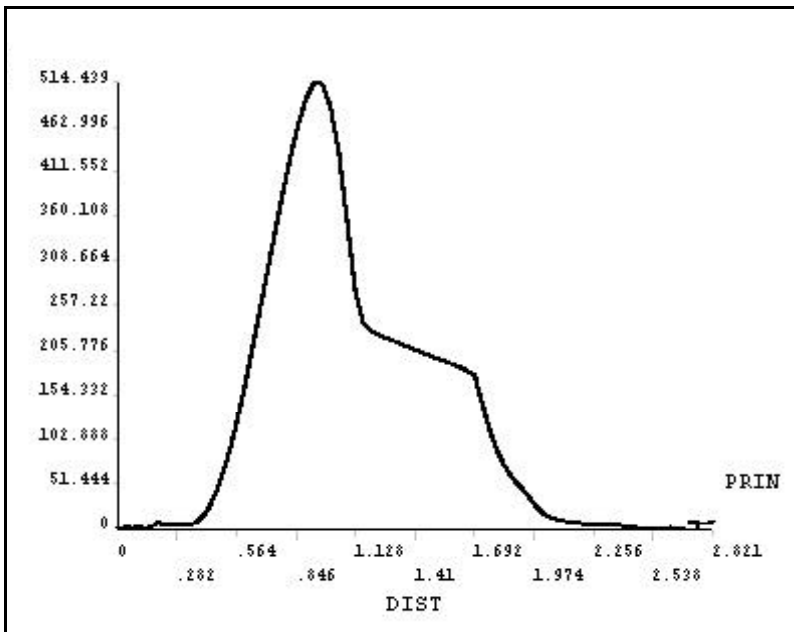


Fig 71: A typical maximum principal stress (nodal-stress) plot along **path A**

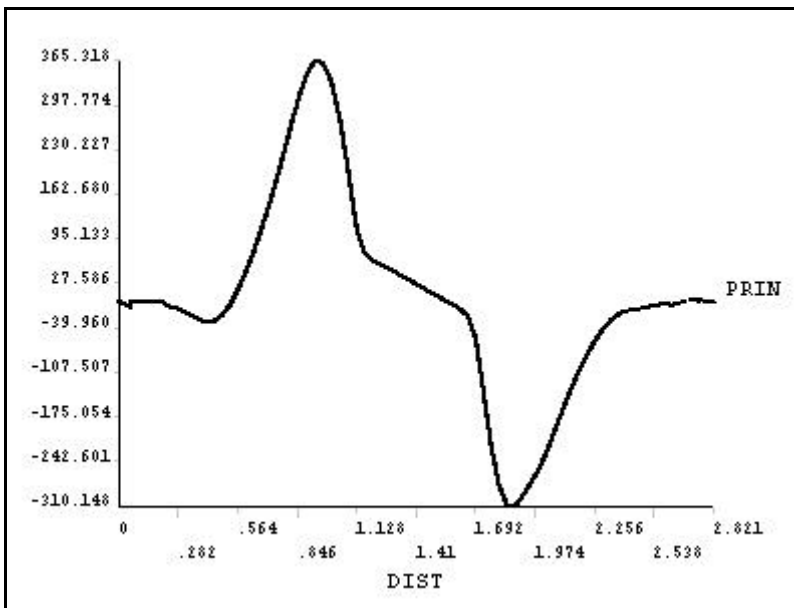


Fig 72: A typical stress X (nodal-stress) plot along **path A**

It can be observed that the maximum value for both the maximum principal stress and stress X is quite different. It is because the maximum principal stress direction is different from that of stress X.

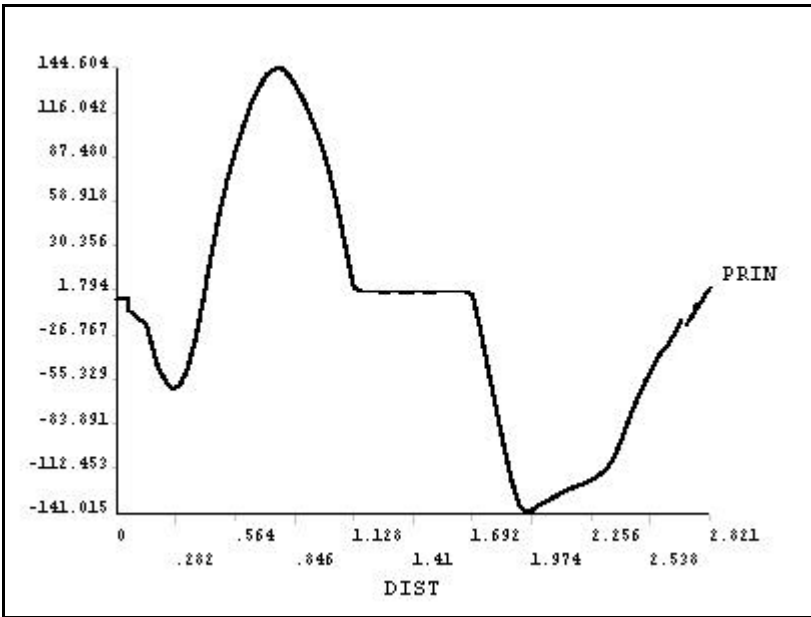


Fig 73: A typical stress Y (nodal-stress) plot along **path A**

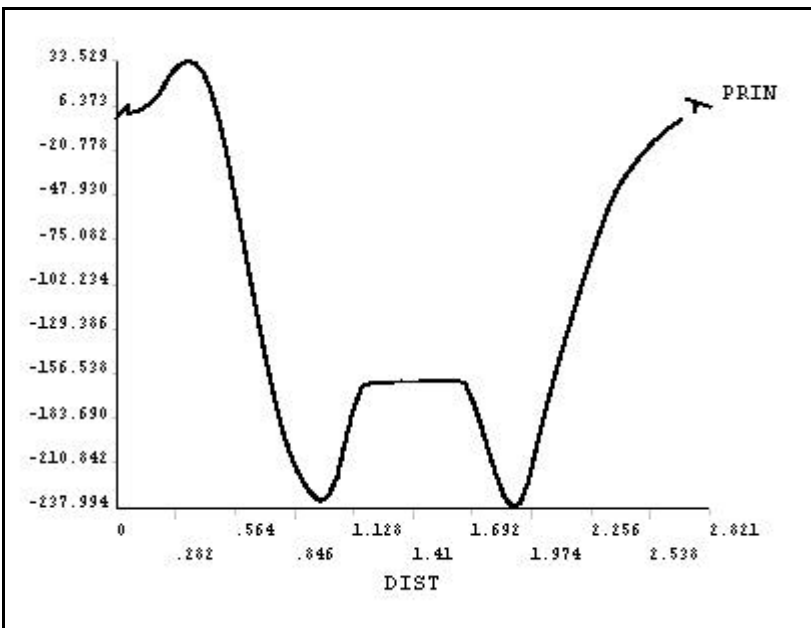


Fig 74: A typical stress XY (nodal-stress) plot along **path A**

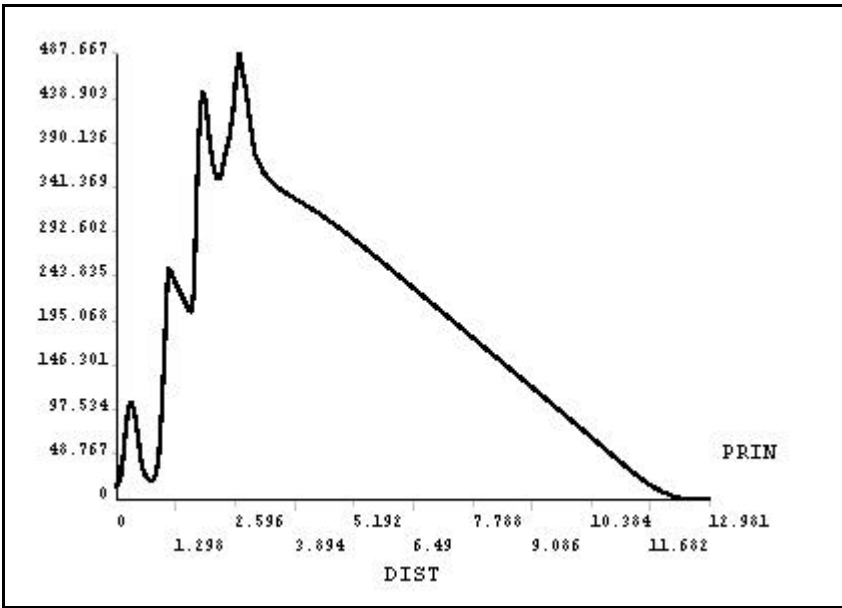


Fig 75: A typical maximum principal stress (nodal-stress) plot along **path B**

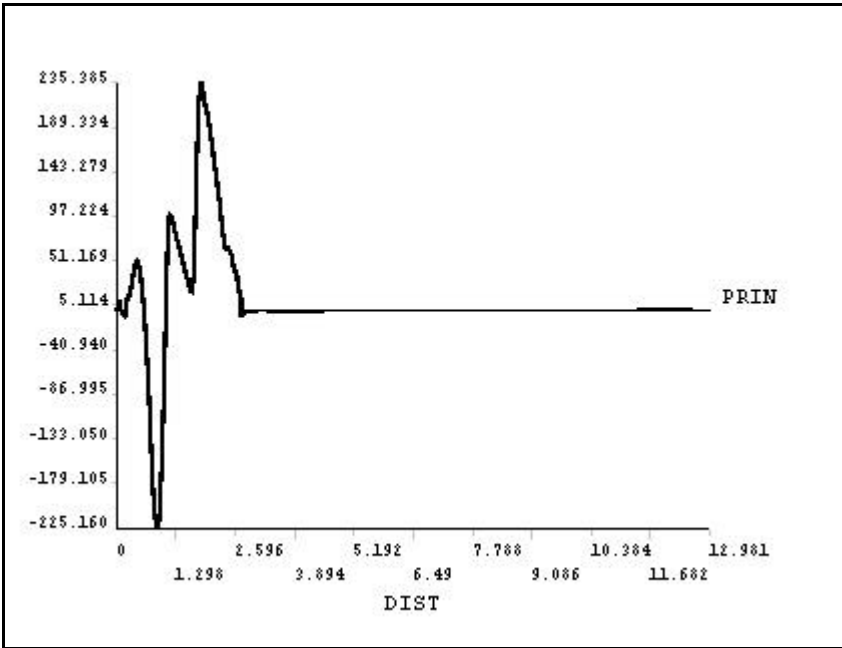


Fig 76: A typical stress X (nodal-stress) plot along **path B**

It can be observed that the maximum principal stress distribution along path B (refer to Fig 75) stretches almost to the end of path B. This can be attributed to stress Y component (refer to Fig 77), which also stretches almost to the end of path B. The existence of this stress Y component is due to the nature of combined loading. In the case of pure bending or pure torsion, such a long-stretching stress Y component does not exist.

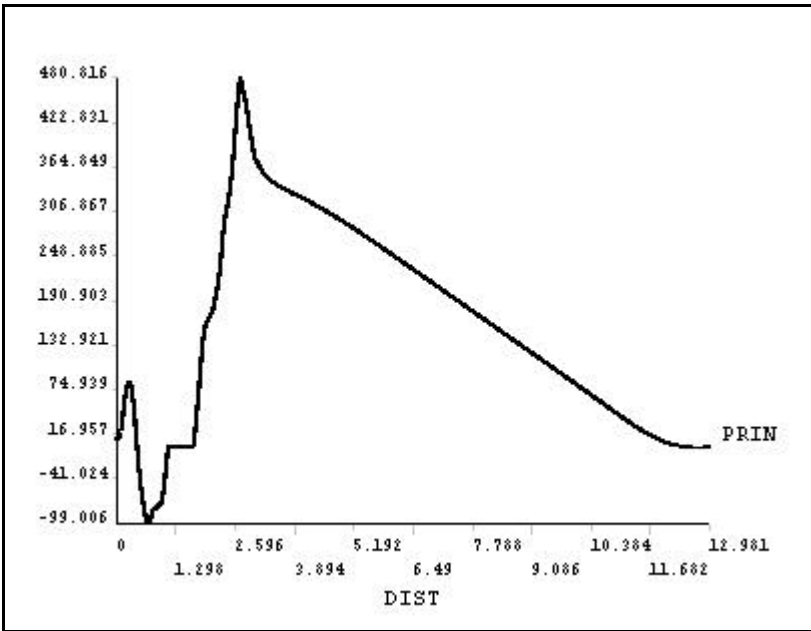


Fig 77: A typical stress Y (nodal-stress) plot along **path B**

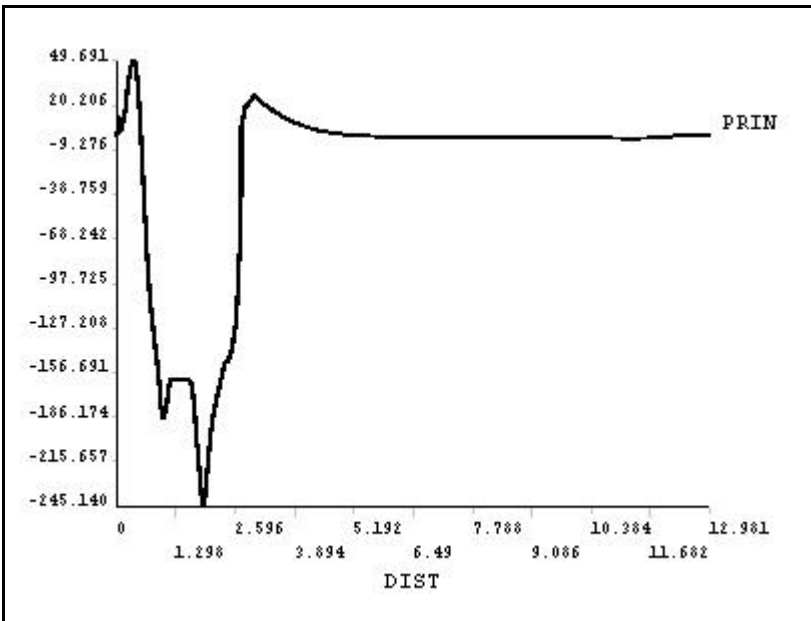


Fig 78: A typical stress XY (nodal-stress) plot along **path B**

6.6.6 Difference between 240um and 300um pure bending

Stress and load factor PDF distribution for path A or B:

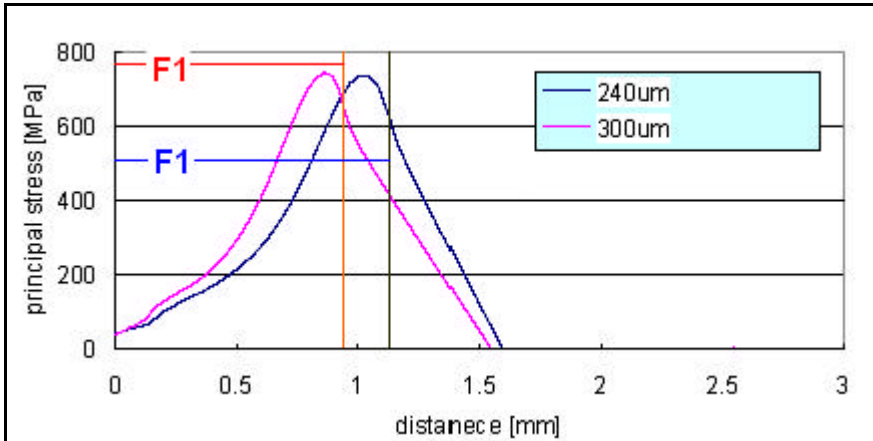


Fig 79: A typical principal **stress distribution** for pure bending (path A or B)

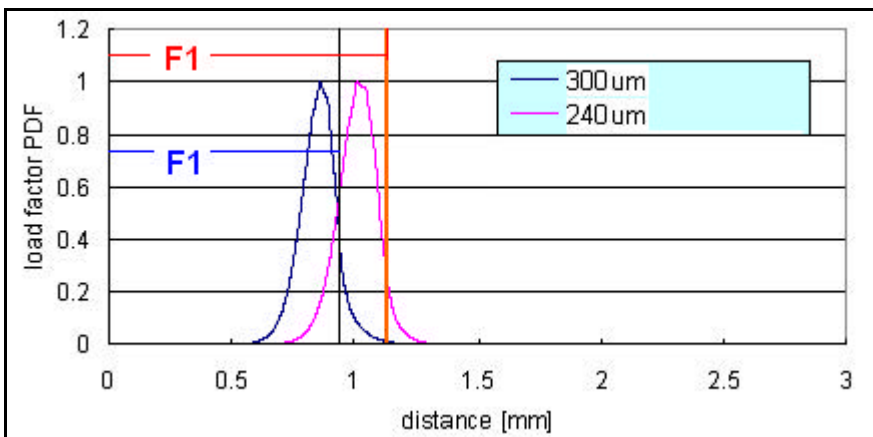


Fig 80: A typical **load factor PDF** for pure bending (path A or B)

Discussion and explanation:

- There is **no statistical difference in strength** between 240um and 300um pure bending samples. The 240um and 300um samples have almost similar strength in pure bending.
- **Path A or B:** From the principal stress distribution and load factor PDF, one can see that there is no noticeable difference.
- **Inferences:** the flaw populations in 240um and 300um in the “severe stress region” are of the same nature (same size and orientation PDF). In other words, on a single piece of wafer, the flaw population in the “severe stress region” on any two specimens could be almost the same.
- **SEM photos:** There seems to be no fractographic evidence to show that there is a difference in flaw between the 240um and 300um samples. **Furthermore, it is postulated that the geometrical difference between 240um and 300um specimen could not possibly lead to a significant difference in etching defects (size and orientation).** Refer to Fig 100 to Fig 117 for a comparison of flaws between 240um and 300um specimens.

6.6.7 Difference between pure bending and combined loading

Stress and load factor PDF distribution for path A:

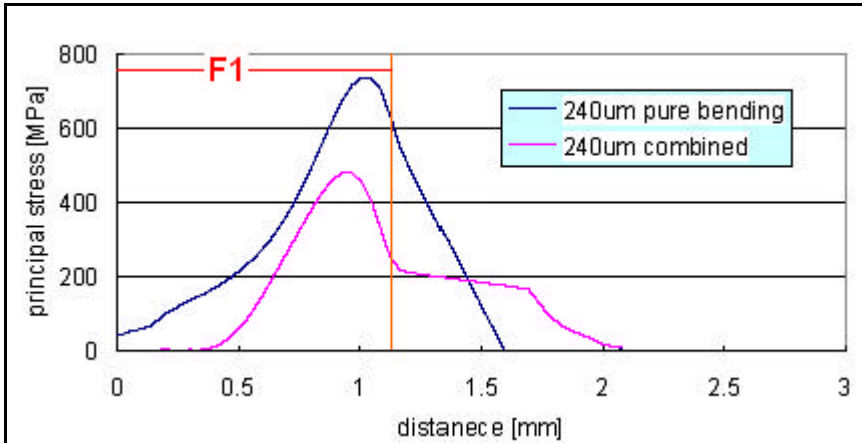


Fig 81: A typical **stress distribution** for 240um pure bending and 240um combined loading (path A)

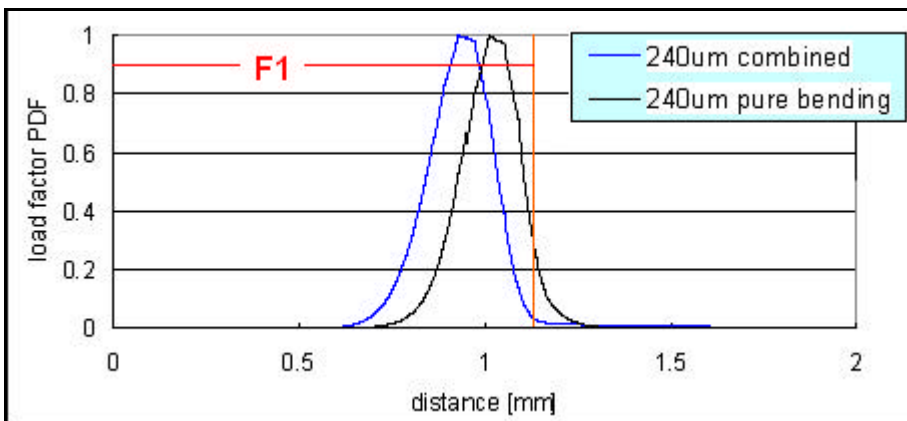


Fig 82: A typical **load factor PDF** for 240um pure bending and 240um combined loading (path A)

Stress and load factor PDF distribution for path B:

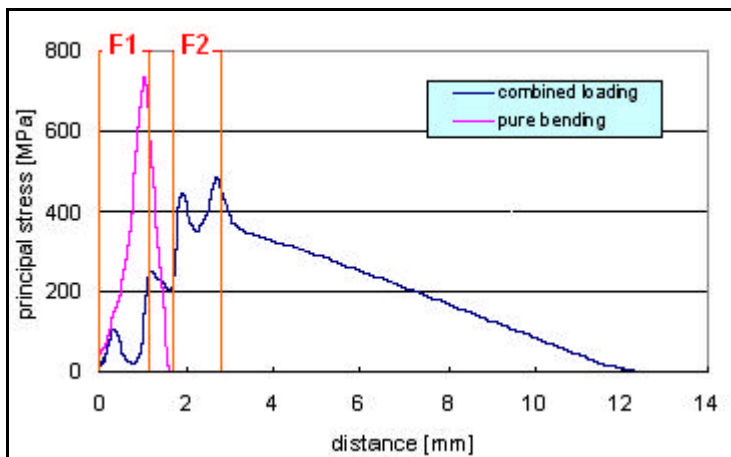


Fig 83: A typical **stress distribution** for 240um pure bending and 240um combined loading (**whole of path B**)

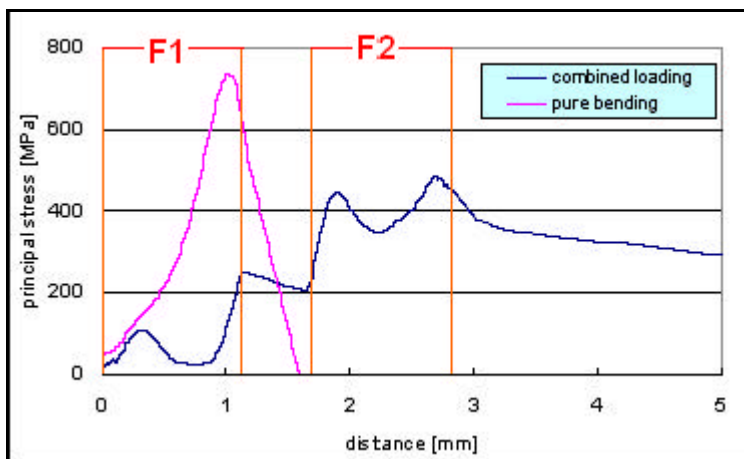


Fig 84: A typical **stress distribution** for 240um pure bending and 240um combined loading (**part of path B**)

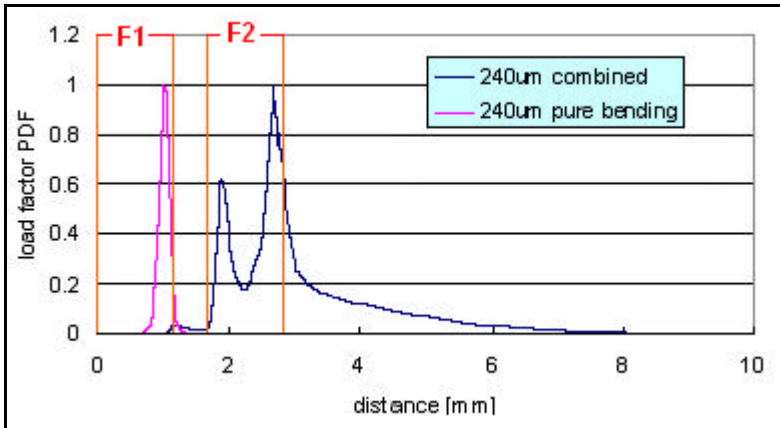


Fig 85: A typical **load factor PDF** for 240um pure bending and 240um combined loading (**whole of path B**)

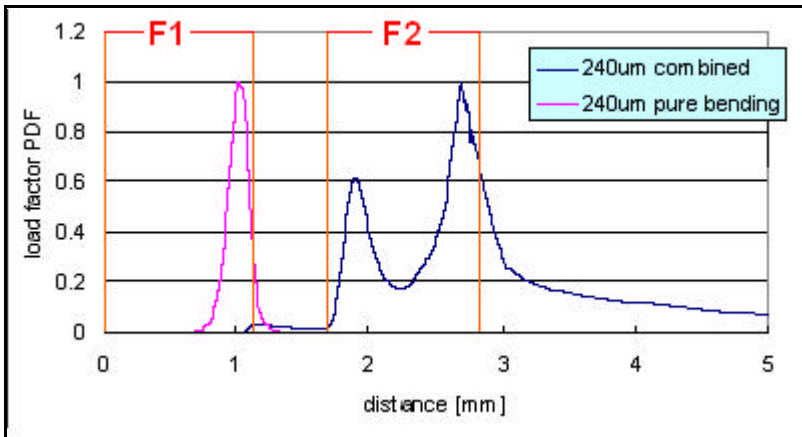


Fig 86: A typical **load factor PDF** for 240um pure bending and 240um combined loading (**part of path B**)

Discussion and explanation:

- There is **significant statistical difference in strength** between pure bending and combined loading samples (non-parametric test).
- **Path A:** From the load factor PDF graph, one can see that the peak of the load factor for the case of 240um combined loading is a little closer to the left side of the graph. The load factor values for both pure bending and combined loading are almost similar.
- **Path B:** From the load factor PDF, one can observe that for the case of pure loading, the load factor PDF is concentrated on the left side of the graph while that for the combined loading is concentrated on the right side. This is due to the nature of combined loading, which results in stress distribution on diagonally opposite edges of the beams. The load factor value for the combined loading in this case is significant greater than that for pure bending.
- **Inferences:** The difference in strength could be attributed to the fact that for the case of 240 combined loading, the maximum principal stress direction is more aligned with the general flaw orientation. Another possible reason for the difference in strength could be attributed to the fact that the combined loading has a much higher overall load factor (considered both path location A and B) than pure bending. As a result, the fracture probability is increased.
- **SEM photos:** It can be observed that the flaws are almost of the same nature in the left or right fillet. Moreover, the flaws are aligned perpendicularly to the beam edge in the fillet region. Refer to Fig 102 to Fig 107 or Fig 110 to Fig 115 for flaws around the fillet region.

6.6.8 Difference between 240um and 300um combined loading

Stress and load factor PDF distribution for path A:

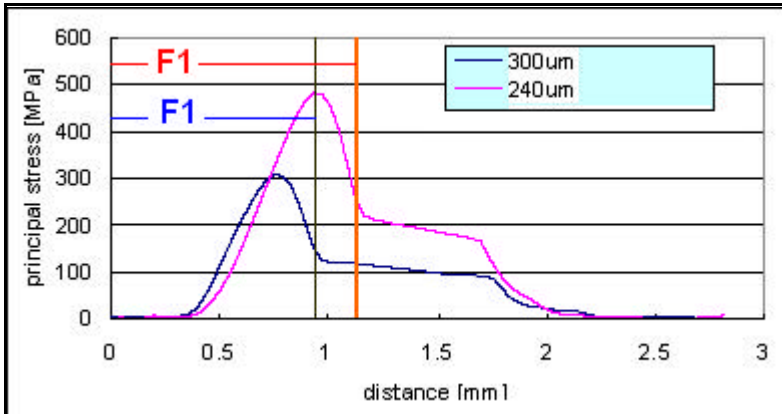


Fig 87: A typical **stress distribution** for 240um and 300um combined loading (path A)

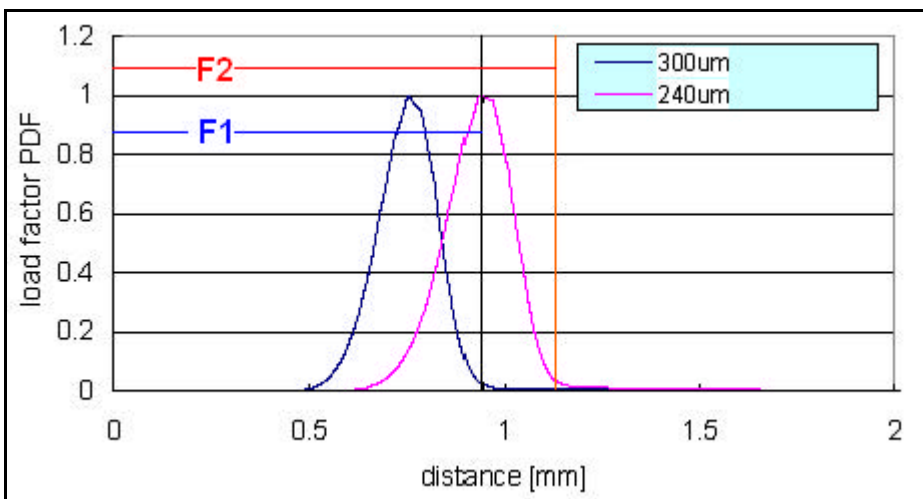


Fig 88: A typical **load factor PDF** for 240um and 300um combined loading (path A)

Stress and load factor PDF distribution for path B:

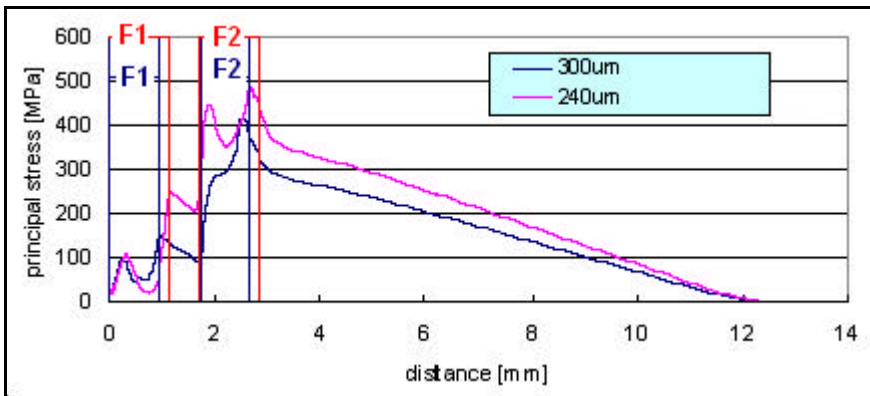


Fig 89: A typical **stress distribution** for 240um and 300um combined loading (whole of path B)

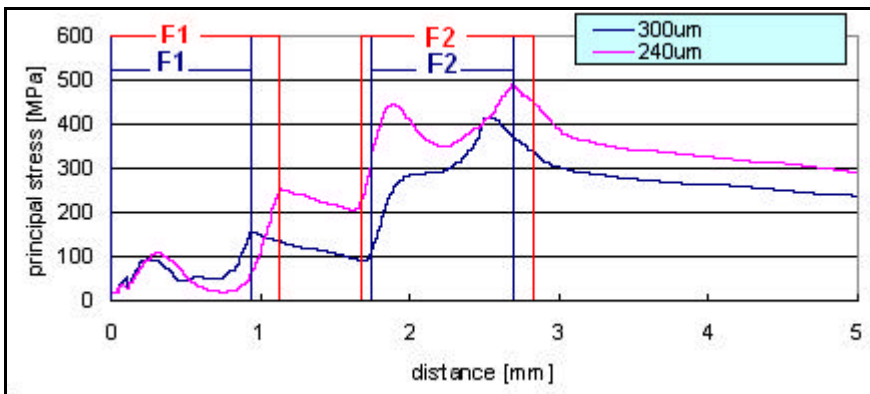


Fig 90: A typical **stress distribution** for 240um and 300um combined loading (part of path B)

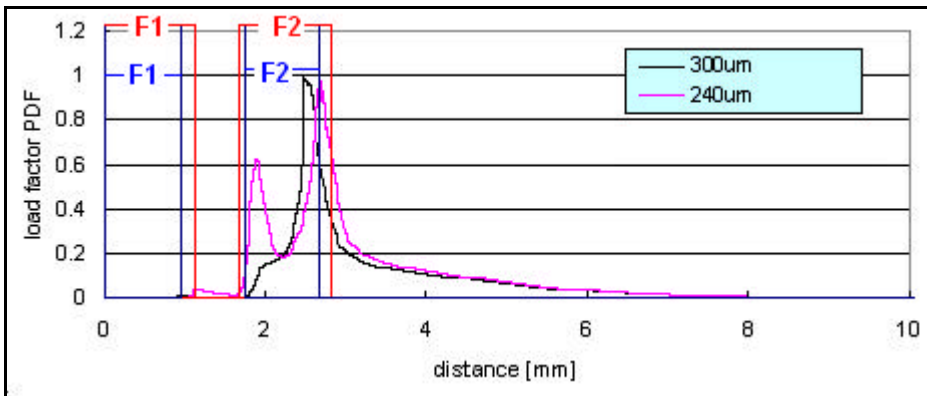


Fig 91: A typical **load factor PDF** for 240um and 300um combined loading (**whole of path B**)

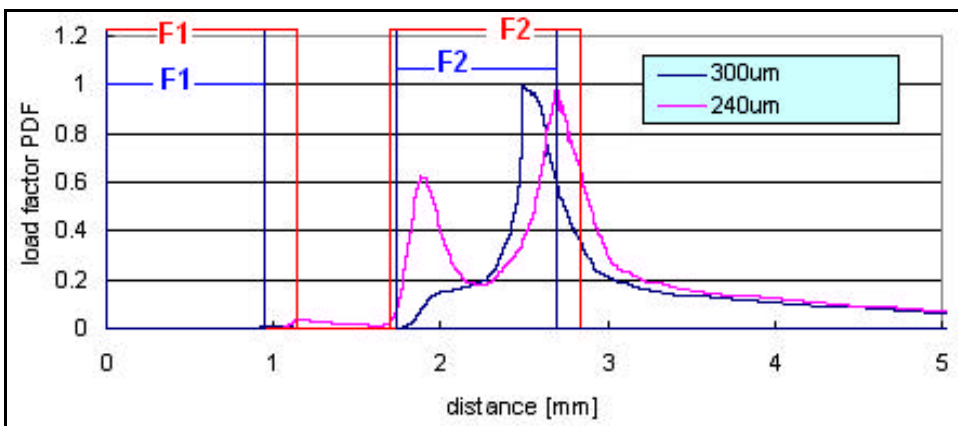


Fig 92: A typical **load factor PDF** for 240um and 300um combined loading (**part of path B**)

Discussion and explanation:

- There is **significant statistical difference in strength** between the 240um and 300um combined loading samples (non-parametric test).
- **Path A:** From the stress and load factor PDF graphs, one can observe that there are no noticeable differences. Moreover, the load factor value for both 240um and 300um combined loading are similar, with 240um being only slight higher.
- **Path B:** From the stress and load factor PDF graphs, one can observe that there are noticeable differences. Moreover, the load factor value for both 240um is much higher than that for 300um.
- **Inferences:** Despite the fact that the overall load factor for the 240um sample is larger than that for the 300um sample, the 300um sample failed at a lower fracture stress. This could be explained by the fact that the geometrical difference between the 240um and 300um sample has resulted in the 300um sample's maximum principal stress direction being more favorably orientated in the general flaw direction. **This in turn could imply that flaw orientation is very important in determining the strength of the specimen.**
- **SEM photos:** Refer to Fig 102 to Fig 107 or Fig 110 to Fig 115 for flaws around the fillet region.

6.7 Fractography

6.7.1 Scaling issues in fractography

It is a universal feature of fractography that there is detail at all magnifications, down to the atomic level. This raises the question as to the magnification at which the surface is to be examined. The answer depends on many different factors and in particular, on the purposes of the examination and the type of information required. A key issue is the scale of observation in relation to the scale of the microstructure. Fractographic observations are made over a very wide range, from $10^{-10}m$ to $1m$ and beyond. The individual techniques have a limited range of applicability and there may be problems in reconciling features observed with different techniques at the same magnification. The microstructural dimension is a characteristic of the material. In many materials, there are several levels of structural organization and a hierarchy of microstructural dimensions. The dimension relevant to a particular fractographic dimension depends on the nature of the problem being studied.

The roughness of fracture surfaces, apparent at all scales of observation, makes it particularly difficult to describe the topography of these surfaces either qualitatively or in mathematical terms. The problem is common to many phenomena, particularly in the complex patterns of nature. These patterns appear random and chaotic and yet they exhibit some evidence of internal consistency. Here, "fractal" can be used to describe these irregular and fragmented features. The application of the fractal approach has been possible because of the development of powerful image analysis equipment and computer software. Although there are many limitations to the use of fractal geometry in fractography, the underlying concepts provide a valuable tool for understanding some aspects of the subject. Attempts have been made to correlate the fractal parameters of fracture phenomena with the engineering performance of materials. In fractal geometry, the relation between $L(r)$ (length of measurement) and r (unit length of measurement) is a measure of the roughness. It should be noted that there is a strong statistical factor in the determination of $L(r)$. The fractal dimension is obtained by plotting $\log L(r)$ against $\log r$. If the plot is linear, the relationship between $L(r)$ and r may be written as:

$$\boxed{L(r) = Ar^{-(D-1)}} \quad \text{-----(65)}$$

where A is a constant and the slope of $\log L(r)$ versus $\log r$ is $(1-D)$. D is the fractal dimension. It has a value between one and two. If $\log L(r)$ versus $\log r$ is linear, the following properties of the roughness apply:

- The roughness profile exhibits self-similarity. This means that, on a statistical basis, the profile appears the same at all magnifications. With

self-similarity established, one has a powerful tool to describe the length of the profile at any magnification.

- The degree of roughness increases as D increases. $D=1$ for a straight line profile.
- For a fully fractal profile, the length of the line extends without limit. As r approaches zero, $L(r)$ approaches infinity. It follows that the length of the profile is infinite. Clearly, this does not apply to real fracture surfaces. There is an upper limit set to r by the overall dimensions of the fracture surface and there is a lower limit set by atomic dimensions.

There are many aspects of scaling concerned with the dimensions of microstructure in relation to features of the stress fields in a material or component before it fails. The important factor here is not the absolute dimensions of the specimen or the microstructure but their relative values. In other words, the deformation and fracture behaviors of the solid depend on the relative values of dimensions and not absolute values. In materials with a hierarchy of microstructural dimensions, there are some dimensions that are sensitive to the dimensions of the stress field and others that are not.

In this research, the entire fractured surface was first examined at a high magnification (approximately 300 to 400 times). Characteristics of brittle fractured surfaces were confirmed. Next, magnification was increased to about 5000 to 10,000 times to locate the flaws. At a magnification of about 10,000 times, each individual major flaw could be observed and thus the approximate general size and orientation of the flaw could be determined.

6.7.2 Typical size of flaw and estimation of nominal fracture stress

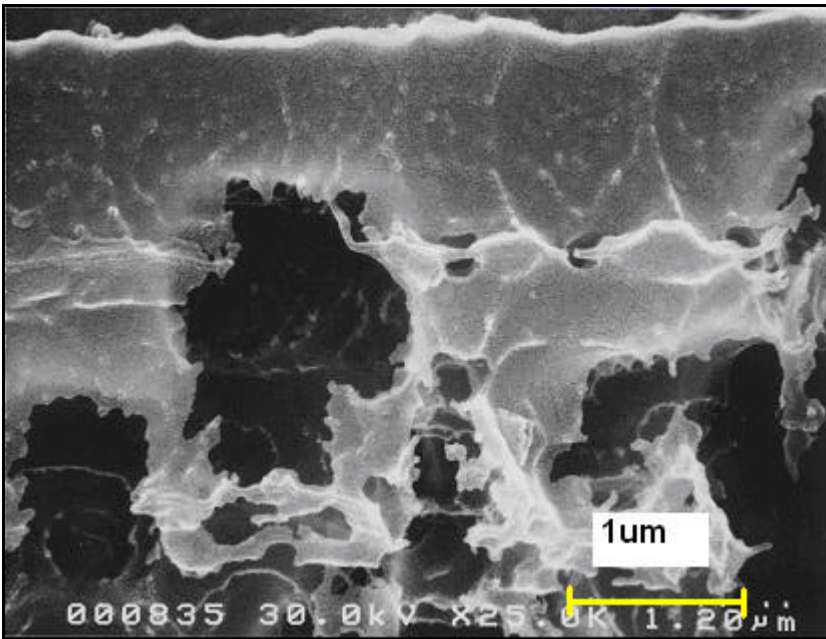


Fig 93: A typical flaw in the region of 1μm in the beam

Using linear-elastic fracture mechanics (LEFM), the severity of a crack in a component can be characterized by the value of a special variable called the stress intensity factor shown below in equation (66):

$$K = FS\sqrt{pa} \quad \text{-----(66)}$$

where S is nominal global stress and a is crack length, both consistently defined relative to the dimensionless quantity F . Use of K depends on the behavior being dominated by linear-elastic deformation, so that the zone of yielding (plasticity) at the crack tip must be relatively small. Simple equations and handbooks provide values of F for a wide range of cases of cracked bodies. The value of F depends on the crack and member geometry, the loading configuration, such as tension or torsion, and on the ratio of the crack to the width of the member. Some notable values of F for relatively short cracks under tension stress are as follows (equation (67):

$$\begin{aligned} F &= 1.00 \text{ (center - cracked plate)} \\ F &= 1.12 \text{ (through - thickness surface crack)} \\ F &= 0.73 \text{ (half - circular surface crack)} \end{aligned} \quad \text{-----(67)}$$

The value of K where a given material begins to crack significantly is called K_o , and where it fails K_c . Slow-stable crack growth may follow K_o until K_c is

reached, and both of these may decrease with increased member thickness. If the plastic zone surrounding the crack tip is quite small compared to the thickness and is very well isolated relative to the boundaries of the member, then a state of plain strain is established. Under plane strain, only limited slow-stable crack growth occurs, so that K_Q and K_C have similar values to each other and also to the standard plane strain fracture toughness, K_{IC} . A value of K_{IC} thus represents a worst-case fracture toughness that can be safely used for any thickness.

Values of K_{IC} for a given material generally decrease along with ductility if the material is processed to achieve higher strength. For a given material and processing, K_{IC} generally increases with temperatures, sometimes exhibiting a rather abrupt change over a narrow range of temperatures, and also having relatively constant lower shelf and upper shelf values on opposite sides of the temperature transition. Increased loading rate causes K_{IC} to decrease, having the effect of shifting the transition to higher temperature. The microstructure of the material may affect K_{IC} , as in the detrimental effect of sulfur in some steels, the effect of crystal grain orientation from rolling of aluminum alloys, and radiation embrittlement of pressure vessel steels.

If the plastic zone is too large, LEFM is no longer valid. Modest amounts of yielding can be handled by using adjusted values of K_{IC} calculated by adding half of the plastic zone size to the crack length. However, above about 80% of the fully plastic load or moment, more general methods such as the J-integral or the crack-tip opening displacement (CTOD) are needed.

In this research, the application of LEFM was assumed valid. K_{IC} of silicon approximated as $1 \text{ MPam}^{1/2}$ ¹¹. F is taken to be 1 and a to be 1 μm (typical size of a flaw). This gives a nominal stress of about 560 MPa. This is in good agreement (same order) with the fractured stress estimated from FEM analysis.

6.7.3 Pure bending fractured surface

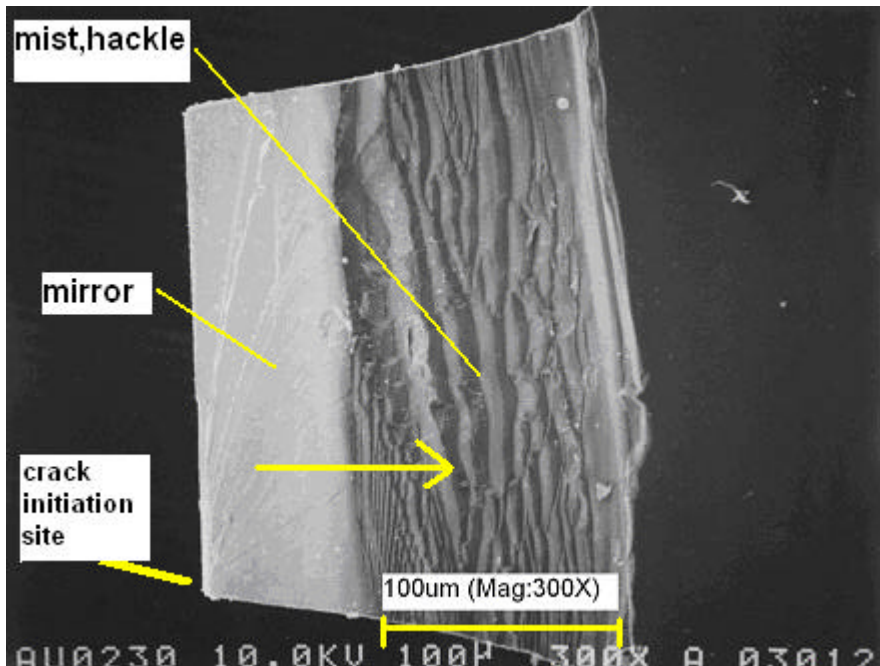


Fig 94: A typical fractured surface for pure bending (note the crack initiation site, mirror, hackle regions; the arrow head points in the direction of crack propagation)

The fractography of “mirror”, “mist” and “hackle” provides a powerful tool in the study of a number of important fracture problems even though the associated phenomena raise some fundamental, and still to be understood, aspects of fracture dynamics. These features can be explained in a qualitative way. When a flaw or crack is present, there is stress concentration close to the crack tip. At a critical applied stress, the Griffith condition is satisfied and the crack starts to propagate. Under constant loading conditions, an increase in crack length means that fracture is unstable and excess energy is available to drive the crack. In terms of fracture toughness parameters, once $K = K_{IC}$, further crack growth results in K becoming much larger than K_{IC} . Under these conditions, the crack accelerates very rapidly; the rate of energy release also increases rapidly, as does the stress intensity at the tip of the moving crack, usually referred to as the dynamic stress intensity K_d . The higher stresses and greater energy released produce greater micro-mechanical activity at the crack tip and a progressive increase in the roughest of the fracture surface, which has the features of mirror, mist and hackle.

Hence, from the examination of mirror, mist and hackle configurations, one can make a good inference about the crack propagation direction, which in this case is from left to right in the Fig 94.

6.7.4 Combined loading fractured surface



Fig 95: A typical fractured surface for combined loading (note the undulating surfaces and river patterns)

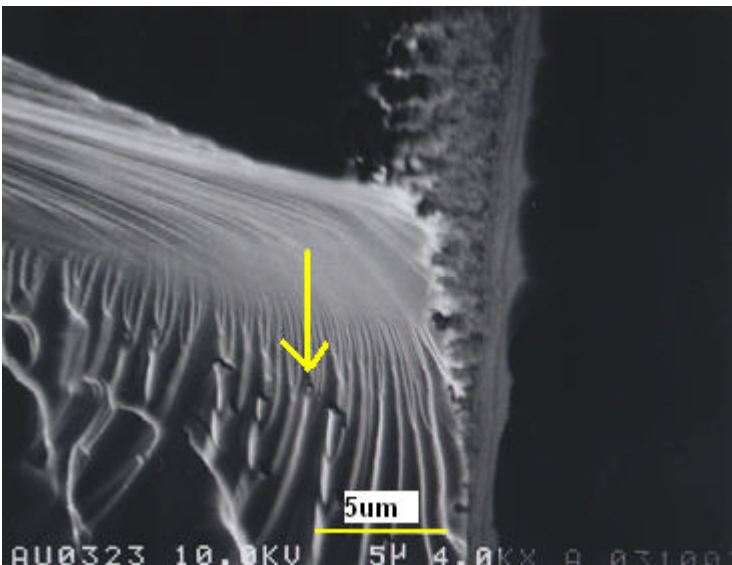


Fig 96: Evident river patterns (the arrow head points in the direction of crack propagation)

The loading mode has a strong influence on the micro-deformation and fracture processes at the crack tip. In the case of pure bending, both the loading mode and crack propagation are predominately Mode I. In the case of combined loading, the loading mode is a combination of Mode I, Mode II and Mode III, judging from the configuration of the etching defects. The relationship between Mode II and Mode III loading and crack growth is more complicated. As these loading conditions do not generate any crack opening, it is difficult to envisage crack growth in brittle materials without some Mode I loading. Although the actual growth of cracks in

brittle materials in pure Mode II and pure Mode III loading is open to conjecture, it is absolutely clear that the combination of these loading modes, with Mode I loading, influences crack propagation.

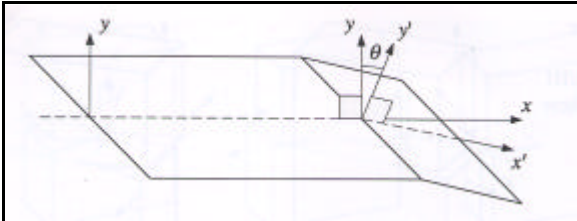


Fig 97: Crack tilting: Mixed Mode I/II.

Crack Tilting (Fig 97): The simplest case of mixed-mode loading is the combination of Mode I and Mode II. Under these conditions, the maximum tensile stress acts at an angle θ between 0° and 90° to the plane of crack. The growing crack tends to tilt about the line of crack front so that the plane of the crack is normal to the maximum tensile stress.

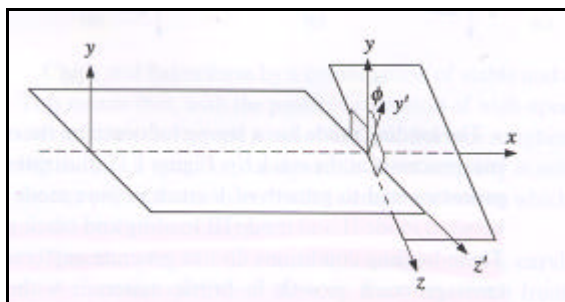


Fig 98: Crack tilting: Mixed Mode I/III

Crack twisting (Fig 98): In mixed Mode I/III loading, the maximum tensile stress acts at an angle ϕ between 0° and 90° . The crack tends to twist.

An important point here is that the straight-fronted crack in Fig 97 can move to the new tilted surface simultaneously along the whole of the crack front. In contrast, it is impossible for the crack in Fig 98 to move to the new surface with producing a step on the surface. In other words, a smooth continuously expanding crack can tilt but it cannot twist. Hence, a smooth curving crack surface could be the result of Mode I/II loading and a stepped surface could be the result of Mode I/III loading. Furthermore, the occurrence of river patterns is often as a diagnostic tool to identify the presence of Mode I/III conditions during crack growth.

In this research, for the fractured surfaces of combined loading, there was fractographic evidence (river patterns) pointing to the existence of mixed mode I/III crack propagation. Also, since the fractured surfaces also showed undulating patterns, there could be mixed mode I/II crack propagation.

6.7.5 Flaws in the various regions of the beam

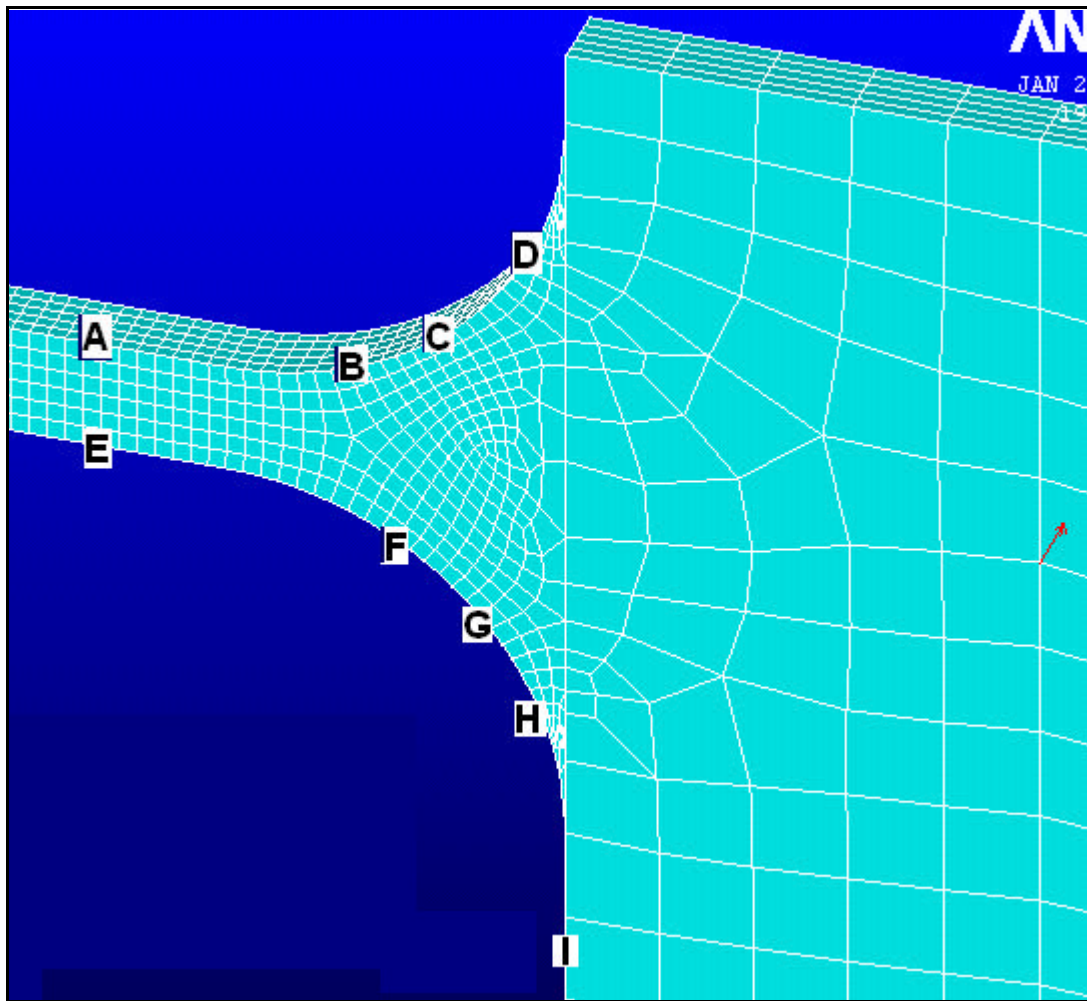


Fig 99: Flaws in the various locations of the beam, namely A, B, C, D, E, F, G, H,

I

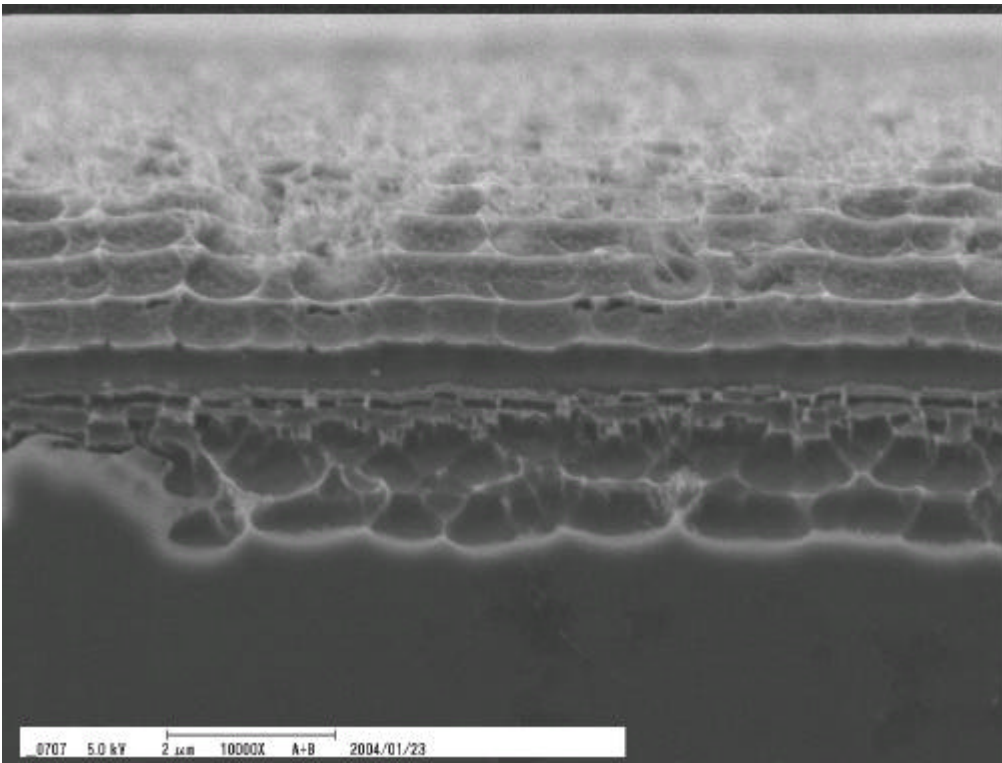


Fig 100: 240um location A

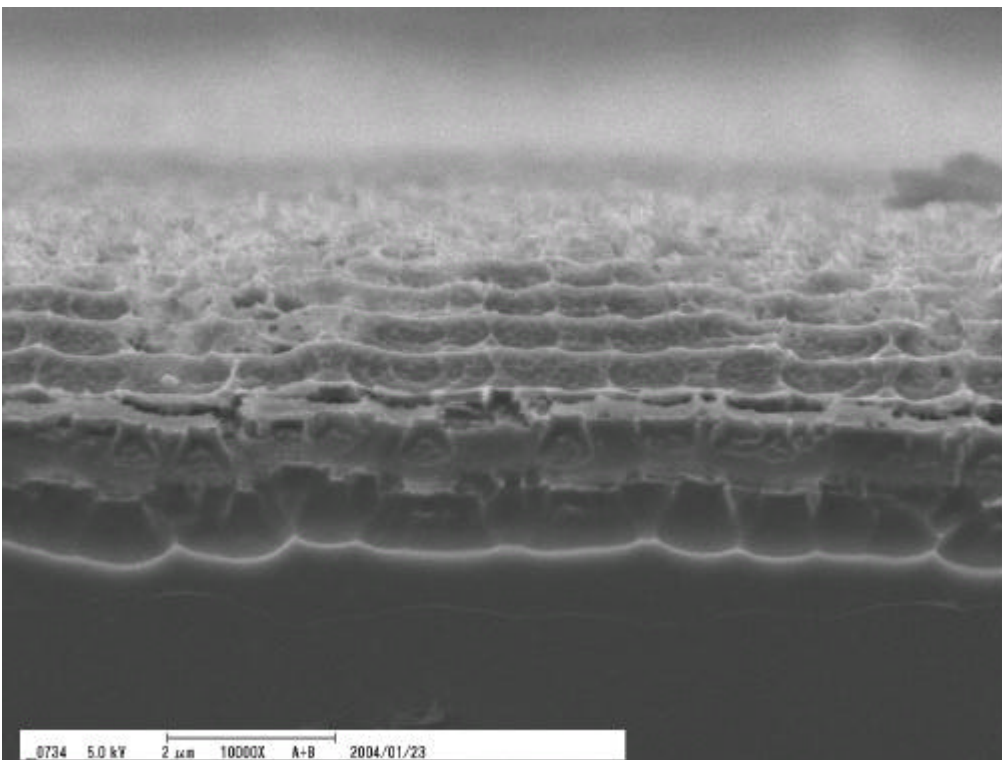


Fig 101: 300um location A

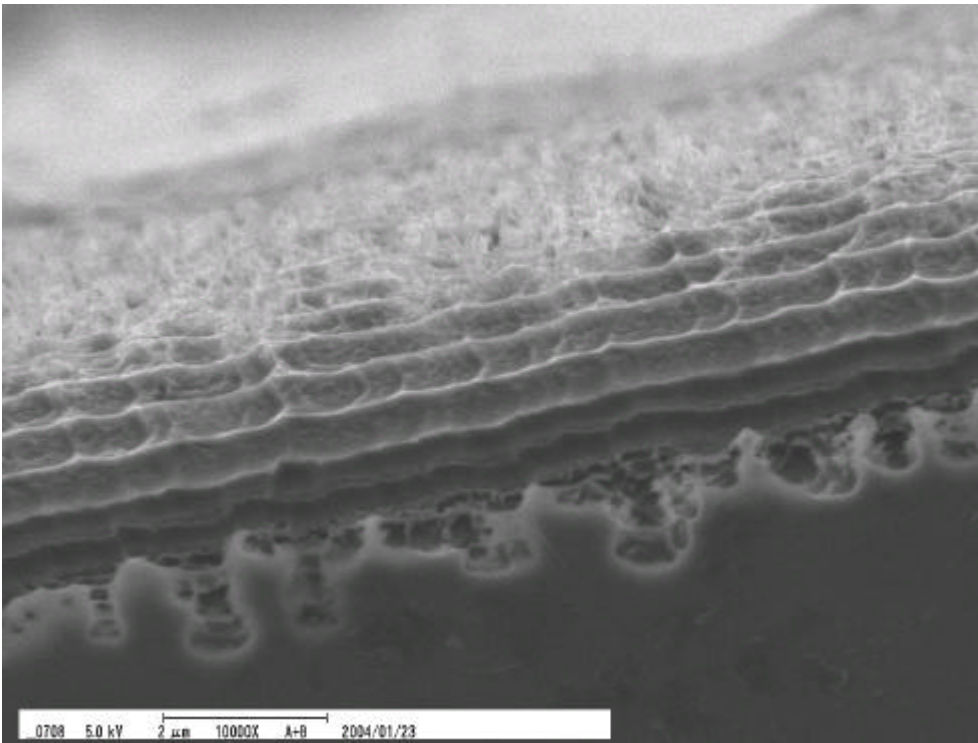


Fig 102: 240um location B

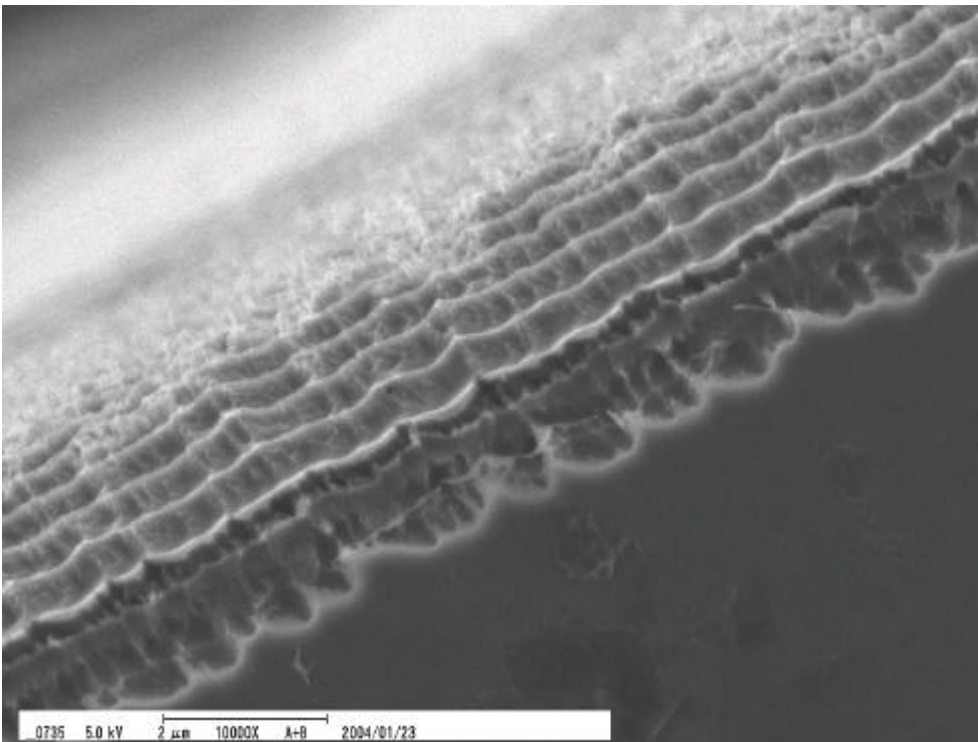


Fig 103: 300um location B

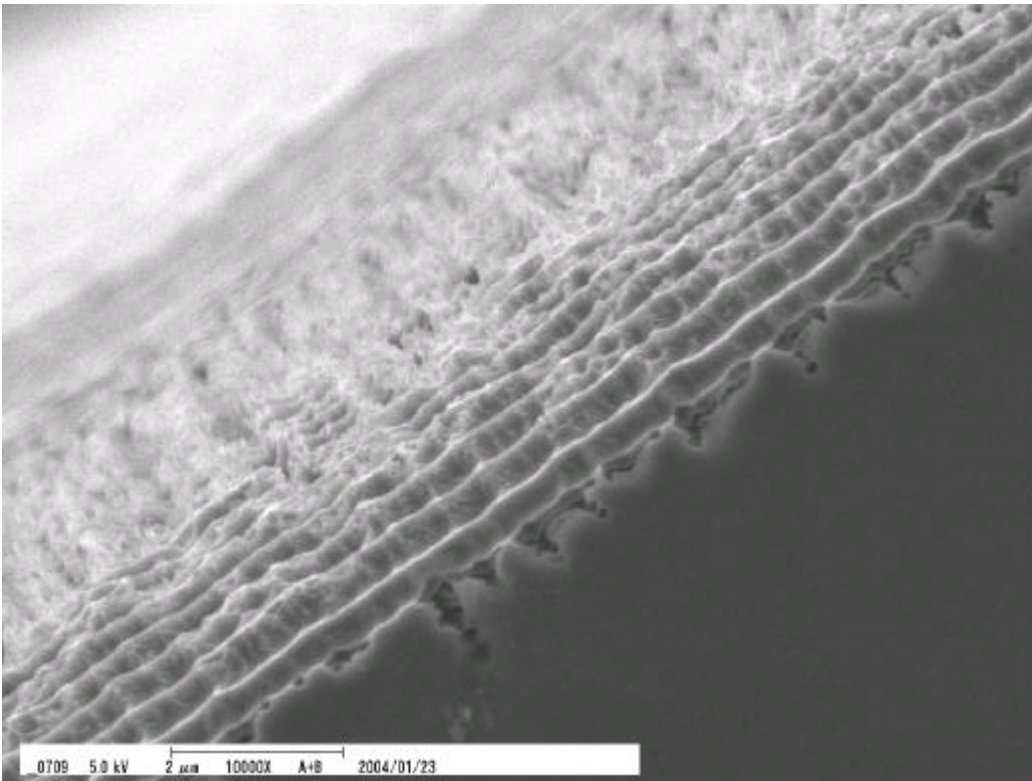


Fig 104: 240um location C

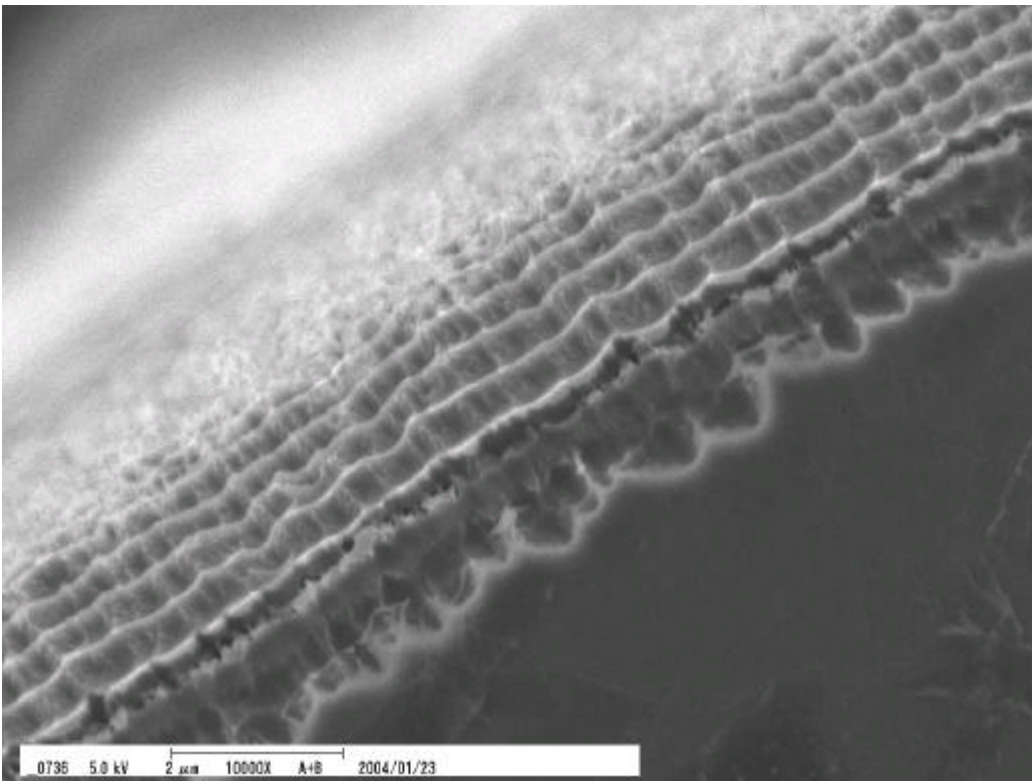


Fig 105: 300um location C

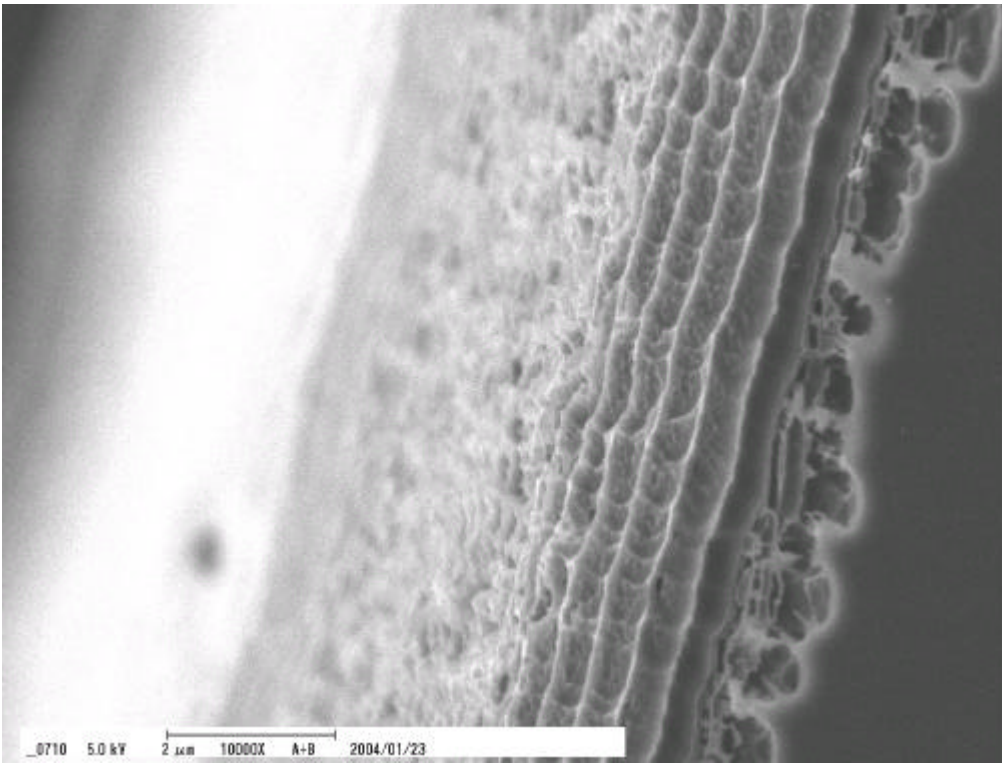


Fig 106: 240um location D

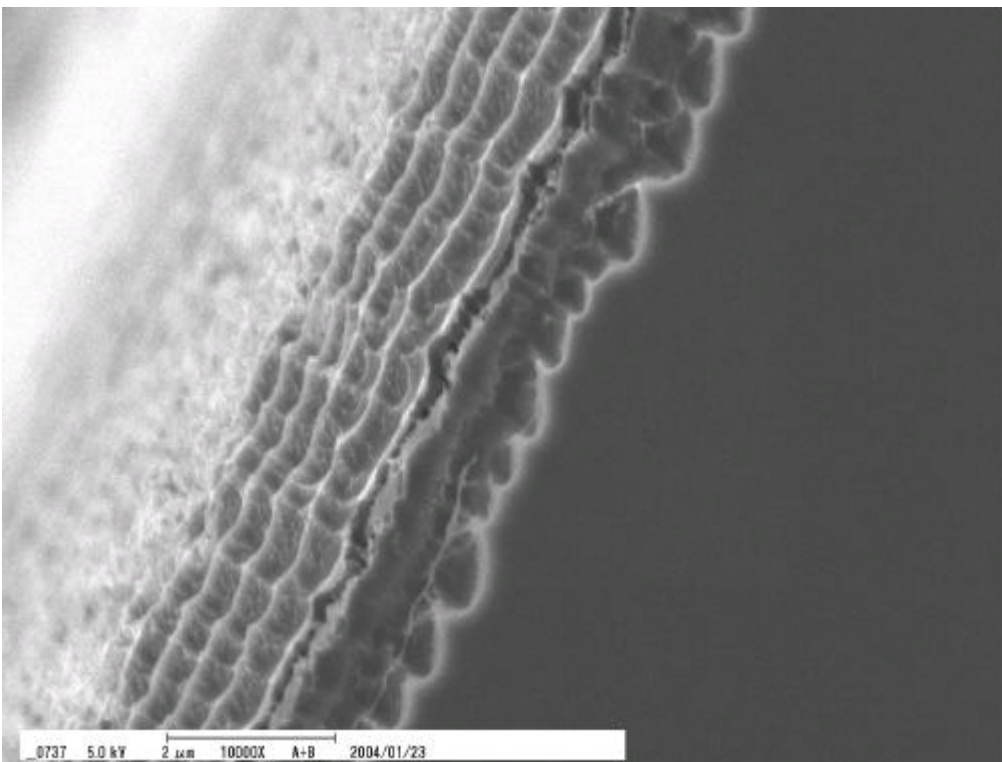


Fig 107: 300um location D

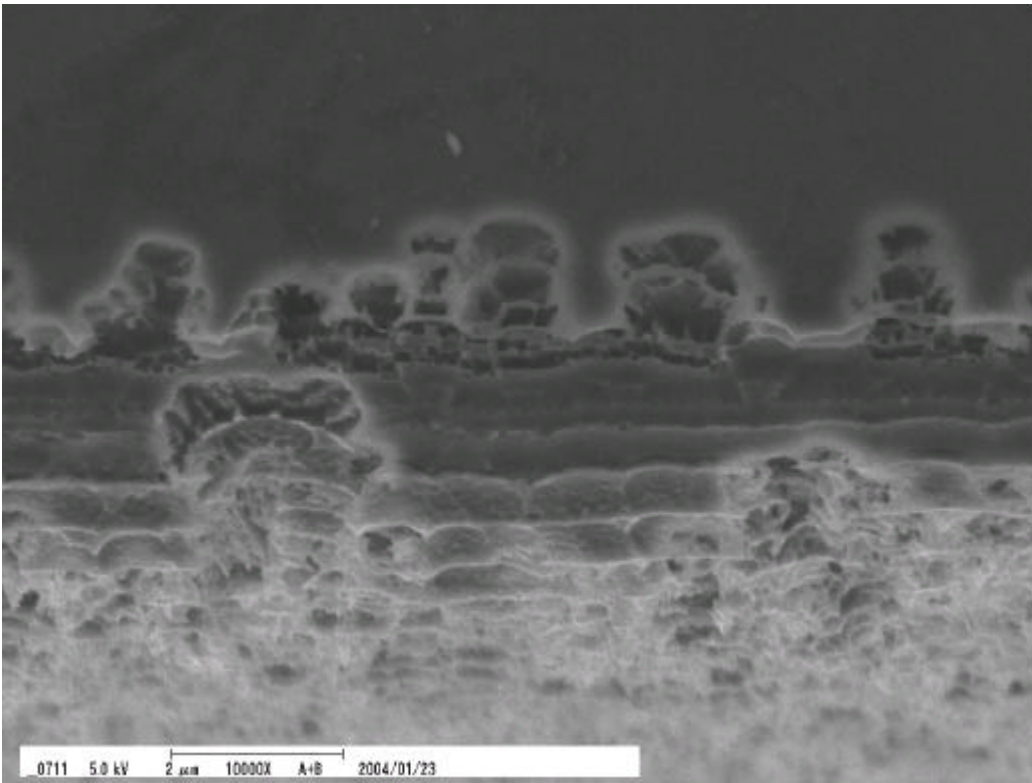


Fig 108: 240um location E

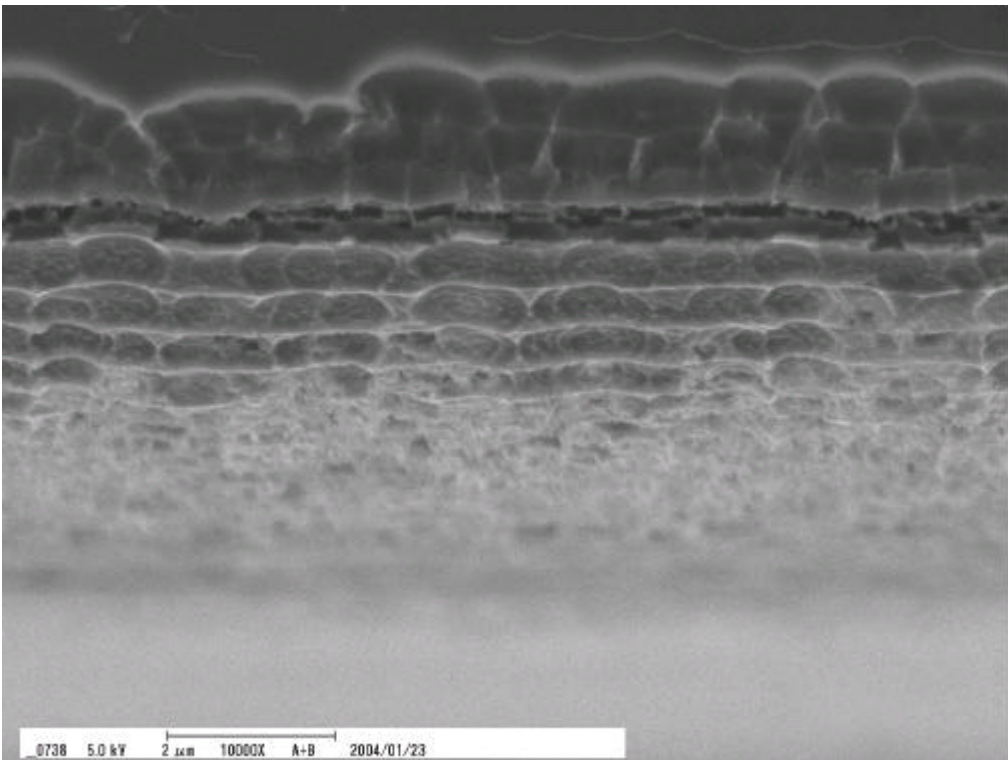


Fig 109: 300um location E

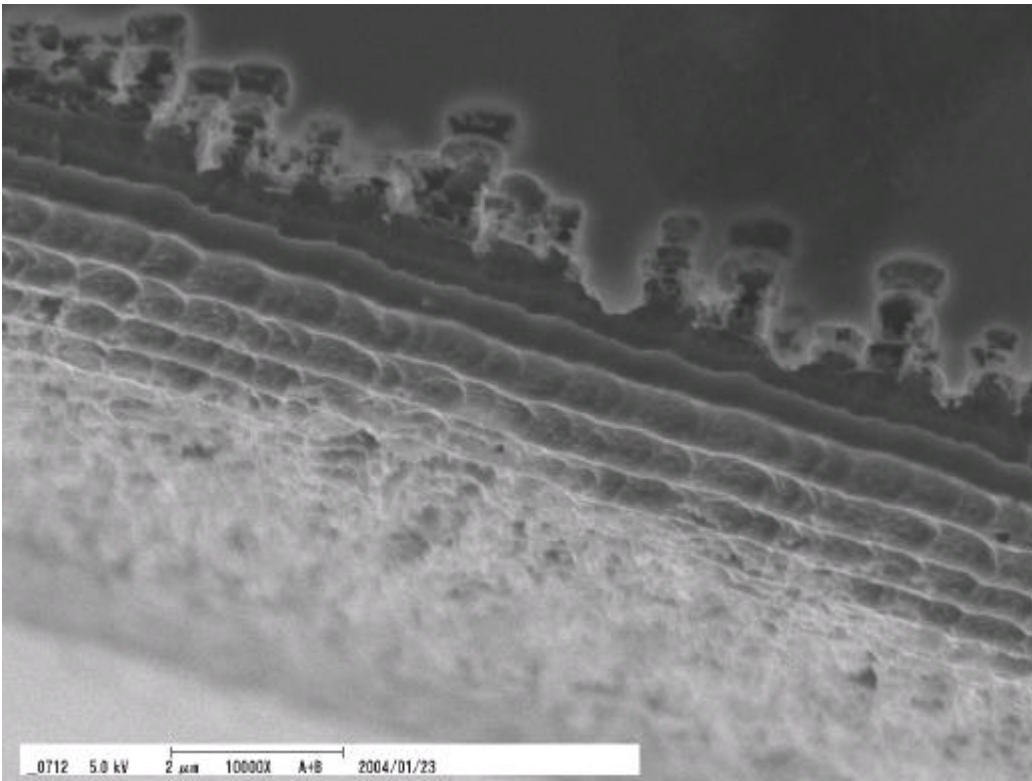


Fig 110: 240um location F

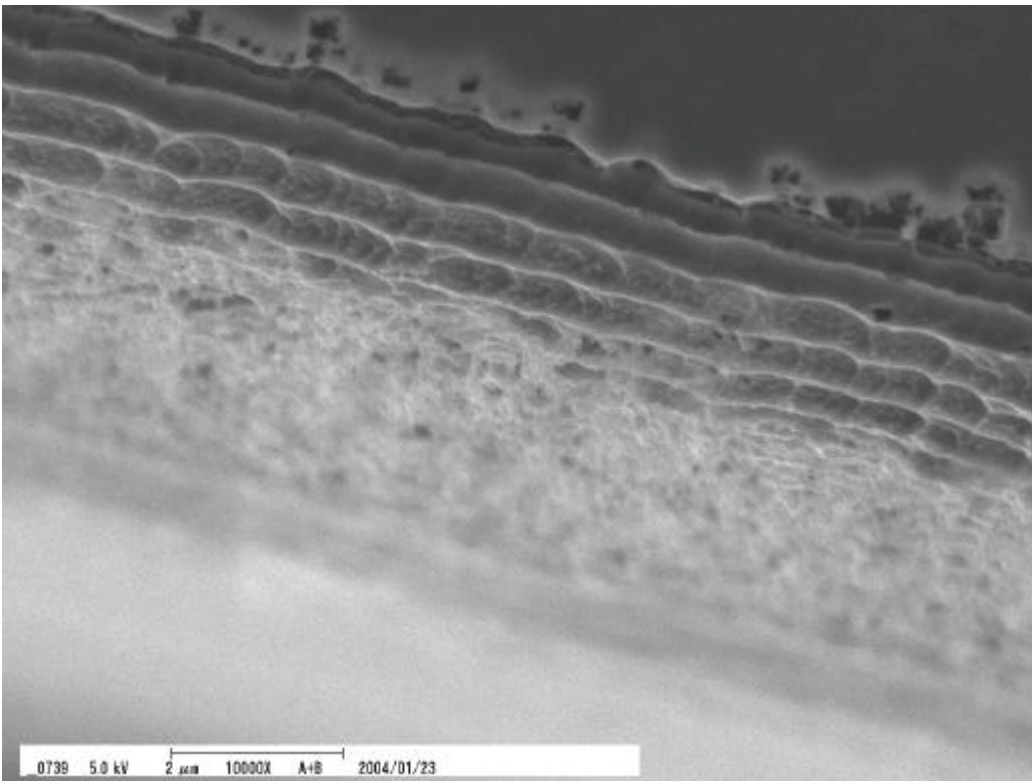


Fig 111: 300um location F

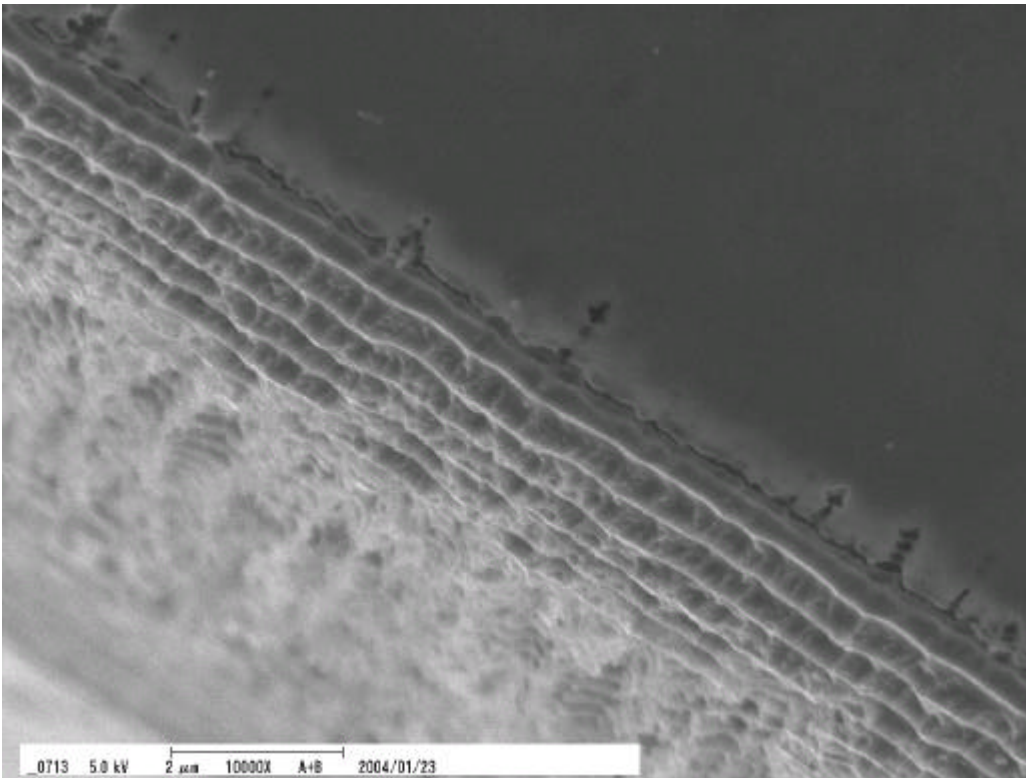


Fig 112: 240um location G

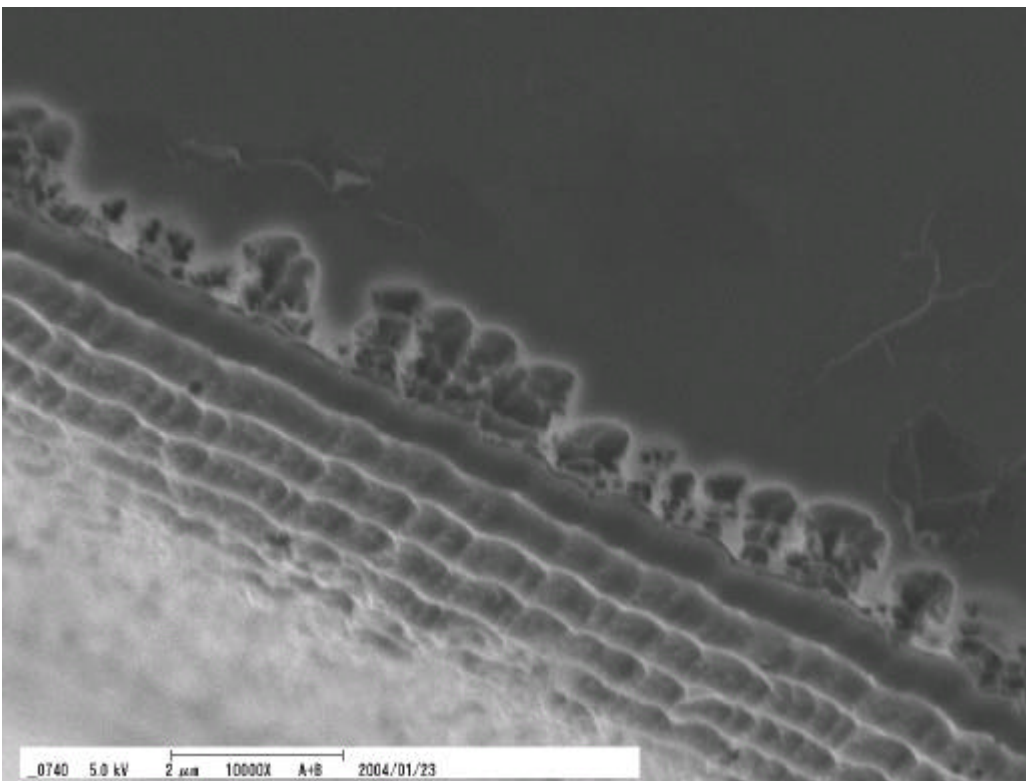


Fig 113: 300um location G

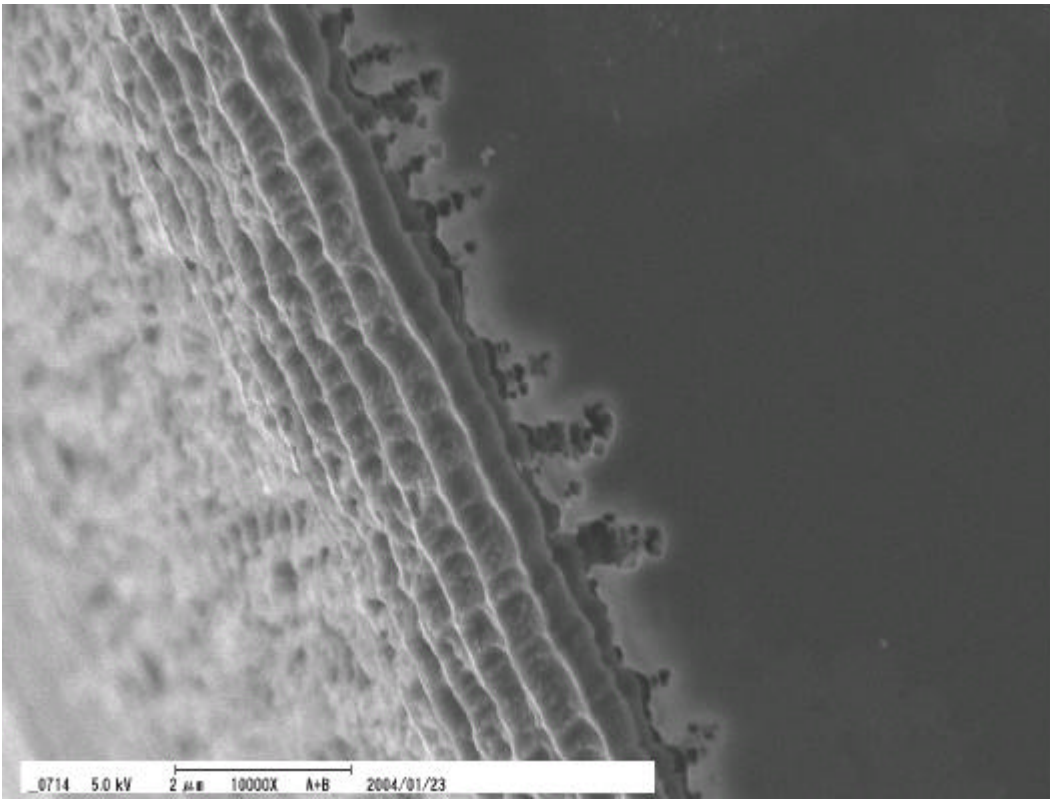


Fig 114: 240um location H

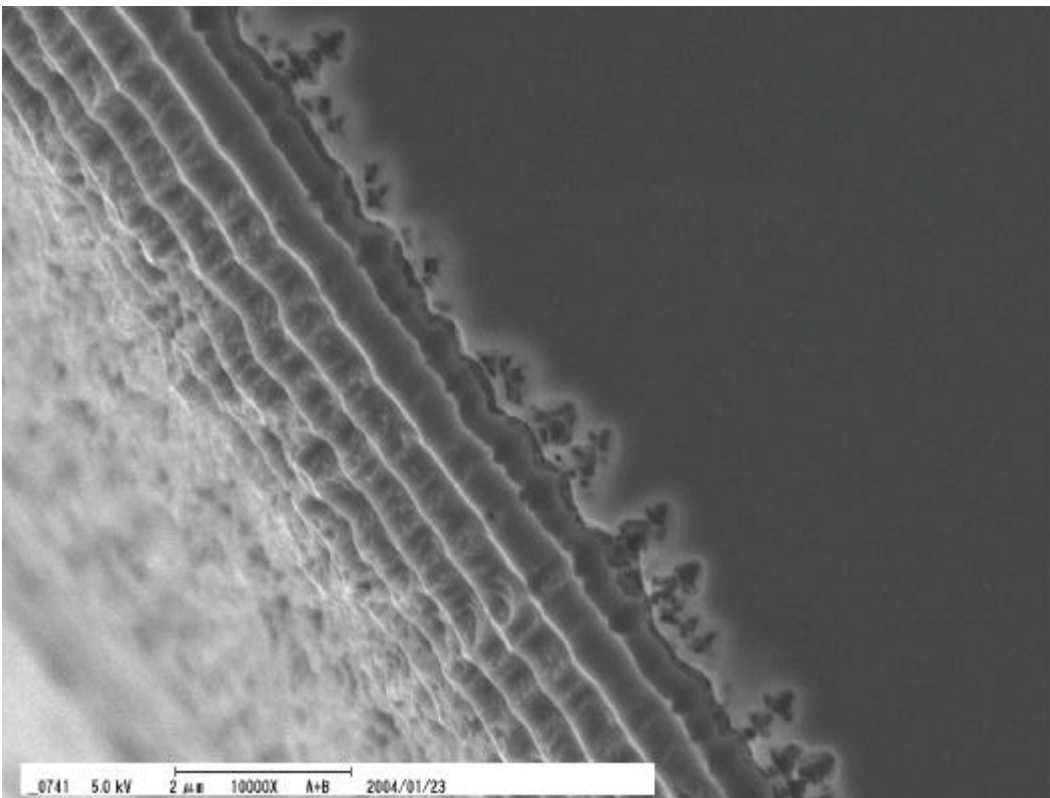


Fig 115: 300um location H

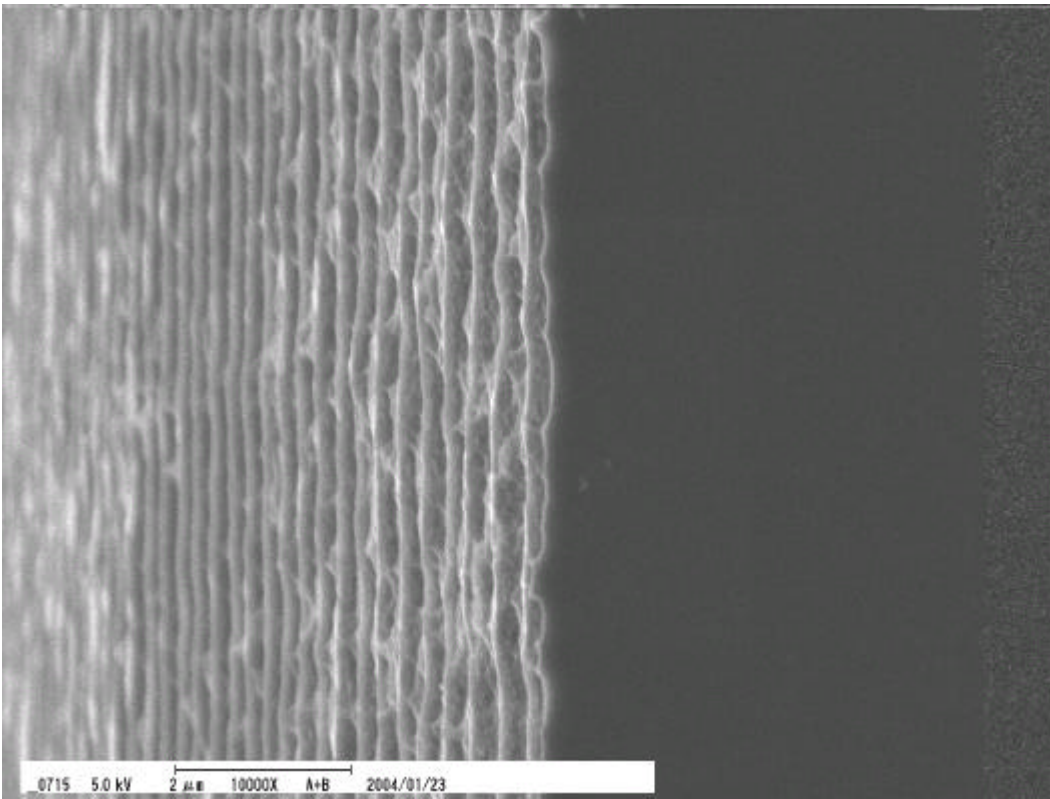


Fig 116: 240um location I

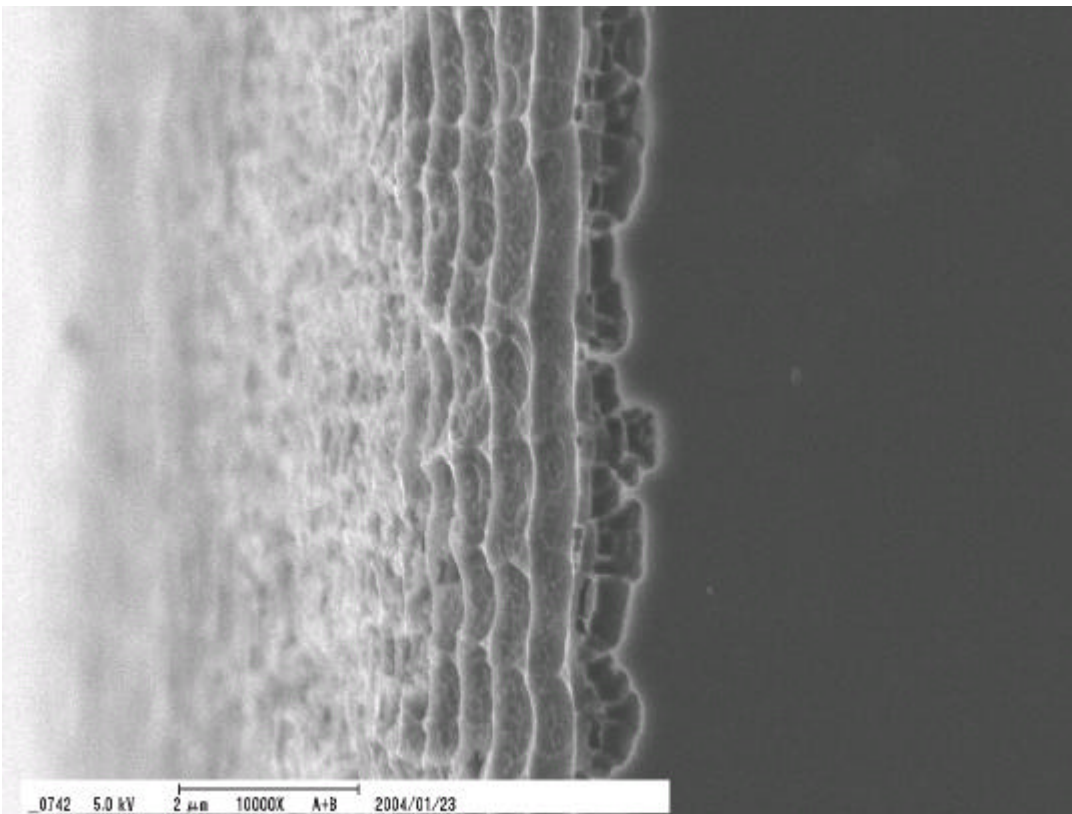


Fig 117: 300um location I

7 Extrapolation to pure torsion and proposed fracture criterion

7.1 Extrapolation to pure torsion

7.1.1 FEM model overview

A FEM model simulating pure torsion loading was constructed. The force applied to the specimen was given in the form of couple. A couple is a system of forces whereby forces of equal magnitudes act in opposite directions. The center of the couple was set to match point **A** on the specimen as shown in Fig 119 shown below. Fig 120 below shows a typical principal stress distribution. As can be observed, there is a symmetrical stress distribution on opposite sides, **a** and **b** of the beam. As such, load factor for path A and path B will be the same. A typical displacement distribution for pure torsion is shown below in Fig 121. Note that there should not be any displacement along the direction of the beam (**line A**).

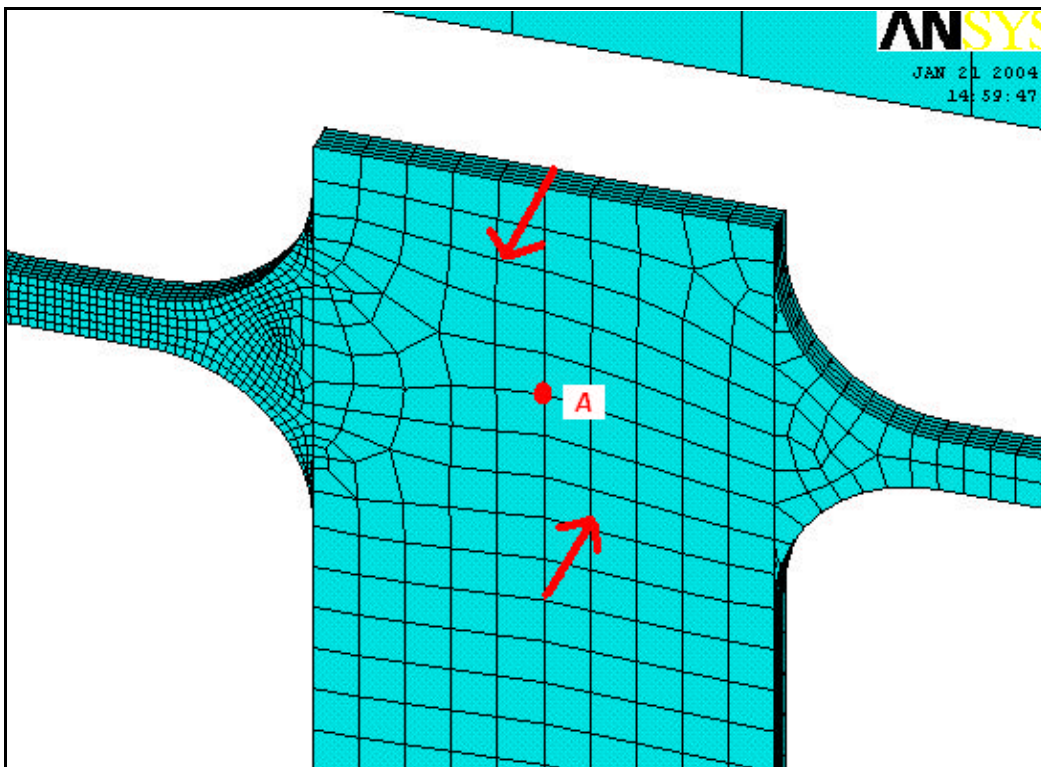


Fig 119: Couple applied to simulate pure torsion. **A** is the center of the couple.

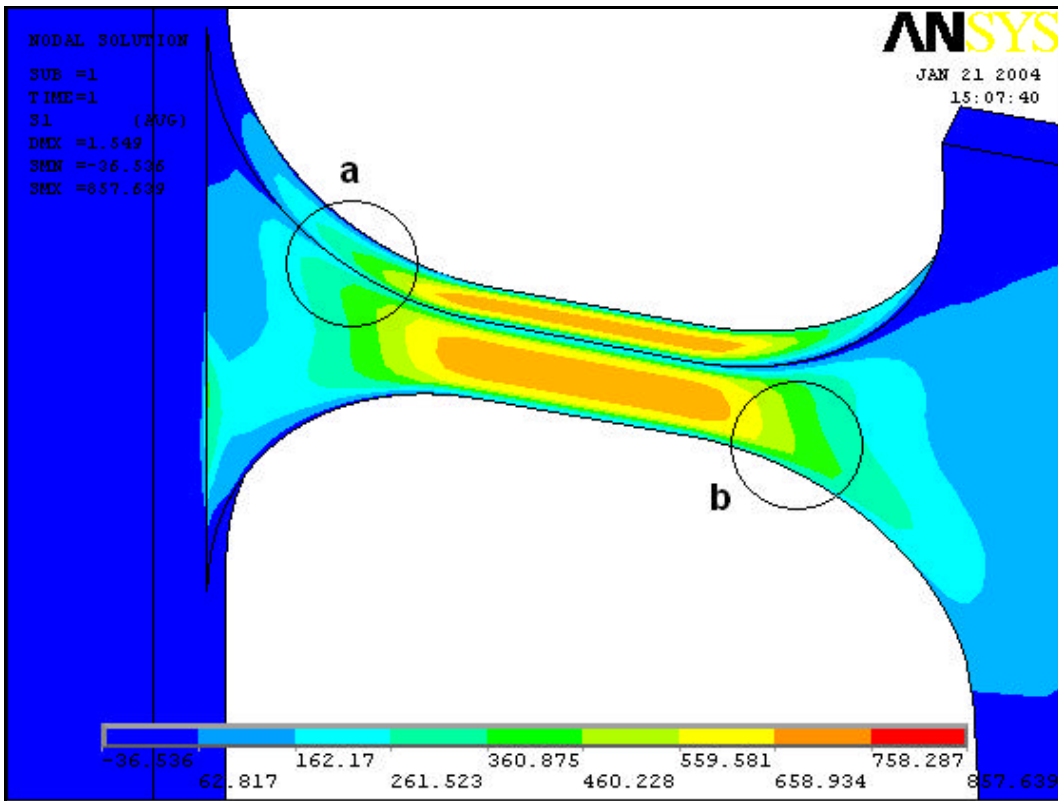


Fig 120: A typical principal stress distribution for pure bending (note that the stress distribution is symmetrical on opposite sides, namely *a* and *b*)

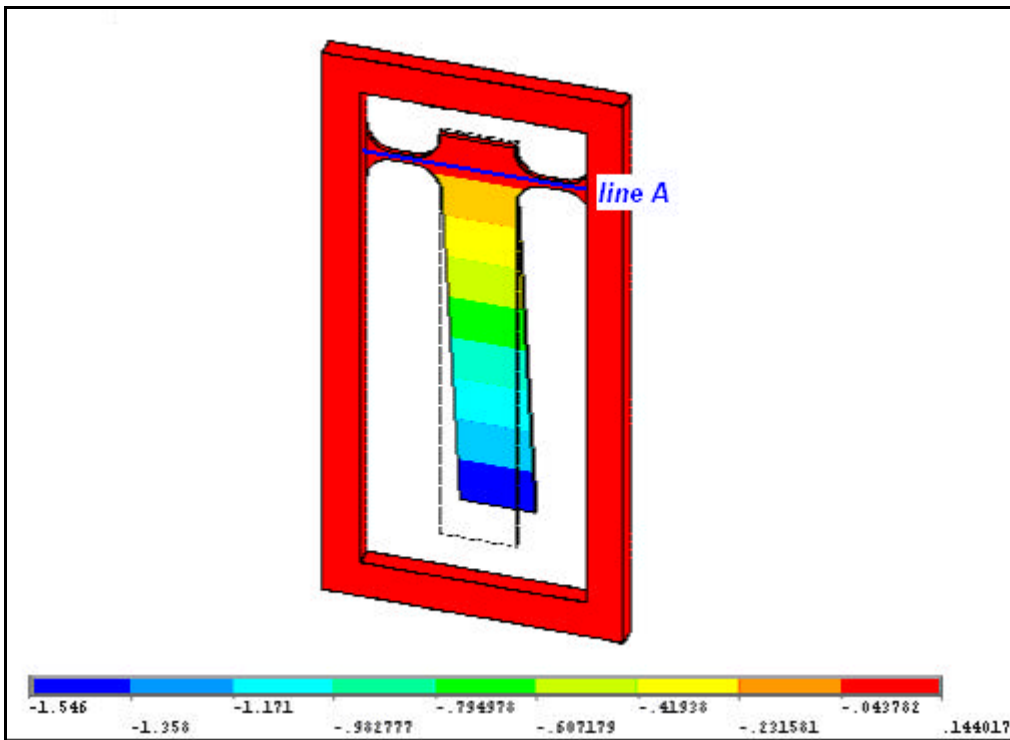


Fig 121: A typical displacement distribution for pure bending (note that displacement along *line A* should be zero)

7.1.2 Stress and load factor PDF for path A

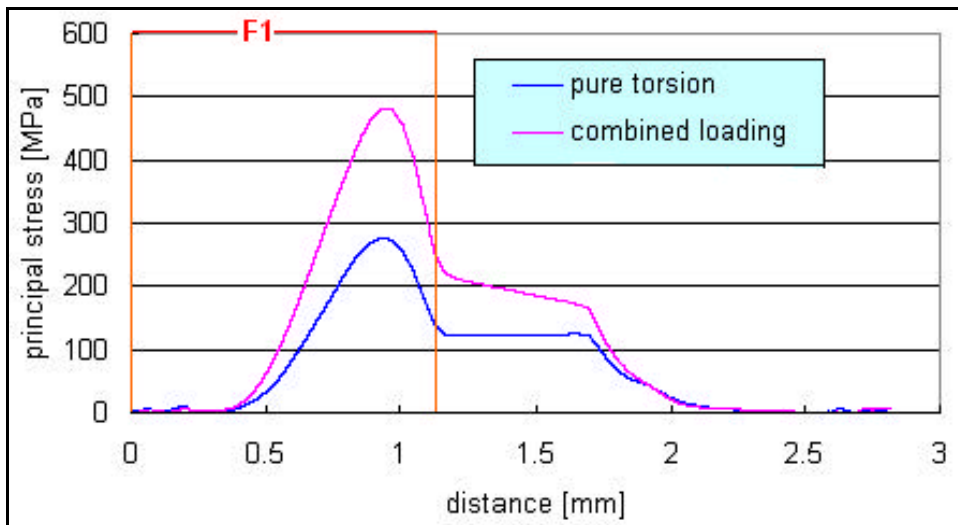


Fig 122: A typical principal **stress distribution** for pure torsion and combined loading (path A)

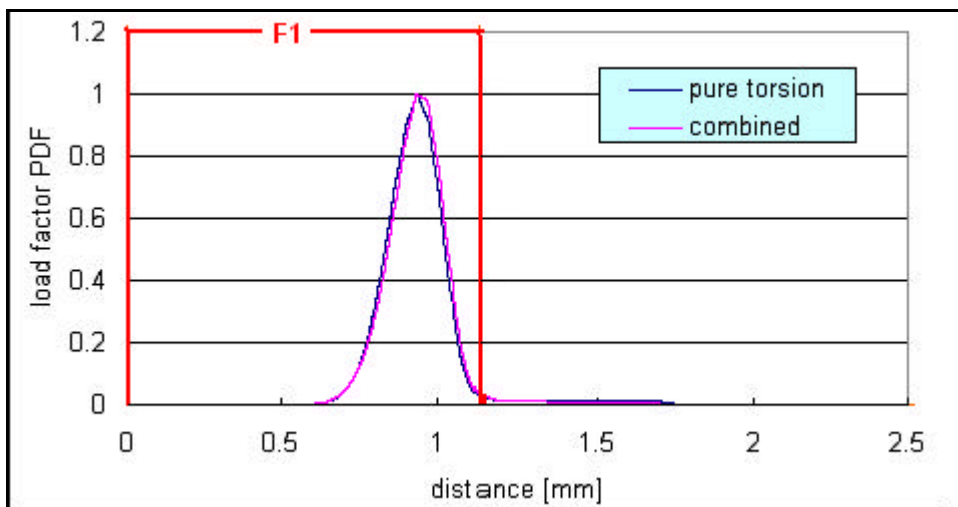


Fig 123: A typical **load factor PDF** for pure torsion and combined loading (path A)

7.1.3 Stress and load factor PDF for path B

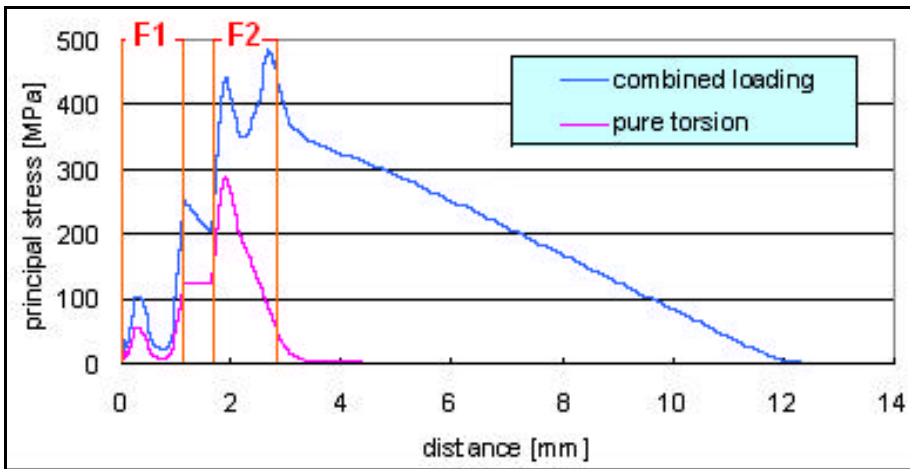


Fig 124: A typical principal **stress distribution** for pure torsion and combined loading (whole of path B)

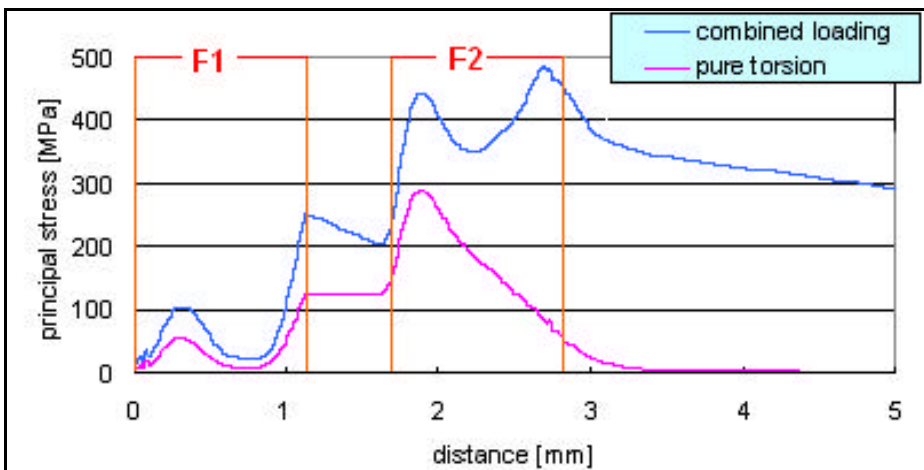


Fig 125: A typical principal **stress distribution** for pure torsion and combined loading (part of path B)

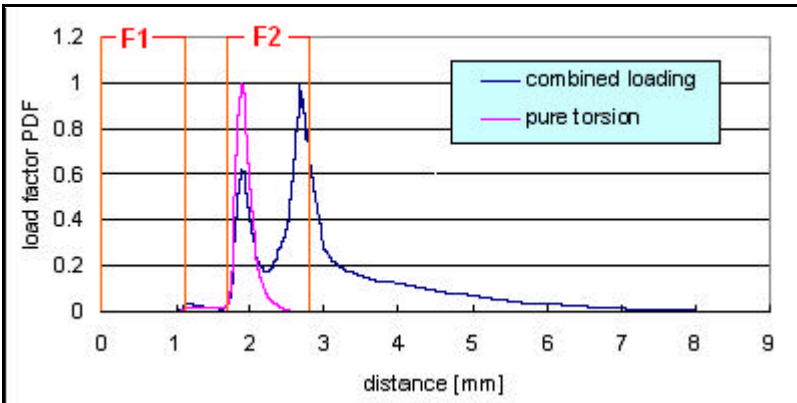


Fig 126: A typical **load factor PDF** for pure torsion and combined loading (whole of path B)

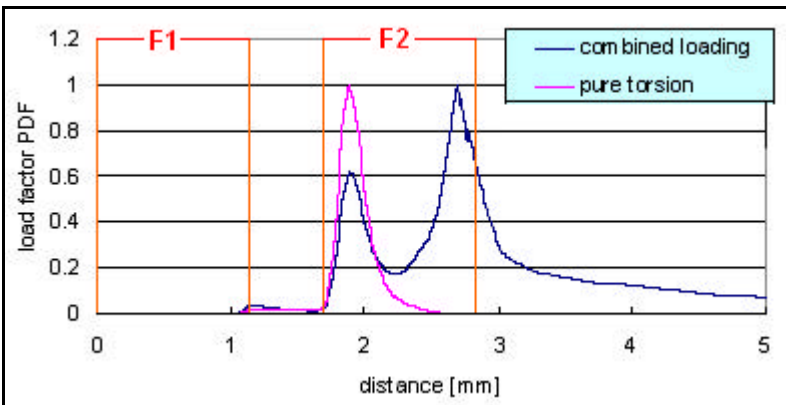


Fig 127: A typical **load factor PDF** for pure torsion and combined loading (part of path B)

7.1.4 Discussion and explanation

- **Path A:** From the stress and load factor PDF, there seems to be no noticeable difference. The load factor for 240um pure torsion is 0.0760 while that for 240um combined loading is 0.0748. The load factor for 300um pure torsion is 0.0704 while that for 300um combined loading is 0.0703.
- **Path B:** From the load PDF, one can infer that the load factor for combined loading is larger than that for pure torsion due to the existence of two significant peaks in the load factor graphs. Moreover, the load factor PDF for the combined loading is very much broader. The load factor for 240um pure torsion is 0.0760 while that for 240um combined loading is 0.319. The load factor for 300um pure torsion is 0.0704 while that for 300um combined loading is 0.266.
- **Inferences:** The **overall load factor** for combined loading is much larger than that for pure torsion. As such, a fracture criterion appropriate for combined loading should also be suitable for pure torsion. Nevertheless, the ability to perform better combined loading to mimic the pure torsion loading will result in less severe load factor for combined loading. In other words, the load factor for better combined loading test will be closer to that for pure torsion. Hence, from the industrial point of view, developmental cost can be saved.
- **SEM photos:** It can be observed that the flaws in the different regions of the fillet are similar in nature (size, orientation). Refer to Fig 102 to Fig 107 or Fig 110 to Fig 115 for the flaws around the fillet regions.

7.2 Proposed fracture criterion

7.2.1 No specific well-defined values

Fracture criterion to be proposed will not be some specific well-defined values. Instead, the fracture criterion will be in the form of a PDF (probability density function). This is because there are some uncertainties concerning the flaw population such as the size and orientation PDF throughout the beam length edge. Although three categories of flaws can be identified and their overall size and general orientation known, it is extremely difficult to characterize these flaws in term of flaw size or flaw orientation PDF.

Postulation: For instance, in the non-fillet region, the flaws could have a broader flaw orientation PDF. In the fillet region, the flaw orientation could be narrower with a significant peak at around 0° .

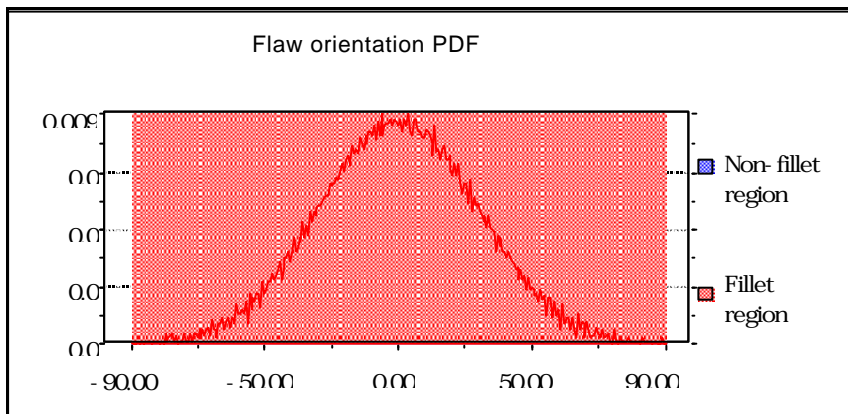


Fig 128: Graph showing **possible** flaw orientation PDFs for fillet and non-fillet regions (Note: horizontal axis shows the orientation of flaw in degree; the vertical axis shows the PDF values)

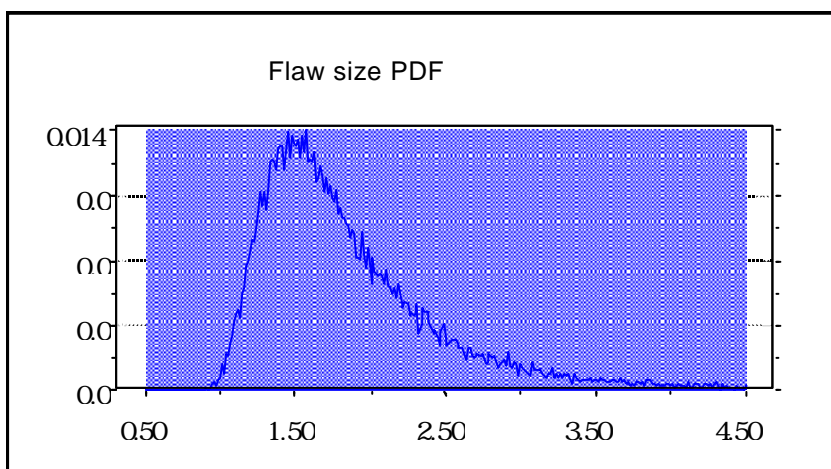


Fig 129: Graph showing a possible flaw size PDF (Note: the horizontal axis shows the flaw size in um; the vertical axis shows the pdf values)

7.2.2 Need for a separate fracture criterion for each form of geometry and loading

Each form of geometry (240um or 300um) or mode of loading (pure bending or combined loading) results in a particular form of stress distribution on the flaw population existing on the edge length of the beam. This warrants a separate fracture criterion for each form of geometry and loading. Hence, three fracture criteria can be considered: namely, pure bending (240um and 300um), combined loading 240um and combined loading 300um. Hence, the fracture criterion will be PDF based on parameters estimated from experiment data.

Table 32: MLM estimation of Weibull parameters

	Scale parameter [MPa]	Weibull modulus
Pure bending	783	7.77
240um combined	517	5.28
300um combined	306	4.98

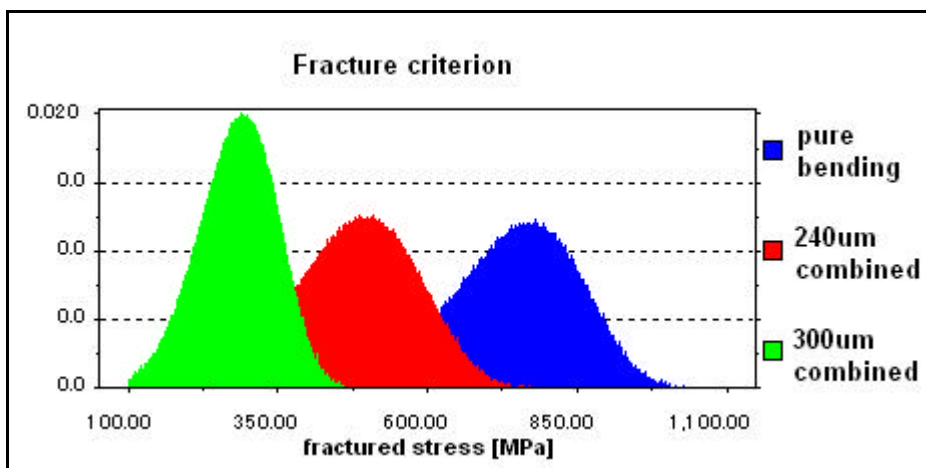


Fig 130: Proposed fracture criterion

8 Reliability analysis and safety design procedure

8.1 Overview

SCS (single crystal silicon) is a brittle material. Its fracture strength, which is largely dependent on the surface damage caused by the etching process, varies according to the MEMS structure and size, etching conditions, temperature, humidity, location on the wafer and type of wafer. Thus, fracture strength distribution estimated by performing fracture tests cannot be used directly for design purposes. It is highly probable that such fracture strength estimated experimentally will not differ greatly from the actual fracture strength. Nevertheless, there is a need to estimate reliably the fracture strength distribution to be used for actual structural design purposes. On the other hand, when one considers the production cost and time constraints, it is very likely that one will not have sufficient sample data to accurately estimate the fracture strength distribution (Weibull, etc.). Furthermore, in the case when a certain level of fracture strength is assured, the testing sample will not be stressed until the point of fracture. Instead, the testing sample will only be stressed to a certain level (below the actual fracture stress). Here, Bayesian reliability can be applied, in which past experimental data can be utilized as the prior PDF (probability density function). As such, only very few samples are required to effectively estimate the actual fracture strength PDF, which can be used for product structural evaluation (design, etc.). Moreover, censored data (unfractured data) can also be incorporated into Bayesian reliability analysis, which is thus more superior to the commonly used MLM (maximum likelihood method) in the absence of sufficient fractured data. **In this research, a general safety design procedure (refer to section 8.2) based on Bayesian reliability analysis is proposed.**

In the limiting case when there are an infinite number of samples, both the maximum likelihood method and Bayesian method will give the same estimate for the unknown parameters. **In the first part of this chapter (section 8.3), reliability analysis results using both Bayesian (using non-informative prior) and MLM based on actual experimental data (240um combined loading) will be presented.** In the case of finite samples, the two methods will give different estimates for the unknown parameters. The question arises as to which method is better. When there are very few samples, the Bayesian method is generally preferred. It is best that there is a prior knowledge of the PDF of the unknown parameters, which will result in better posterior PDF for the unknown parameters. Nevertheless, even if there is no expert opinion for the prior PDF, non-informative PDF for the unknown parameters can be used.

In the second half of this chapter, a case study in the form of simulation (section 8.4) comparing the effectiveness of Bayesian method and MLM is given. Weibull parameters, namely scale parameter and Weibull modulus are updated using both Bayesian (non-informative priors and normal priors) and MLM (maximum likelihood method) and the results are compared for 2 cases: when sample size is 3 and when sample size is 10. It has been observed that in the

absence of sufficient data, if one overestimates the scale parameter by two times, one can still obtain a reasonable posterior strength PDF, which is close to the actual data. Moreover, it has also been shown that the non-informative prior outperformed the MLM. Thus, if one really does not have any prior knowledge of the data PDF, one can still use the non-informative prior and get reasonably good estimate for the posterior strength PDF.

8.2 Safety design procedure

Here a safety design procedure is proposed. For demonstration purpose, it is assumed that n pieces of specimens have been tested, (i.e. fractured).

1. Loading test is performed on each specimen and the fracture stress for each specimen is estimated by FEM analysis aided by fractography
2. The Weibull parameters are then estimated based on the assumption that the fractured data follow a Weibull PDF. If n is small, Bayesian update method can be used. If there is no past data, non-informative priors can be used. If there are past data, normal prior PDFs for the Weibull parameters can be used. If n is large, other methods like MLM or moment method may be used. Hence, a fracture criterion (strength PDF) can be constructed based on the estimated Weibull parameters. Confidence intervals are also constructed for the Weibull parameters.
3. Based on the estimated Weibull parameters, the design stress PDF and failure probability can be determined. Here, the relationship between the design stress and failure probability is established.
4. The cost production function is then constructed and the required level of failure probability is set.
5. Determine the design stress bound. (Only the lower limit will be used for design)
6. Convert the design stress into displacement (angle of rotation)

Hence, a typical reliability specification will be **5.5°~6.0° with a failure probability of 1% at sample size n** . As the number of samples test is increased, the PDF for the Weibull parameters will become change such that the confidence interval width becomes narrower and the PDF becomes sharper. As a result, the design stress and hence the angle of rotation bound width will become smaller.

The next question will be how many samples to be tested. Here, a **test termination criterion could be based on incremental or marginal improvement in value a parameter of concern**, for instance the angle of rotation. In other words, if further improvement in the angle of rotation is found to be impractical or uneconomical, then the test should be terminated.

8.3 Results of reliability analysis based on actual experimental data

Bayesian parametric estimation is applied to **actual experimental data** (240 combined loading). The data were all uncensored. Both the scale and Weibull modulus were the unknown parameters to be estimated. For the prior PDF, the non-informative prior (refer to Theory) concerning both the scale and Weibull modulus was used. The scale and Weibull parameters were updated starting with five samples in increasing order of five samples until 25 samples have been reached. Fig 132 below shows the updated scale PDFs and Fig 133 shows the updated Weibull modulus PDFs. It can be observed that the PDFs become narrower and have sharper peaks as the sample size increases. A typical PDF and CDF for Weibull modulus are shown in Fig 131. In this paper, the confidence interval values were extracted from the CDF, which was calculated by numerically integrating the PDF. Modal values are extracted from PDF.

Here, the **95% confidence intervals** and **modal values** were extracted and the results were shown in Fig 134 and Fig 135. It can be observed that the width of 95% confidence intervals becomes smaller as the sample sizes increases. Moreover, the PDFs become less skewed as the sample size increases.

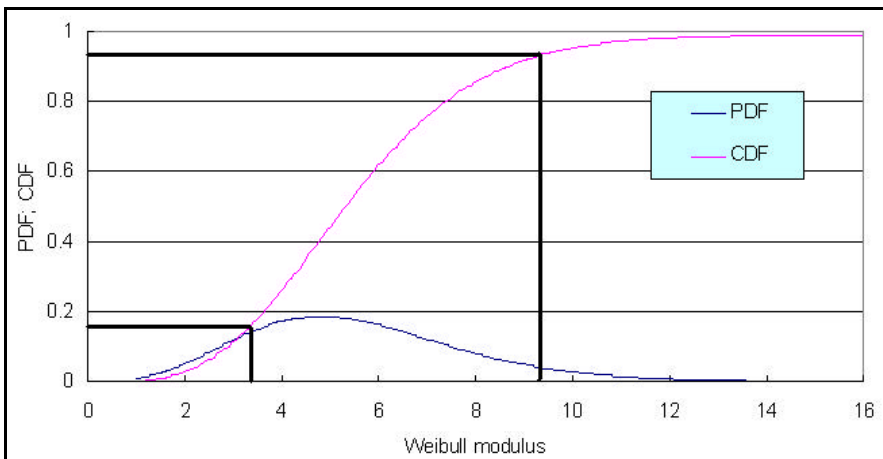


Fig 131: Extraction of confidence interval values from CDF (cumulative distribution function)

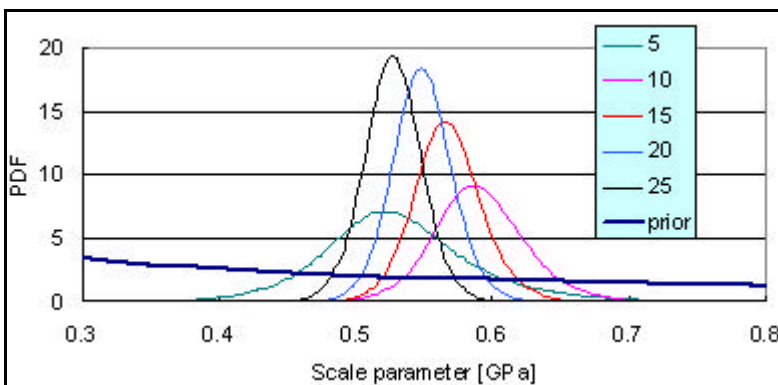


Fig 132: Updated scale parameter PDFs

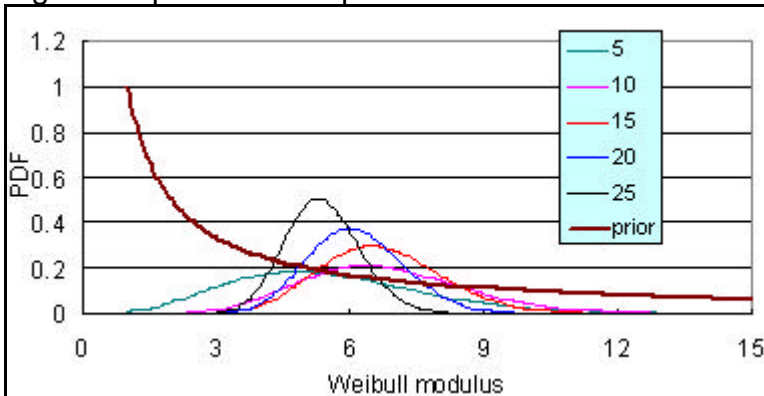


Fig 133: Updated Weibull modulus PDFs

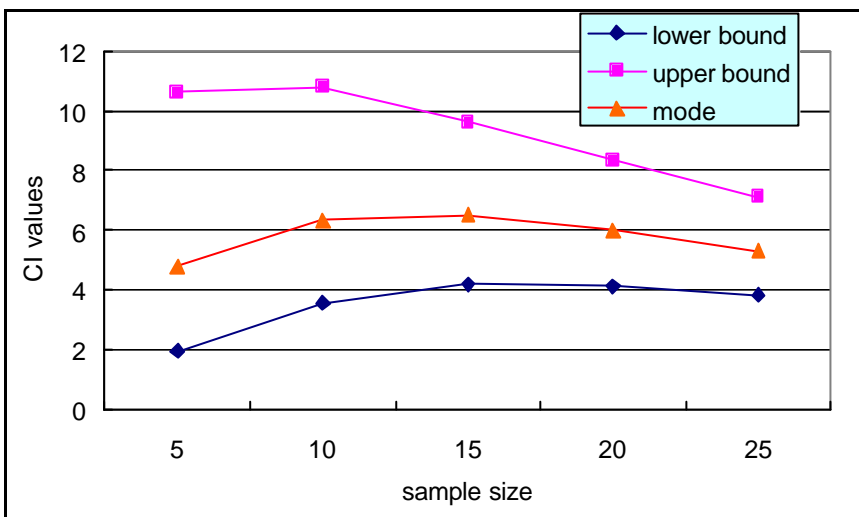


Fig 134: 95% C.I. values and modal values for Weibull modulus

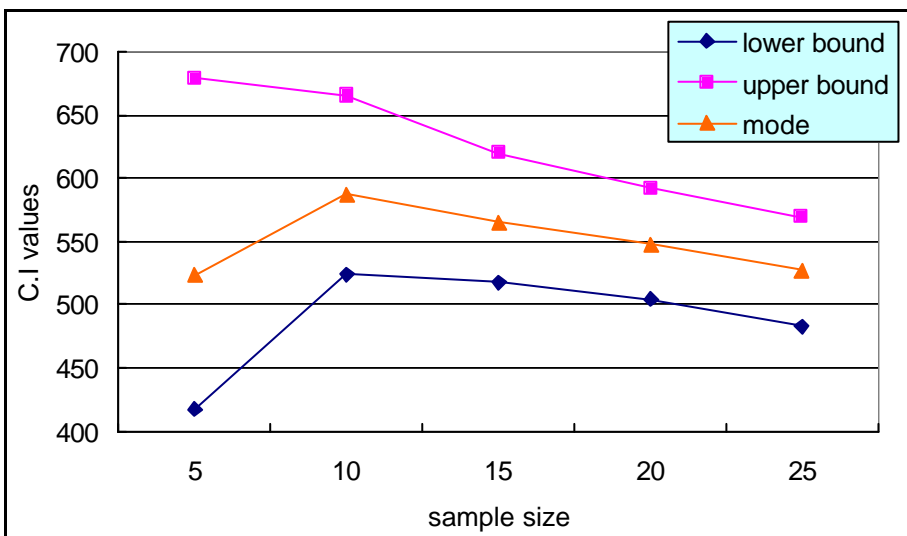


Fig 135: 95% C.I. values and modal values for scale parameter

Comparison with MLM:

The MLM and Bayesian method are equivalent in the asymptotic limit of infinite training data.

First, the **computational complexity**. In this case, the MLM is preferred since it requires merely differential calculus techniques rather than a possibly complex multidimensional integration needed in Bayesian method.

Next, the **interpretation**. The MLM seeks to find the parameter value that is best supported by the training data, i.e. maximizes the probability of obtaining the samples actual observed. In Bayesian estimation, the parameters are considered random variables having a known prior PDF; the training data convert this to a posterior PDF. The recursive Bayesian method updates the Bayesian parameter estimate incrementally, that is, as each training point is sampled. **Thus, the Bayesian method is, in principle, to be preferred.**

It had been shown previously (simulation) that the Weibull modulus (modal value) could be estimated more accurately when samples were limited. For the case of scale parameter (modal value), such a similar trend could not be observed. The results are shown in Table 33.

Table 33: Comparison between Bayesian and MLM (%value)

No of data	Scale parameter		Weibull modulus	
	Bayesian	MLM	Bayesian	MLM
4	94.3	93.9	139.0	209.0
6	97.1	98.0	125.0	158.0
8	105.7	104.0	93.0	109.0
10	102.9	104.0	105.0	119.0
15	102.9	101.7	100.0	109.0
20	100.0	99.4	86.0	91.5
25	100.0	100.1	97.0	102.0

Now, it can be observed that when there are few samples, the Bayesian method gives narrower confidence intervals for the Weibull modulus (Fig 136 and Fig 137) but a wider confidence interval for the scale parameter (Fig 138 and Fig 139). When the sample sizes increases, the confidence interval widths for both Weibull modulus and scale parameter converge.

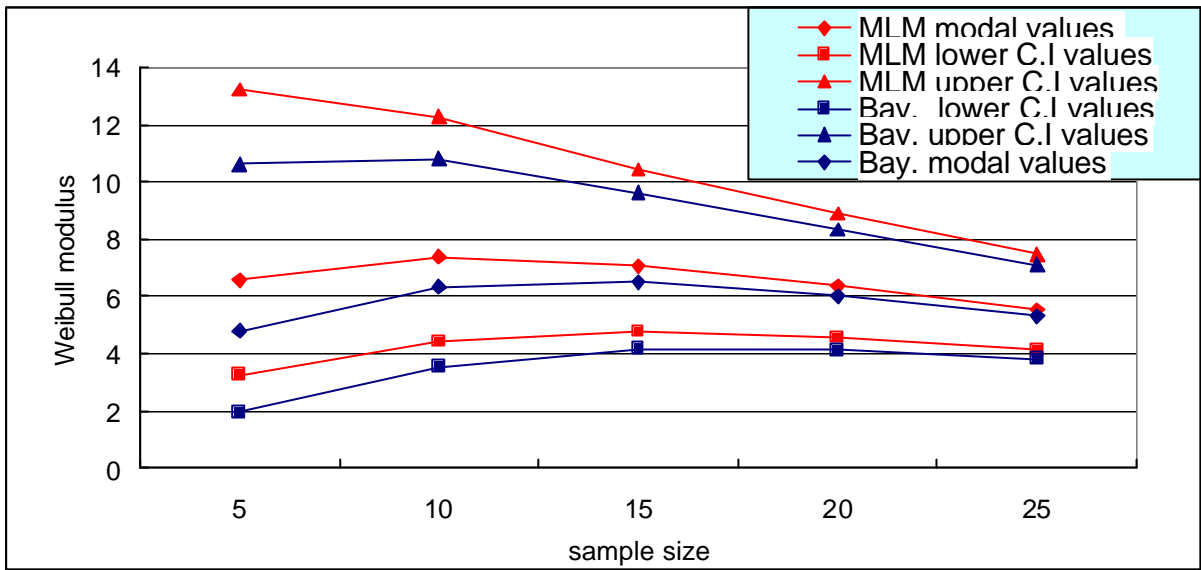


Fig 136: Comparison of Weibull modulus values between Bayesian method and MLM

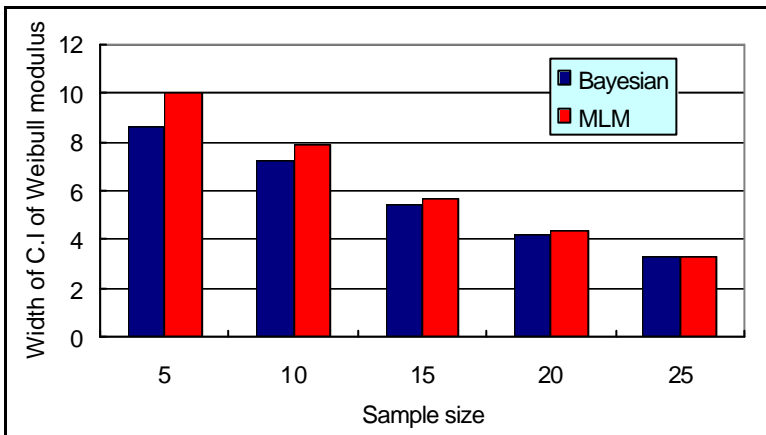
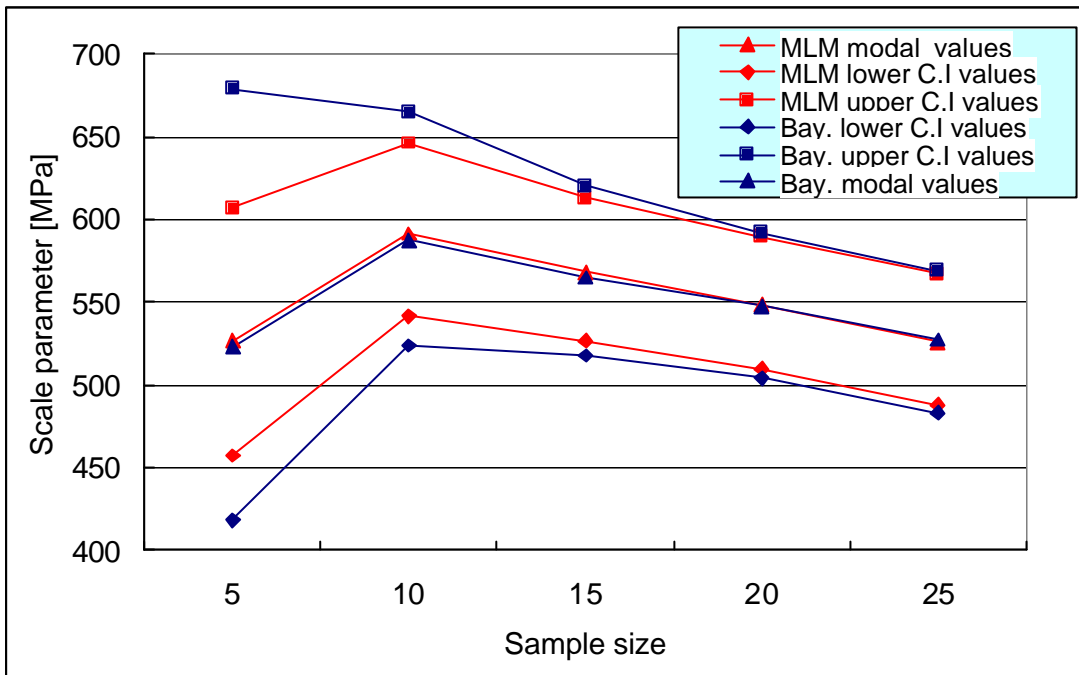


Fig 137: Comparison of Weibull modulus C.I width between Bayesian method and MLM



Fig

138: Comparison of scale parameter values between Bayesian method and MLM

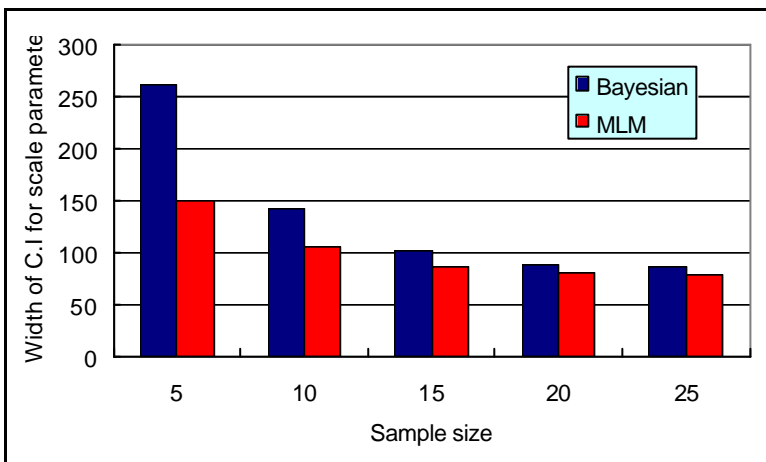


Fig 139: Comparison of scale parameter C.I width between Bayesian method and MLM

Relationship between the design stress and failure probability:

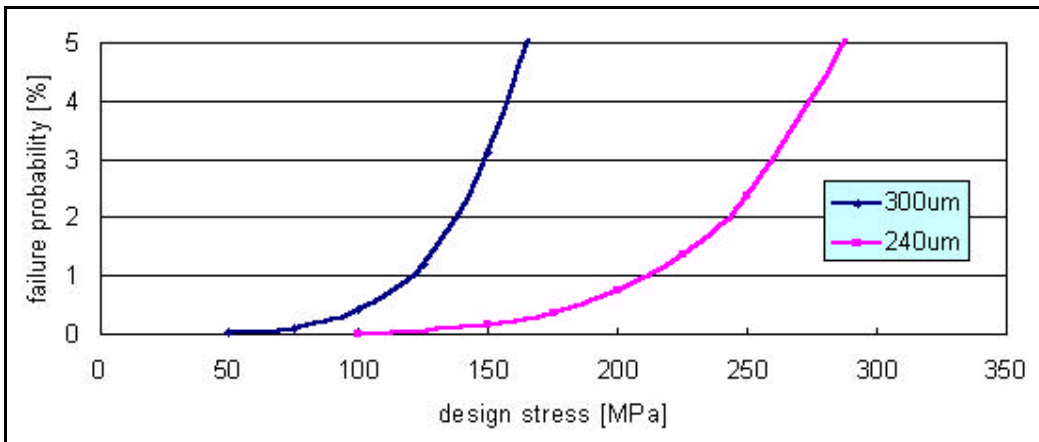


Fig 140: A typical relationship between the failure probability and design stress (normal problem)

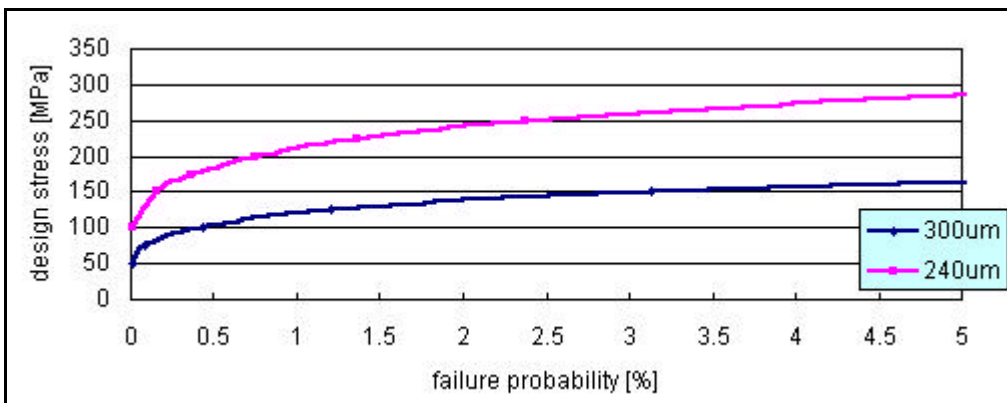


Fig 141: A typical relationship between the design stress and failure probability (reverse problem)

Table 34: A typical set of standard error and 95% confidence interval for failure probability (240um) obtained using Monte Carlo simulations

Design stress [MPa]	Failure probability [%]	Standard error	95% confidence interval	
100	0.01	0.003	0.004	0.016
150	0.155	0.012	0.131	0.179
175	0.367	0.019	0.330	0.404
200	0.748	0.027	0.695	0.801
225	1.359	0.037	1.287	1.431
250	2.366	0.048	2.272	2.460
300	6.196	0.076	6.047	6.345
350	13.039	0.106	12.830	13.248

Table 35: A typical set of standard error and 95% confidence interval for failure probability (300um) obtained using Monte Carlo simulations

Design stress [MPa]	Failure probability [%]	Standard error	95% confidence interval	
50	0.017	0.004	0.009	0.025
75	0.089	0.009	0.071	0.107
100	0.432	0.021	0.391	0.473
125	1.209	0.035	1.141	1.277
150	3.123	0.055	3.015	3.231
175	6.587	0.078	6.433	6.741
200	12.087	0.103	11.885	12.289

From a safety design point of view, the **failure probability** is first specified. Next, the relationship between the design stress and failure is determined by a combination of **Monte Carlo simulation** and an iterative procedure. (This is a reverse problem). The relationship between failure probability and (mean) design stress is shown in the Fig 140 and Fig 141. Here, the Latin hypercube sampling for the random number generation is used. For this sampling technique, the random input variables are sampled randomly according to their distribution functions, efficiently stratifying the samples into layers and avoiding the re-use of those layers. The sampling process has a "memory" of previous simulations, which prevents accumulation of clusters of samples. In addition, this sampling strategy forces the extreme ends of a distribution function to participate in the sampling. This generally leads to smoother distribution functions of the sampled set. For each design stress, 100,000 runs are performed to obtain failure probability. The confidence intervals (95%) for the failure probability are also constructed. The standard deviation of the design stress is assumed 10% of the mean design stress value. (Hence COV is assumed to be constant).

Moreover, the **failure probability** can also be obtained by an **analytical method** by approximating the non-normal PDF with a normal PDF. Here the Taylor expansion is performed at the failure point, which occurs at the left skirt of the PDF (refer to Fig 142). As such, for small failure probability, such an analytical method will give a more accurate estimation. The formula used for approximation to normal PDF are given below in equation (68):

$$\begin{aligned} m_{X_j} &= x_j^* - \left[\Phi^{-1} \left\{ F_{X_j}(x_j^*) \right\} \right] s_{X_j} \\ s_{X_j} &= \frac{j \left[\Phi^{-1} \left\{ F_{X_j}(x_j^*) \right\} \right]}{f_{X_j}(x_j^*)} \end{aligned} \quad \text{-----(68)}$$

m_{X_j} : Mean of normalized PDF

s_{X_j} : Standard deviation of normalized PDF

$f_{X_j}(x_j^*)$: Non-normal PDF for random variable X_j

$F_{X_j}(x_j^*)$: Non-normal CDF for random variable X_j

$j(x_j^*)$: Standardized normal PDF

$\Phi(x_j^*)$: Standardized normal CDF

x_j^* : Failure point

The unknown variables are m_{X_j} and s_{X_j} for a particular failure point x_j^* . Thus, the above equation (68) is solved iteratively.

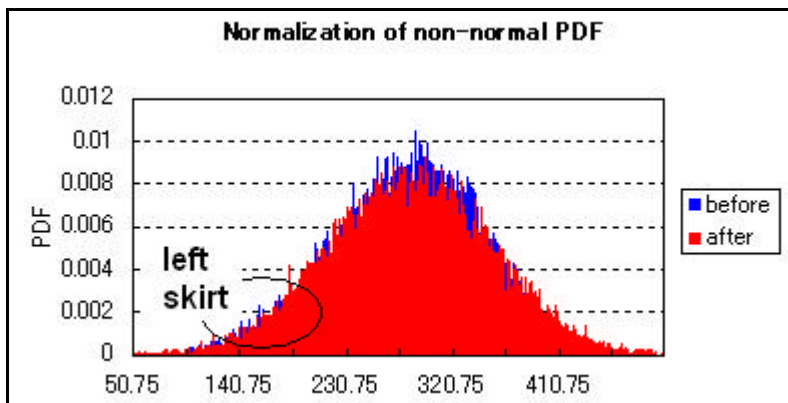


Fig 142: Normalization of non-normal PDF (before: PDF before normalization; after: PDF after normalization)

It can be observed from Fig 142 that at the left skirt, both PDFs (before and after) are almost equivalent. Note that the failure point is at 155.82 on the horizontal axis. At the failure point, both PDFs (before and after) have the same value.

Design stress bound:

(Assumption: for a constant failure probability) The **lower and upper bounds for the design stress PDF** were estimated as follows: the lower bound for design stress PDF can be determined by the combination of the lower confidence interval values of the scale and Weibull modulus. Similarly, the upper bound for design stress PDF can be determined by the combination of the higher confidence interval values of the scale and Weibull modulus. This explanation is shown in Fig 143 below. **The standard deviation of the design stress is assumed 10% of the mean design stress value.** (Hence COV is assumed to be constant). In the normal course of analysis, failure probability is determined when the stress and strength PDF are given. Now, the failure probability is first set and the design stress PDF is to be determined. Thus, this is a reverse problem, which can be solved by an iterative procedure. The relationship between failure probability and design stress for a large number of cases is determined and then an interpolation equation to relate the two variables is constructed. Typical design stress bounds are shown in Fig 144 and Fig 145 below. **Though the entire range of the design stress bound was shown, only the lower limit (left bound value) should be used in the design process.**

Finally, **the failure probability in this research is set at 1%.** However, there will be uncertainty regarding the failure probability and its confidence intervals. As such, it is advisable to treat the failure probability of 1% as **a relative value instead of as an absolute value.** Moreover, in the usual structural design, a failure probability of 1% is too high. However, in the case of MEMS reliability analysis, there is the proof test (screening test) in which products below a certain level of fracture strength are screened and removed. The proof test stress is usually set at a level whereby a certain number of samples will be fractured and removed. As such, if the failure probability is set too low (proof test stress will be too high), most samples will be fractured and removed.

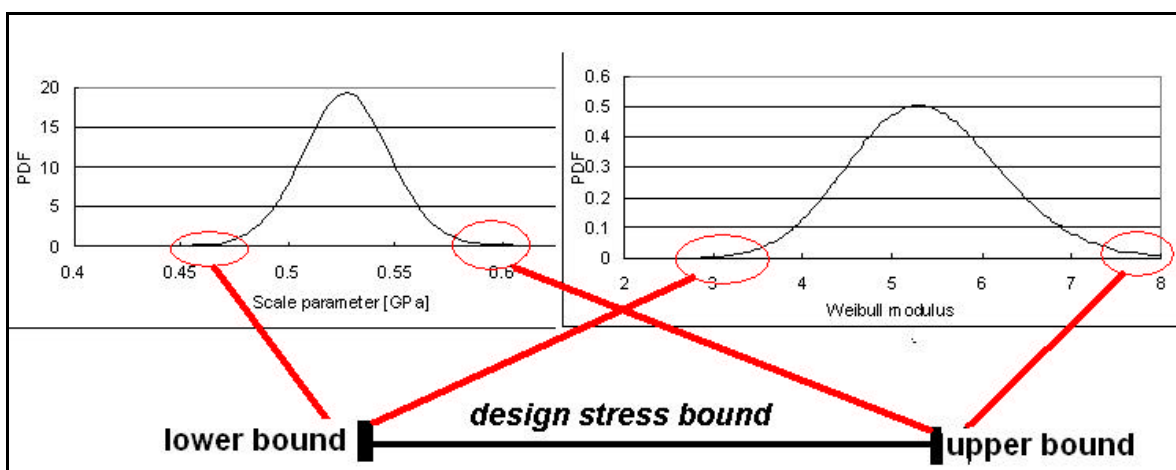


Fig 143: Explanation for determining the design stress bound

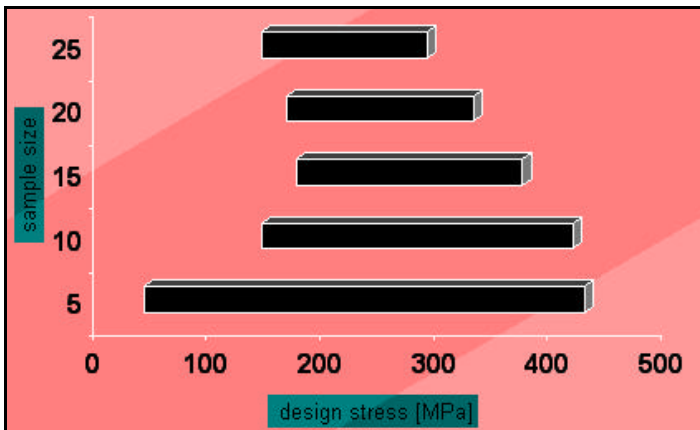


Fig 144: Design stress bounds determined using Bayesian method
 Note: failure probability is set at $(1\pm 0.06)\%$ 95% confidence interval]



Fig 145: Design stress bounds determined using MLM
 [Note: failure probability is set at $(1\pm 0.06)\%$ 95% confidence interval]

Relationship between displacement (angle of rotation) and design stress:

Since in the normal flow of analysis, the displacement (angle of rotation) is the input and the design stress is the output. Now, the reverse problem is to be solved: The design stress becomes the input and the displacement is the output.

normal problem: $design\ stress = function\ (displacement)$	-----(69)
reverse problem: $displacement = function^{-1}(design\ stress)$	

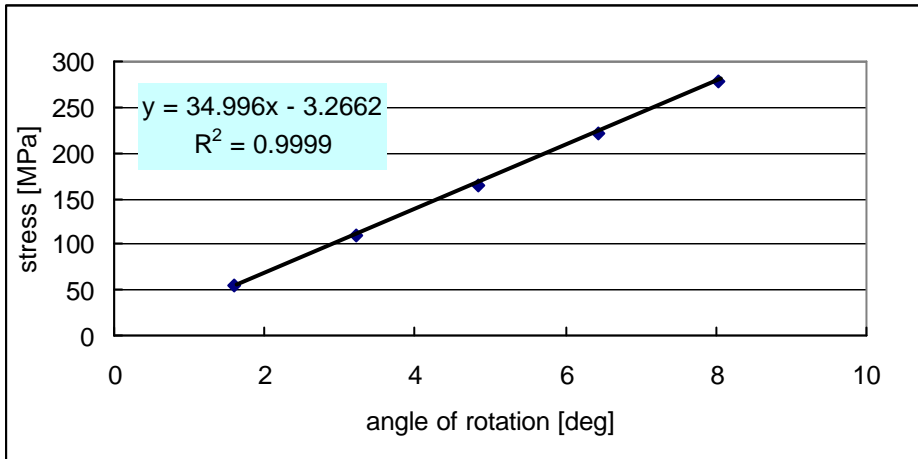


Fig 146: Graph of design stress versus angle of rotation for 240um pure torsion (normal problem)

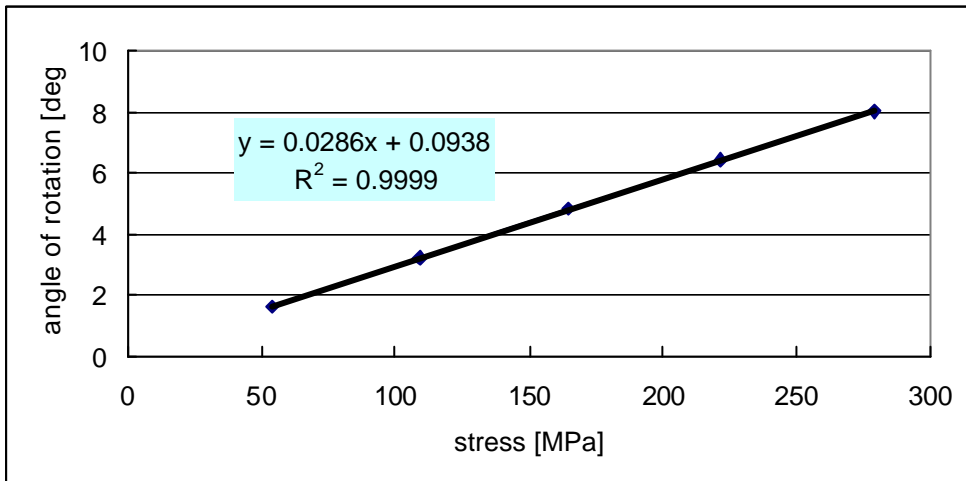


Fig 147: Graph of angle of rotation versus stress for 240um pure torsion (reverse problem)

A typical relationship between design stress and angle of rotation is shown in Fig 146 and Fig 147. As can be seen from the graphs, there is an almost perfect linear relationship between the design stress and the angle of rotation. For a more general case, probabilistic design is performed and surface response method can be used to determinate the relationship between the input parameters and output parameters. In this research, the input parameter was rotational angle and the output parameter was design stress at a particular location on the beam. For a more complex analysis, more input parameters, such as dimensions of beams, material constant, can be used.

Converting the design stress to rotational angle:

Probabilistic design was performed and surface response method was used to determine the relationship between the input parameters and output parameters. In this research, the input parameter is rotational angle and the output parameter is design stress at a particular location on the beam. Since the design stress and rotational angle has an almost 100% linear relationship, a wider design stress bound will be translated into a wider rotational angle bound of the same proportion. For a more complex analysis, more input parameters, such as dimensions of beams, material constant, can be used.

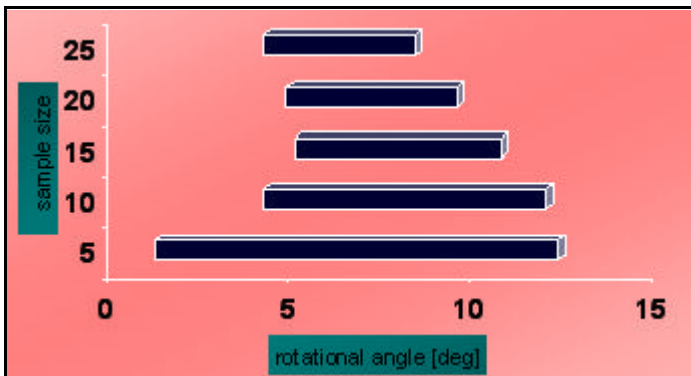


Fig 148: Rotational angle bounds determined using Bayesian method
[Note: failure probability is set at $(1\pm 0.06)\%$ 95% confidence interval]



Fig 149: Rotational angle bounds determined using MLM
[Note: failure probability is set at $(1\pm 0.06)\%$ 95% confidence interval]

Conclusion:

The underlying fractured data was assumed to follow a Weibull PDF, and Bayesian update and MLM estimation for two parameters, namely the scale parameter and Weibull modulus have been performed. When there were few samples, the Bayesian method using the non-informative prior could give a better estimate for Weibull modulus (modal value). Moreover, the confidence intervals for Weibull modulus were also narrower. On the other hand, for the case of scale parameter, such a trend could not be observed. The modal values estimated by both Bayesian method and MLM were almost the same. However, the Bayesian method gave much wider confidence intervals when the sample size was small. The design stress bounds determined by both the Weibull modulus and scale parameter were calculated and translated into rotational angle. For instance (refer to Fig 143 and Fig 144), at a failure probability of 1% and at a sample size of 25, both MLM and Bayesian method gave a rotational angle of about 5° (lower bound value).

8.4 Case study (simulation) on effectiveness of Bayesian update

The MLM estimation of past data (240um combined loading) has given a scale parameter of 0.517 GPa and a Weibull modulus of 5.28. Data, which followed a Weibull distribution, were then generated randomly. Then, the effectiveness of the Bayesian method with respect to the MLM was compared for two cases: when sample size is three and when sample size is ten (**mimicking data insufficiency**). For the Bayesian method, two types of prior PDFs were used. One of them was the **non-informative prior** for the Weibull parameters and the other one was **normal prior PDFs** for the Weibull parameters. The mean values of the prior normal PDF for the different cases for the scale parameter and Weibull modulus, and updating results (geometrical distance C) are shown in [Table 36](#) and [Table 38](#) for [sample size of three](#) and [sample size of ten](#) respectively. (The standard deviation is taken to be 20% of the mean value for both scale parameter and Weibull modulus).

The **geometrical distance C** (refer to Fig 150 below) between the posterior PDF and the true underlying parameters was also calculated to give a measure of effectiveness of each method. Moreover, a **corrective index** (refer to equation (70) below) was introduced to indicate whether how much the posterior PDF was closer to the true underlying parameters with respect to the prior PDF. A larger and more positive corrective index will indicate that the posterior PDF has become closer to the actual PDF after the Bayesian updating. **It is assumed that 100MPa is equivalent in distance to one unit of Weibull modulus, based on practical experiences.**

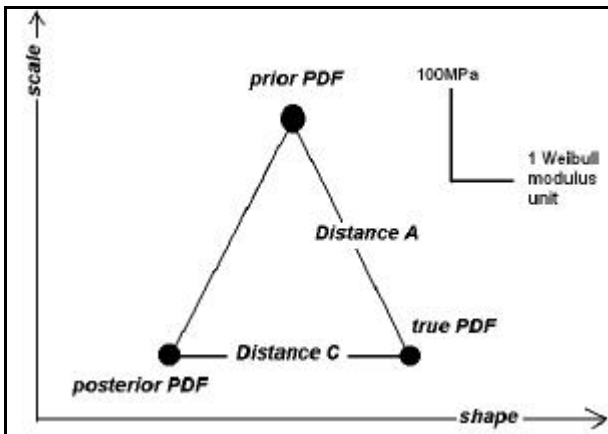


Fig 150: illustration of the various distances (note that modal values for each PDF are used)

$$\text{corrective index} = \frac{\text{distance A}}{\text{distance C}} - 1 \quad \text{-----(70)}$$

Table 36: Comparison of Bayesian method (non-informative prior and normal prior) and MLM (average of 10 sets of data; each set of data contained 3 samples)

	Shape (Weibull modulus)	Scale [GPa]	Bay. (Normal prior) Dist. C	MLM Dist. C	Bay. (non-informative) Dist. C	Corrective index	Ranking of corrective index
Case 1	5.280	1.034	0.582	3.745	2.660	7.876	1
Case 2	7.920	1.034	2.416	3.745	2.660	1.403	2
Case 3	2.640	1.034	3.334	3.745	2.660	0.741	4
Case 4	7.920	0.517	2.361	3.745	2.660	0.118	6
Case 5	2.640	0.517	2.464	3.745	2.660	0.072	8
Case 6	5.280	0.259	1.883	3.745	2.660	0.373	5
Case 7	7.920	0.259	2.032	3.745	2.660	0.818	3
Case 8	2.640	0.259	3.377	3.745	2.660	0.094	7
Case 9	5.280	0.517	0.506	3.745	2.660	NA	NA

Best
 Worst

Table 37: Standard deviations of distance C for the different cases under Bayesian (normal and non-informative priors) and MLM for a **sample size of 3**

	Bay. (Normal prior) Dist. C	Standard deviation	MLM Dist. C	Standard deviation	Bay (non-informative) Dist. C	Standard deviation
Case 1	0.582	0.438	3.745	2.736	2.660	1.381
Case 2	2.416	0.811	3.745	2.736	2.660	1.381
Case 3	3.334	0.224	3.745	2.736	2.660	1.381
Case 4	2.361	0.861	3.745	2.736	2.660	1.381
Case 5	2.464	0.077	3.745	2.736	2.660	1.381
Case 6	1.883	0.635	3.745	2.736	2.660	1.381
Case 7	2.032	0.763	3.745	2.736	2.660	1.381
Case 8	3.377	0.150	3.745	2.736	2.660	1.381
Case 9	0.506	0.258	3.745	2.736	2.660	1.381

Firstly, from **Table 36**, it can be observed that out of nine cases of normal prior PDFs, seven cases were more superior compared to MLM or Bayesian (non-informative prior). Besides, out of these seven cases, case 1 had the highest corrective index, followed by case 2 and case 7. In other words, if twice the actual scale parameter was inputted as the mean for the normal prior PDF (the shape parameter is inputted correctly), the posterior PDF will become much closer to the actual PDF after the Bayesian updating. Moreover, it can be observed that Bayesian update using the non-informative prior was more effective the MLM.

Table 38: Comparison of Bayesian method (non-informative prior and normal prior) and MLM (average of 10 sets of data; each set of data contained **10 samples**)

	Shape	Scale	Bay (normal prior) Dist. C	MLM Dist. C	Bay (non-informative) Dist. C	Corrective index	Ranking of corrective index
Case 1	5.280	1.034	0.677	2.020	1.870	6.638	1
Case 2	7.920	1.034	1.658	2.020	1.870	2.502	2
Case 3	2.640	1.034	2.145	2.020	1.870	1.706	3
Case 4	7.920	0.517	1.587	2.020	1.870	0.663	6
Case 5	2.640	0.517	2.129	2.020	1.870	0.240	8
Case 6	5.280	0.259	1.237	2.020	1.870	1.090	5
Case 7	7.920	0.259	1.669	2.020	1.870	1.214	4
Case 8	2.640	0.259	2.783	2.020	1.870	0.328	7
Case 9	5.280	0.517	0.668	2.020	1.870	NA	NA


Best
Worst

Table 39: Standard deviations of distance C for the different cases under Bayesian (normal and non-informative priors) and MLM for a **sample size of 10**

	Bay. (Normal prior) Dist. C	Standard deviation	MLM Dist. C	Standard deviation	Bay (non-informative) Dist. C	Standard deviation
Case 1	0.677	0.241	2.020	1.506	1.870	1.274
Case 2	1.658	1.239	2.020	1.506	1.870	1.274
Case 3	2.145	0.154	2.020	1.506	1.870	1.274
Case 4	1.587	1.251	2.020	1.506	1.870	1.274
Case 5	2.129	0.161	2.020	1.506	1.870	1.274
Case 6	1.237	0.669	2.020	1.506	1.870	1.274
Case 7	1.669	0.585	2.020	1.506	1.870	1.274
Case 8	2.783	0.212	2.020	1.506	1.870	1.274
Case 9	0.668	0.234	2.020	1.506	1.870	1.274

Next, a **sample size of 10** was used and the results are shown **Table 38**. As can be observed, results were generally similar to the case when the sample size was three were obtained. It can be observed that out of nine cases of normal prior PDFs, six cases were more superior compared to MLM or Bayesian (non-informative prior). Besides, out of these six cases, case 1 had the highest corrective index, followed by case 2 and case 3. In other words, if twice the actual scale parameter was inputted as the mean for the normal prior PDF (the shape parameter is inputted correctly), the posterior PDF will become much closer to the actual PDF after the Bayesian updating. The same result was also obtained when the sample size was three.

Another point to note is that, for case two when both the scale parameter and Weibull modulus were overestimated, a high corrective index (ranking no. 2) was obtained. On the other hand, for case five when the Weibull modulus was underestimated (scale parameter correctly estimated), the corrective index became very low (in fact the lowest among all the cases). **This implies that it is better to overestimate the scale or Weibull parameter (assuming the other parameter is known) rather than to underestimate them.**

In general, for almost all cases, distance C has decreased. This is due to the greater corrective effect as the sample size increases. **The effectiveness of using the non-informative prior as opposed to using MLM has decreased, as can be observed from the decreased difference in distance C value between Bayesian (non-informative) and MLM.**

Hence, in the future, as the etching process improves, the scale parameter, which is an indication of the mean strength of the data, will also increase. Based on the results in Table 36, one can use just a few samples (preferably about 3 samples) to roughly predict the strength of the new samples produced by the new and improved etching process. If one really does not have a prior knowledge of the sample strength, one can still use the non-informative prior.

In this research, all the data was **uncensored**. However, in real applications, it is highly possible that some of the fractured data will be censored. This means that the samples are still unfractured at the end of their period of use. Hence, it is a need to develop a safety design procedure for such a need. **Censored data** can be accounted for by simply multiplying the maximum likelihood function with an additional term as shown in equation (71) below:

$$\prod_{i=1}^n g(x_i | \mathbf{q}) \times \prod_{j=1}^m \{1 - G(x_j^* | \mathbf{q})\} \text{-----(71)}$$

$\prod_{i=1}^n g(x_i | \mathbf{q})$: Likelihood function

$\prod_{j=1}^m \{1 - G(x_j^* | \mathbf{q})\}$: Additional term to account for censored data

$g(x_i | \mathbf{q})$: PDF for x_i given θ

$G(x_j^* | \mathbf{q})$: CDF for x_j^* given θ

x_i : Uncensored data from $i=1$ to $i=m$

x_j^* : Censored data $j=1$ to $j=m$

Raw results for Table 36 calculated above:

Table 40: Set (1) calculation results when sample size =3

Set 1	Shape	Scale	Bay (normal prior) Dist. C	MLM Dist. C	Bay (non-informative) Dist. C
Case 1	5.280	1.034	1.619	8.687	5.055
Case 2	7.920	1.034	3.375	8.687	5.055
Case 3	2.640	1.034	3.776	8.687	5.055
Case 4	7.920	0.517	3.183	8.687	5.055
Case 5	2.640	0.517	2.449	8.687	5.055
Case 6	5.280	0.259	2.954	8.687	5.055
Case 7	7.920	0.259	3.401	8.687	5.055
Case 8	2.640	0.259	3.618	8.687	5.055
Case 9	5.280	0.517	0.921	8.687	5.055

SET_1	Shape	Scale	Data	
Case 1	5.660	0.674	x1	0.644
Case 2	8.366	0.654	x2	0.530
Case 3	2.810	0.803	x3	0.671
Case 4	8.301	0.617		
Case 5	2.881	0.566		
Case 6	2.621	0.388		
Case 7	2.230	0.367		
Case 8	2.043	0.355		
Case 9	5.658	0.601		
MLM	13.878	0.641		
Non-inform.	10.197	0.634		

Table 41: Set (2) calculation results when sample size =3

Set 2	Shape	Scale	Bay (normal prior) Dist. C	MLM Dist. C	Bay (non- informative) Dist. C
Case 1	5.280	1.034	0.304	2.525	0.769
Case 2	7.920	1.034	2.651	2.525	0.769
Case 3	2.640	1.034	3.254	2.525	0.769
Case 4	7.920	0.517	2.632	2.525	0.769
Case 5	2.640	0.517	2.405	2.525	0.769
Case 6	5.280	0.259	1.452	2.525	0.769
Case 7	7.920	0.259	1.229	2.525	0.769
Case 8	2.640	0.259	3.292	2.525	0.769
Case 9	5.280	0.517	0.328	2.525	0.769

SET_2	Shape	Scale	Data	
Case 1	5.501	0.538	x1	0.559
Case 2	7.931	0.523	x2	0.464
Case 3	2.700	0.715	x3	0.393
Case 4	7.909	0.504		
Case 5	2.881	0.499		
Case 6	4.464	0.397		
Case 7	6.125	0.428		
Case 8	2.506	0.340		
Case 9	5.549	0.498		
MLM	7.801	0.502		
Non-inform.	6.004	0.491		

Table 42: Set (3) calculation results when sample size =3

Set 3	Shape	Scale	Bay (normal prior) Dist. C	MLM Dist. C	Bay (non-informative) Dist. C
Case 1	5.280	1.034	0.336	5.399	2.707
Case 2	7.920	1.034	2.941	5.399	2.707
Case 3	2.640	1.034	3.155	5.399	2.707
Case 4	7.920	0.517	2.971	5.399	2.707
Case 5	2.640	0.517	2.412	5.399	2.707
Case 6	5.280	0.259	1.331	5.399	2.707
Case 7	7.920	0.259	2.107	5.399	2.707
Case 8	2.640	0.259	3.243	5.399	2.707
Case 9	5.280	0.517	0.572	5.399	2.707

SET_3	Shape	Scale	Data	
Case 1	5.587	0.503	x1	0.375
Case 2	8.204	0.486	x2	0.468
Case 3	2.687	0.697	x3	0.506
Case 4	8.219	0.473		
Case 5	2.889	0.485		
Case 6	4.902	0.389		
Case 7	7.143	0.419		
Case 8	2.599	0.335		
Case 9	5.649	0.473		
MLM	10.661	0.473		
Non-inform.	7.938	0.466		

Table 43: Set (4) calculation results when sample size =3

Set 4	Shape	Scale	Bay (normal prior) Dist. C	MLM Dist. C	Bay (non-informative) Dist. C
Case 1	5.280	1.034	0.509	6.849	4.266
Case 2	7.920	1.034	3.077	6.849	4.266
Case 3	2.640	1.034	3.296	6.849	4.266
Case 4	7.920	0.517	3.082	6.849	4.266
Case 5	2.640	0.517	2.371	6.849	4.266
Case 6	5.280	0.259	1.272	6.849	4.266
Case 7	7.920	0.259	1.669	6.849	4.266
Case 8	2.640	0.259	3.285	6.849	4.266
Case 9	5.280	0.517	0.449	6.849	4.266

SET_4	Shape	Scale	Data	
Case 1	5.658	0.551	x1	0.475
Case 2	8.354	0.531	x2	0.559
Case 3	2.738	0.727	x3	0.464
Case 4	8.362	0.514		
Case 5	2.910	0.510		
Case 6	4.605	0.409		
Case 7	6.787	0.445		
Case 8	2.476	0.346		
Case 9	5.723	0.510		
MLM	12.129	0.520		
Non-inform.	9.545	0.514		

Table 44: Set (5) calculation results when sample size =3

Set 5	Shape	Scale	Bay (normal prior) Dist. C	MLM Dist. C	Bay (non- informative) Dist. C
Case 1	5.280	1.034	0.996	2.637	3.608
Case 2	7.920	1.034	0.921	2.637	3.608
Case 3	2.640	1.034	3.632	2.637	3.608
Case 4	7.920	0.517	0.720	2.637	3.608
Case 5	2.640	0.517	2.635	2.637	3.608
Case 6	5.280	0.259	2.870	2.637	3.608
Case 7	7.920	0.259	3.034	2.637	3.608
Case 8	2.640	0.259	3.629	2.637	3.608
Case 9	5.280	0.517	0.653	2.637	3.608

SET_5	Shape	Scale	Data	
Case 1	4.591	0.589	x1	0.176
Case 2	6.038	0.569	x2	0.604
Case 3	2.493	0.750	x3	0.514
Case 4	5.991	0.528		
Case 5	2.648	0.503		
Case 6	2.895	0.357		
Case 7	2.740	0.351		
Case 8	2.190	0.327		
Case 9	4.627	0.518		
MLM	2.660	0.487		
Non-inform.	1.802	0.421		

Table 45: Set (6) calculation results when sample size =3

Set 6	Shape	Scale	Bay (normal prior) Dist. C	MLM Dist. C	Bay (non- informative) Dist. C
Case 1	5.280	1.034	0.564	1.692	2.696
Case 2	7.920	1.034	1.354	1.692	2.696
Case 3	2.640	1.034	3.393	1.692	2.696
Case 4	7.920	0.517	1.210	1.692	2.696
Case 5	2.640	0.517	2.538	1.692	2.696
Case 6	5.280	0.259	2.327	1.692	2.696
Case 7	7.920	0.259	2.112	1.692	2.696
Case 8	2.640	0.259	3.464	1.692	2.696
Case 9	5.280	0.517	0.382	1.692	2.696

SET_6	Shape	Scale	Data	
Case 1	4.914	0.560	x1	0.60
Case 2	6.596	0.549	x2	0.43
Case 3	2.583	0.723	x3	0.27
Case 4	6.490	0.518		
Case 5	2.753	0.494		
Case 6	3.474	0.370		
Case 7	3.695	0.377		
Case 8	2.368	0.329		
Case 9	4.917	0.505		
MLM	3.622	0.483		
Non-inform.	2.675	0.448		

Table 46: Set (7) calculation results when sample size =3

Set 7	Shape	Scale	Bay (normal prior) Dist. C	MLM Dist. C	Bay (non- informative) Dist. C
Case 1	5.280	1.034	0.231	3.453	1.186
Case 2	7.920	1.034	2.751	3.453	1.186
Case 3	2.640	1.034	3.193	3.453	1.186
Case 4	7.920	0.517	2.773	3.453	1.186
Case 5	2.640	0.517	2.422	3.453	1.186
Case 6	5.280	0.259	1.397	3.453	1.186
Case 7	7.920	0.259	1.721	3.453	1.186
Case 8	2.640	0.259	3.272	3.453	1.186
Case 9	5.280	0.517	0.465	3.453	1.186

SET_7	Shape	Scale	Data	
Case 1	5.509	0.514	x1	0.36
Case 2	8.023	0.497	x2	0.52
Case 3	2.679	0.702	x3	0.48
Case 4	8.031	0.483		
Case 5	2.875	0.488		
Case 6	4.695	0.390		
Case 7	6.705	0.421		
Case 8	2.561	0.335		
Case 9	5.567	0.480		
MLM	8.714	0.480		
Non-inform.	6.371	0.470		

Table 47: Set (8) calculation results when sample size =3

Set 8	Shape	Scale	Bay (normal prior) Dist. C	MLM Dist. c	Bay (non- informative) Dist. C
Case 1	5.280	1.034	0.623	5.223	3.001
Case 2	7.920	1.034	3.032	5.223	3.001
Case 3	2.640	1.034	3.048	5.223	3.001
Case 4	7.920	0.517	3.062	5.223	3.001
Case 5	2.640	0.517	2.445	5.223	3.001
Case 6	5.280	0.259	1.444	5.223	3.001
Case 7	7.920	0.259	2.543	5.223	3.001
Case 8	2.640	0.259	3.216	5.223	3.001
Case 9	5.280	0.517	0.832	5.223	3.001

SET_8	Shape	Scale	Data	
Case 1	5.617	0.465	x1	0.48
Case 2	8.235	0.449	x2	0.37
Case 3	2.661	0.673	x3	0.40
Case 4	8.247	0.441		
Case 5	2.886	0.467		
Case 6	5.186	0.373		
Case 7	7.521	0.397		
Case 8	2.696	0.326		
Case 9	5.671	0.444		
MLM	10.443	0.438		
Non-inform.	8.156	0.432		

Table 48: Set (9) calculation results when sample size =3

Set 9	Shape	Scale	Bay (normal prior) Dist. C	MLM Dist. C	Bay (non- informative) Dist. C
Case 1	5.280	1.034	0.516	0.145	1.462
Case 2	7.920	1.034	2.232	0.145	1.462
Case 3	2.640	1.034	3.399	0.145	1.462
Case 4	7.920	0.517	2.189	0.145	1.462
Case 5	2.640	0.517	2.464	0.145	1.462
Case 6	5.280	0.259	1.973	0.145	1.462
Case 7	7.920	0.259	1.253	0.145	1.462
Case 8	2.640	0.259	3.414	0.145	1.462
Case 9	5.280	0.517	0.018	0.145	1.462

SET_9	Shape	Scale	Data	
Case 1	5.258	0.569	x1	0.56
Case 2	7.487	0.551	x2	0.55
Case 3	2.658	0.733	x3	0.31
Case 4	7.467	0.526		
Case 5	2.818	0.507		
Case 6	3.773	0.390		
Case 7	4.591	0.412		
Case 8	2.369	0.339		
Case 9	5.298	0.517		
MLM	5.424	0.518		
Non-inform.	3.833	0.496		

Table 49: Set (10) calculation results when sample size =3

Set 10	Shape	Scale	Bay (normal prior) Dist. C	MLM Dist. C	Bay (non- informative) Dist. C
Case 1	5.280	1.034	0.125	0.843	1.856
Case 2	7.920	1.034	1.827	0.843	1.856
Case 3	2.640	1.034	3.196	0.843	1.856
Case 4	7.920	0.517	1.790	0.843	1.856
Case 5	2.640	0.517	2.495	0.843	1.856
Case 6	5.280	0.259	1.807	0.843	1.856
Case 7	7.920	0.259	1.254	0.843	1.856
Case 8	2.640	0.259	3.335	0.843	1.856
Case 9	5.280	0.517	0.436	0.843	1.856

SET_10	Shape	Scale	Data	
Case 1	5.171	0.511	x1	0.34
Case 2	7.101	0.503	x2	0.55
Case 3	2.616	0.694	x3	0.36
Case 4	7.038	0.483		
Case 5	2.818	0.477		
Case 6	4.193	0.373		
Case 7	5.108	0.393		
Case 8	2.544	0.326		
Case 9	5.192	0.474		
MLM	4.682	0.458		
Non-inform.	3.610	0.436		

Raw results for Table 38 calculated above:

Table 50: Set (1) calculation results when sample size =10

Set 1	Shape	Scale	Bay (normal prior) Dist. C	MLM Dist. C	Bay (non-informative) Dist. C
Case 1	5.280	1.034	0.555	1.859	1.354
Case 2	7.920	1.034	2.378	1.859	1.354
Case 3	2.640	1.034	2.028	1.859	1.354
Case 4	7.920	0.517	2.321	1.859	1.354
Case 5	2.640	0.517	2.024	1.859	1.354
Case 6	5.280	0.259	0.653	1.859	1.354
Case 7	7.920	0.259	1.326	1.859	1.354
Case 8	2.640	0.259	2.628	1.859	1.354
Case 9	5.280	0.517	0.541	1.859	1.354

Set 1	Shape	Scale	Data	
Case1	5.835	0.515	x1	0.558
Case2	7.658	0.519	x2	0.380
Case3	3.253	0.525	x3	0.449
Case4	7.601	0.513	x4	0.397
Case5	3.266	0.496	x5	0.519
Case6	5.089	0.455	x6	0.534
Case7	6.535	0.474	x7	0.586
Case8	2.908	0.404	x8	0.563
Case9	5.810	0.506	x9	0.367
MLM	7.138	0.511	x10	0.424
Non-inform.	6.631	0.508		

Table 51: Set (2 calculation results when sample size =10

Set 2	Shape	Scale	Bay (normal prior) Dist. C	MLM Dist. C	Bay (non-informative) Dist. C
Case 1	5.280	1.034	0.354	1.112	0.612
Case 2	7.920	1.034	2.054	1.112	0.612
Case 3	2.640	1.034	2.092	1.112	0.612
Case 4	7.920	0.517	2.000	1.112	0.612
Case 5	2.640	0.517	2.090	1.112	0.612
Case 6	5.280	0.259	0.807	1.112	0.612
Case 7	7.920	0.259	0.955	1.112	0.612
Case 8	2.640	0.259	2.718	1.112	0.612
Case 9	5.280	0.517	0.344	1.112	0.612

Set 2	Shape	Scale	Data	
Case1	5.634	0.517	x1	0.347
Case2	7.334	0.520	x2	0.536
Case3	3.190	0.526	x3	0.526
Case4	7.280	0.514	x4	0.579
Case5	3.201	0.496	x5	0.366
Case6	4.818	0.451	x6	0.509
Case7	6.113	0.470	x7	0.568
Case8	2.825	0.400	x8	0.444
Case9	5.609	0.507	x9	0.543
MLM	6.390	0.510	x10	0.298
Non-inform.	5.882	0.506		

Table 52: Set (3 calculation results when sample size =10

Set 3	Shape	Scale	Bay (normal prior) Dist. C	MLM Dist. C	Bay (non-informative) Dist. C
Case 1	5.280	1.034	0.754	3.021	2.459
Case 2	7.920	1.034	2.835	3.021	2.459
Case 3	2.640	1.034	1.996	3.021	2.459
Case 4	7.920	0.517	2.777	3.021	2.459
Case 5	2.640	0.517	1.967	3.021	2.459
Case 6	5.280	0.259	0.488	3.021	2.459
Case 7	7.920	0.259	1.755	3.021	2.459
Case 8	2.640	0.259	2.580	3.021	2.459
Case 9	5.280	0.517	0.754	3.021	2.459

Set 3	Shape	Scale	Data	
Case1	6.034	0.520	x1	0.464
Case2	8.110	0.533	x2	0.467
Case3	3.300	0.542	x3	0.410
Case4	8.055	0.527	x4	0.600
Case5	3.314	0.510	x5	0.567
Case6	5.302	0.468	x6	0.573
Case7	7.014	0.490	x7	0.559
Case8	2.919	0.413	x8	0.402
Case9	6.034	0.520	x9	0.439
MLM	8.299	0.528	x10	0.499
Non-inform.	7.737	0.525		

Table 53: Set (4) calculation results when sample size =10

Set 4	Shape	Scale	Bay (normal prior) Dist. C	MLM Dist. C	Bay (non-informative) Dist. C
Case 1	5.280	1.034	0.686	0.556	0.688
Case 2	7.920	1.034	1.392	0.556	0.688
Case 3	2.640	1.034	2.259	0.556	0.688
Case 4	7.920	0.517	1.189	0.556	0.688
Case 5	2.640	0.517	2.160	0.556	0.688
Case 6	5.280	0.259	1.582	0.556	0.688
Case 7	7.920	0.259	1.220	0.556	0.688
Case 8	2.640	0.259	2.914	0.556	0.688
Case 9	5.280	0.517	0.497	0.556	0.688

Set 4	Shape	Scale	Data	
Case1	5.272	0.586	x1	0.410
Case2	6.457	0.591	x2	0.700
Case3	3.140	0.590	x3	0.612
Case4	6.309	0.577	x4	0.509
Case5	3.136	0.543	x5	0.601
Case6	3.781	0.466	x6	0.683
Case7	4.126	0.477	x7	0.439
Case8	2.545	0.416	x8	0.511
Case9	5.193	0.566	x9	0.444
MLM	5.140	0.571	x10	0.332
Non-inform.	4.787	0.565		

Table 54: Set (5) calculation results when sample size =10

Set 5	Shape	Scale	Bay (normal prior) Dist. C	MLM Dist. C	Bay (non-informative) Dist. C
Case 1	5.280	1.034	0.406	0.991	1.301
Case 2	7.920	1.034	0.510	0.991	1.301
Case 3	2.640	1.034	2.240	0.991	1.301
Case 4	7.920	0.517	0.469	0.991	1.301
Case 5	2.640	0.517	2.267	0.991	1.301
Case 6	5.280	0.259	1.544	0.991	1.301
Case 7	7.920	0.259	1.169	0.991	1.301
Case 8	2.640	0.259	2.895	0.991	1.301
Case 9	5.280	0.517	0.497	0.991	1.301

Set 5	Shape	Scale	Data	
Case1	4.910	0.500	x1	0.341
Case2	5.774	0.505	x2	0.389
Case3	3.044	0.503	x3	0.493
Case4	5.696	0.495	x4	0.471
Case5	3.050	0.476	x5	0.446
Case6	4.055	0.423	x6	0.197
Case7	4.473	0.432	x7	0.602
Case8	2.711	0.384	x8	0.377
Case9	4.870	0.489	x9	0.613
MLM	4.356	0.481	x10	0.449
Non-inform.	4.049	0.475		

Table 55: Set (6) calculation results when sample size =10

Set 6	Shape	Scale	Bay (normal prior) Dist. C	MLM Dist. C	Bay (non-informative) Dist. C
Case 1	5.280	1.034	0.720	1.292	1.537
Case 2	7.920	1.034	0.333	1.292	1.537
Case 3	2.640	1.034	2.265	1.292	1.537
Case 4	7.920	0.517	0.255	1.292	1.537
Case 5	2.640	0.517	2.259	1.292	1.537
Case 6	5.280	0.259	1.963	1.292	1.537
Case 7	7.920	0.259	1.850	1.292	1.537
Case 8	2.640	0.259	2.960	1.292	1.537
Case 9	5.280	0.517	0.720	1.292	1.537

Set 6	Shape	Scale	Data	
Case1	4.565	0.525	x1	0.334
Case2	5.216	0.550	x2	0.289
Case3	3.029	0.542	x3	0.494
Case4	5.079	0.533	x4	0.746
Case5	3.024	0.505	x5	0.462
Case6	3.513	0.432	x6	0.534
Case7	3.621	0.435	x7	0.514
Case8	2.581	0.395	x8	0.376
Case9	4.565	0.525	x9	0.532
MLM	3.988	0.517	x10	0.418
Non-inform.	3.745	0.510		

Table 56: Set (7) calculation results when sample size =10

Set 7	Shape	Scale	Bay (normal prior) Dist. C	MLM Dist. C	Bay (non-informative) Dist. C
Case 1	5.280	1.034	0.740	2.845	2.275
Case 2	7.920	1.034	2.767	2.845	2.275
Case 3	2.640	1.034	2.015	2.845	2.275
Case 4	7.920	0.517	2.712	2.845	2.275
Case 5	2.640	0.517	1.986	2.845	2.275
Case 6	5.280	0.259	0.494	2.845	2.275
Case 7	7.920	0.259	1.680	2.845	2.275
Case 8	2.640	0.259	2.608	2.845	2.275
Case 9	5.280	0.517	0.706	2.845	2.275

Set 7	Shape	Scale	Data	
Case1	6.007281123	0.530419226	x1	0.606
Case2	8.043	0.533	x2	0.456
Case3	3.281	0.543	x3	0.560
Case4	7.990	0.527	x4	0.564
Case5	3.295	0.511	x5	0.513
Case6	5.234	0.468	x6	0.495
Case7	6.937	0.489	x7	0.412
Case8	2.892	0.412	x8	0.554
Case9	5.985	0.520	x9	0.465
MLM	8.123	0.528	x10	0.345
Non-inform.	7.554	0.525		

Table 57: Set (8) calculation results when sample size =10

Set 8	Shape	Scale	Bay (normal prior) Dist. C	MLM Dist. C	Bay (non-informative) Dist. C
Case 1	5.280	1.034	0.920	1.750	2.025
Case 2	7.920	1.034	0.414	1.750	2.025
Case 3	2.640	1.034	2.399	1.750	2.025
Case 4	7.920	0.517	0.418	1.750	2.025
Case 5	2.640	0.517	2.389	1.750	2.025
Case 6	5.280	0.259	2.322	1.750	2.025
Case 7	7.920	0.259	2.323	1.750	2.025
Case 8	2.640	0.259	3.140	1.750	2.025
Case 9	5.280	0.517	0.920	1.750	2.025

Set 8	Shape	Scale	Data	
Case1	4.363	0.524	x1	0.182
Case2	5.005	0.548	x2	0.574
Case3	2.899	0.546	x3	0.681
Case4	4.885	0.531	x4	0.289
Case5	2.894	0.506	x5	0.384
Case6	3.167	0.421	x6	0.595
Case7	3.166	0.421	x7	0.618
Case8	2.416	0.388	x8	0.496
Case9	4.363	0.524	x9	0.402
MLM	3.531	0.513	x10	0.385
Non-inform.	3.260	0.504		

Table 58: Set (9) calculation results when sample size =10

Set 9	Shape	Scale	Bay (normal prior) Dist. C	MLM Dist. C	Bay (non-informative) Dist. C
Case 1	5.280	1.034	0.486	1.114	1.394
Case 2	7.920	1.034	0.265	1.114	1.394
Case 3	2.640	1.034	2.235	1.114	1.394
Case 4	7.920	0.517	0.135	1.114	1.394
Case 5	2.640	0.517	2.251	1.114	1.394
Case 6	5.280	0.259	1.745	1.114	1.394
Case 7	7.920	0.259	1.512	1.114	1.394
Case 8	2.640	0.259	2.915	1.114	1.394
Case 9	5.280	0.517	0.554	1.114	1.394

Set 9	Shape	Scale	Data	
Case1	4.797	0.522	x1	0.394
Case2	5.524	0.527	x2	0.521
Case3	3.045	0.521	x3	0.283
Case4	5.413	0.515	x4	0.681
Case5	3.046	0.490	x5	0.573
Case6	3.780	0.428	x6	0.548
Case7	4.013	0.435	x7	0.382
Case8	2.658	0.390	x8	0.357
Case9	4.735	0.507	x9	0.358
MLM	4.181	0.499	x10	0.439
Non-inform.	3.908	0.492		

Table 59: Set (10) calculation results when sample size =10

Set 10	Shape	Scale	Bay (normal prior) Dist. C	MLM Dist. C	Bay (non-informative) Dist. C
Case 1	5.280	1.034	1.149	5.662	5.060
Case 2	7.920	1.034	3.630	5.662	5.060
Case 3	2.640	1.034	1.921	5.662	5.060
Case 4	7.920	0.517	3.596	5.662	5.060
Case 5	2.640	0.517	1.896	5.662	5.060
Case 6	5.280	0.259	0.770	5.662	5.060
Case 7	7.920	0.259	2.899	5.662	5.060
Case 8	2.640	0.259	2.470	5.662	5.060
Case 9	5.280	0.517	1.143	5.662	5.060

Set 10	Shape	Scale	Data	
Case1	6.429	0.518	x1	0.502
Case2	8.910	0.520	x2	0.480
Case3	3.367	0.535	x3	0.540
Case4	8.876	0.516	x4	0.467
Case5	3.387	0.506	x5	0.433
Case6	5.879	0.469	x6	0.595
Case7	8.165	0.489	x7	0.513
Case8	3.033	0.415	x8	0.448
Case9	6.421	0.511	x9	0.518
MLM	10.942	0.520	x10	0.493
Non-inform.	10.340	0.518		

9 Conclusions

Firstly, specimen suitable for micro testing has been designed and an experimental procedure for pure bending and combined loading have been proposed. Pure bending and combined loading tests have been performed. A separate fracture criterion for each form of geometry and loading has been proposed. Besides, fracture criterion for combined loading can be used for pure torsion loading based on load factor analysis. Finally, a general safety design procedure has been proposed.

10 Future plans

In the near future, there is a need to correlate the fracture strength of the specimens with the etching parameters. Statistical procedures will be employed and as such, large number of samples has to be tested. Hence, there is a need to standardize experiments to save computational time. Moreover, from an industrial point of view, there will probably be demand for real-time reliability tests, which will hasten the product developmental process. Characterization of surface roughness will probably require image process techniques and surface roughness variation within the same piece of wafer and hence strength variation within the same piece of wafer will be investigated.

11 References

- (1) N. Asada, H. Matsuki, K. Minami, M. Esashi, "Silicon Micromachined Two-Dimensional Galvano optical Scanner", IEEE Transactions on Magnetics, Vol.30, No. 6, Nov. 1994
- (2) Tsuchiya T, Tabato O, Sakata J and Taga Y, "Specimen size effect on tensile strength of surface-micromachined polycrystalline silicon thin films", J. Microelectromech. System, 1998, 106-113
- (3) Sato K, Shikida M, Yoshioka T, Ando T and Kawabata T, " Micro tensile test of silicon film having different crystallographic orientations", Solid-state sensors and actuators, 1996, 595-598
- (4) Taechung Yi, Chang-Jin Kim, "Measurement of mechanical properties for MEMS materials", Meas. Sci. Technol., 10 (1999) 706-716
- (5) P.D. Warren, "Fracture of brittle materials: effects of test method and threshold stress on the Weibull modulus", Journal of the European Ceramic Society, 21,2001,335-342
- (6) Chunsheng Lu, Robert Danzer, and Franz Dieter Fischer, "Fracture statistics of brittle materials: Weibull or normal distribution", Physical review E, vol. 65, 067102
- (7) Horst Fischer, Walter Rentzsch, Rudolf Marx, "A modified size effect model for brittle nonmetallic materials", engineering fracture mechanics, 69, 2002, 781-791
- (8) S.L. Fok, B.C. Mitchell, J. Smart. B.J. Marsden, "A numerical study on the application of the Weibull theory to brittle materials", engineering fracture mechanics, 68, 2001, 1171-1179
- (9) H. Peterlik, D. Loidl, "Bimodal strength distributions and flaw populations of ceramics and fibers", engineering fracture mechanics, 68, 2001, 253-261
- (10) P. Zinck, J.F. Gerard, H.D. Wagner, " On the significance and description of the size effect in multimodal fracture behavior; experimental assessment on E-glass fibers", engineering fracture mechanics, 69,2002,1049-1055
- (11) C.P. Chen, T.H. Chang, "Fracture mechanics evaluation of optical fibers", material chemistry and physics, 77, 2002, 110-116
- (12) Dongchu Sun, "A note on noninformative priors for Weibull distributions", journal of statistical planning and inference, 61, 1997, 319-338
- (13) Takahiro Namazu, Yoshitada Isono, Takeshi Tanaka, "Evaluation of size effect on mechanical properties of single crystal silicon by nanoscale bending test using AFM", Journal of MEMS, 9, Dec 2000, 4
- (14) J.N. Ding, Y.G. Meng, S.Z. Wen, "Specimen size effect on mechanical properties of polysilicon microcantilever beams measured by deflection using a nanoindenter", materials science and engineering, 83, 2001, 42-47
- (15) William N. Sharpe, " Effect of specimen size on young's modulus and fracture strength of polysilicon", Journal of MEMS, 10, Sept 2001, 3
- (16) C. J. Wilson, A. ormeggi, and M. Narbutovskih, " Fracture testing of silicon microcantilever beams", Journal of Applied Physics, vol. 79, no. 5

- (17) S.C. Bromley, L.L. Howell, B.D. Jenson, " Determination of maximum allowable strain for polysilicon micro-devices", engineering failure analysis, 6, 1999, 27-41
- (18) Xiaodong Li, Bharat Bhushan, " Fatigue studies of nanoscale structures for MEMS/NEMS applications using nanoindentation techniques", surface and coatings tech., 2002
- (19) Sriram Sundararajan, Bharat Bhushan, " Development of AFM-based techniques to measure mechanical properties of nanoscale structures", sensors and actuators, A 3526, 2002, 1-14
- (20) Yoshitada Isono, " Mechanical characterization of sub-micrometer thick DLC films by AFM tensile testing for surface modification in MEMS"
- (21) Yoshitada Isono, " Pastic deformation of nanometric single crystal silicon wire in AFM bending test at intermediate temperatures"
- (22) Hiroshi Miyajima, " A study on nonlinear torsional characteristics of polyimide hinges", solid-state sensors and actuators,
- (23) G. Schiltges, J. Dual, " Failure behavior of microstructures under torsional loads", Institute of Mechanics
- (24) M.A. Haque and M. T. A. Saif, " Microscale materials testing using MEMS actuators", Journal of MEMS, vol. 10, no. 1
- (25) Jan Vedde, Peter Gravesen, " The fracture strength of nitrogen doped silicon wafers", material science and engineering, B36, 1996, 246-250

12 General readings

- (1) Gere & Timoshenko, "Mechanics of Materials", 4th edition. Chapter 2: Stress concentration, page135
- (2) Roark & Young, "Formulas for stress and strain", 6th edition, Table 20, case 4, page348
- (3) Derek Hull, "Fractography (observing, measuring and interpreting fracture surface topography)", Cambridge University Press
- (4) T.L Anderson, "Fracture Mechanics (fundamentals and applications)", 2nd edition
- (5) Norman E. Dowling, " Mechanical Behavior Of Materials (engineering methods for deformation, fracture, and fatigue)", Prentice-Hall International Editions
- (6) Murray R. Spiegel, "Schaum's outline series: Theory and problems of Statistics", 2nd edition
- (7) James R. Evans and David L. Olson, "Introduction To Simulation And Risk Analysis", 2nd edition
- (8) John H. Mathews and Kurtis D. Fink, "Numerical Methods Using Matlab", 3rd edition
- (9) Samuel Kotz and Saralees Nadarajah, " Extreme Value Distribution: theory and applications", Imperial College Press
- (10)M. Elwenspoek and H. Jansen, "Silicon Micromachining", Cambridge University press
- (11)Sergey Edward Lyshevski, "MEMS and NEMS: Systems, devices and structures", CRC press
- (12)J.F. NYE, " Physical Properties of Crystals", Oxford science publications
- (13)Shafique M.A. Khan, Marwan K. Khraisheh, "Analysis of mixed mode crack initiation angles under various loading conditions", engineering fracture mechanics, 67, 2000, 397-419
- (14)Christopher L. Muhlstein, Stuart B. Brown, Robert O. Ritchie, "High-cycle Fatigue of single-crystal silicon thin films", Journal of MEMS, 10, Dec 2001,4
- (15)S.M. Spearing, "Material issues in MEMS", Acta materialia, 48, 2000, 179-196
- (16)Richard W. Hertzberg, "Deformation and fracture mechanics of engineering materials", 3rd editon

13 Acknowledgement

I would like to express my heartfelt thanks to all the people around me who have helped me make this research enjoyable and meaningful.

以上

1~184 ページ 完
修士論文

平成 16 年 2 月 13 日 提出

26199 チャン ウエー ピン